I. PREPROCESSING FOR TOWED STREAMER, OCEAN BOTTOM AND ONSHORE ACQUISITION, FOR HORIZONTAL OR NON-HORIZONTAL ACQUISITION SURFACE: IMPLICATIONS FOR MULTIPLE REMOVAL, STRUCTURAL DETERMINATION AND AMPLITUDE ANALYSIS; II. INVERSE SCATTERING SERIES INTERNAL MULTIPLE ATTENUATION IN AN ABSORPTIVE DISPERSIVE EARTH, WITHOUT KNOWING, NEEDING OR ESTIMATING ELASTIC OR ANELASTIC SUBSURFACE PROPERTIES

A Dissertation Presented to

the Faculty of the Department of Physics

University of Houston

In Partial Fulfillment

of the Requirements for the Degree

Doctor of Philosophy

By

Jing Wu

August 2017

I. PREPROCESSING FOR TOWED STREAMER, OCEAN BOTTOM AND ONSHORE ACQUISITION, FOR HORIZONTAL OR NON-HORIZONTAL ACQUISITION SURFACE: IMPLICATIONS FOR MULTIPLE REMOVAL, STRUCTURAL DETERMINATION AND AMPLITUDE ANALYSIS; II. INVERSE SCATTERING SERIES INTERNAL MULTIPLE ATTENUATION IN AN ABSORPTIVE DISPERSIVE EARTH, WITHOUT KNOWING, NEEDING OR ESTIMATING ELASTIC OR ANELASTIC SUBSURFACE PROPERTIES

Jing Wu

APPROVED:

Dr. Arthur B. Weglein, Chairman

Dr. Lowell T. Wood

Dr. Donna W. Stokes

Dr. Clement Kostov

Dean, College of Natural Sciences and Mathematics

ACKNOWLEDGMENTS

This dissertation is finished with the help from many colleagues and mentors.

First and foremost, my deepest gratitude is to my advisor, Professor Arthur B. Weglein, for his continued guidance support and encouragement during my study at University of Houston. I benefit from his innovative thinking, profound knowledge and am inspired by his enthusiasm to the research and work. I would always appreciate Professor Weglein for his extremely valuable instruction and his support. I would also like to thank Dr. Wood, Dr. Bassler, Dr. Lee, Dr. Stokes and Dr. Kostov for serving as my dissertation committee members.

I am greatly indebted to Clement Kostov for providing me with two incredibly rewarding internship opportunities at Schlumberger. I appreciate the tremendous effort and excellent mentoring from Clement and the talented people in his professional team: James Wu, Bill Dragoset, Fred Melo, Debra Dishberger, Jae Young Park, Clement Zhang, Glenn Miers, Ahmed Ali, Scott Slaton, and Vasudha Govindan.

I would like to express my gratitude to all the sponsors for their support to our M-OSRP group. I would like to extend thanks to the colleagues formerly or currently in this great team: Fang Liu, Jingfeng Zhang, James Mayhan, Hong Liang, Chao Ma, Jinlong Yang, Qiang Fu, Xinglu Lin, Yanglei Zou, Yuchang Shen, Zhen Zhang, Lin Tang and Nour Alzamil, for their worthwhile discussions, suggestions and feedbacks on my research. I would like to thank Jennifer Chin-Davis, Naomi Haynes, and Jackqueline Owens for their administrative help and support. Yuting Duan is thanked for her longterm friendship and huge encouragement.

Finally, I would like to express my greatest gratitude to my parents and my brother, for their constant support, encouragement and concern.

I. PREPROCESSING FOR TOWED STREAMER, OCEAN BOTTOM AND ONSHORE ACQUISITION, FOR HORIZONTAL OR NON-HORIZONTAL ACQUISITION SURFACE: IMPLICATIONS FOR MULTIPLE REMOVAL, STRUCTURAL DETERMINATION AND AMPLITUDE ANALYSIS; II. INVERSE SCATTERING SERIES INTERNAL MULTIPLE ATTENUATION IN AN ABSORPTIVE DISPERSIVE EARTH, WITHOUT KNOWING, NEEDING OR ESTIMATING ELASTIC OR ANELASTIC SUBSURFACE PROPERTIES

An Abstract of a Dissertation

Presented to

the Faculty of the Department of Physics

University of Houston

In Partial Fulfillment

of the Requirements for the Degree

Doctor of Philosophy

By

Jing Wu

August 2017

ABSTRACT

The first part of this dissertation advances Green's theorem wave separation methods for separating the reference wave and reflection data and for deghosting. There are several contributions within this first topic area. Firstly, note that a depth-variable acquisition surface can frequently occur either with a feathered cable in water or with a complicated topography in onshore or ocean bottom acquisition. Under these circumstances, directly applying Green's theorem deghosting method cannot deghost the recorded data on the acquisition surface. This dissertation proposes a new approach which is able to effectively solve this problem. Secondly, Green's theorem wave separation is a mature application in marine towed streamer acquisition. This dissertation extends the deghosting method to ocean bottom data. Thirdly, the current filtering methods for onshore ground roll removal may often damage reflection data; this dissertation develops Green's theorem wave separation algorithm which can satisfactorily address this issue. In a further step, this dissertation proposes a simplified algorithm to achieve onshore wave separation with a reduced data requirement. These solutions can enhance the capability of Green's theorem wave separation method and provide an adequate satisfaction of prerequisites for the subsequent multiple removal, structural determination, and amplitude analysis.

The second part of this dissertation investigates the performance of the inverse scattering series internal multiple attenuation method for an anelastic medium with absorption and dispersion. Both analytical and numerical tests demonstrate the attenuation method retains its effectiveness to predict the internal multiple with the right time and approximate am-

plitude, and without requiring any elastic or anelastic property. For an anelastic medium, the approximate amplitude predicted by the inverse scattering internal multiple attenuation algorithm is further from the exact amplitude than in the corresponding acoustic/elastic circumstance. When the anelastic property can be provided or estimated, a new algorithm is developed to improve the predicted amplitude.

CONTENTS

LIST OF FIGURES

LIST OF TABLES

1. INTRODUCTION

1.1 General background of seismic exploration

The objective of seismic exploration is to discover new oil and gas resources and to enable a better understanding and characterization of reservoirs under production. For exploration seismology, a man-made source[1] generates waves propagating in the subsurface. When the wave reaches a reflector where rock properties change, it is reflected upward towards the surface and then recorded by receivers[2]. Figure 1.1 illustrates three types of seismic acquisition: marine towed streamers, ocean bottom sensors, and land surface receivers. The seismic data recorded by the receiver are processed to locate subsurface interfaces (called migration/imaging) and delineate the specific earth mechanical property changes across those interfaces (called inversion). The images and material properties are important for structural geology interpretation and reservoir characterization.

The recorded data consist of different types of waves based on their experience in the subsurface, as listed below. (Figure 1.2 depicts marine seismic waves. Land data contain similar types of waves except land data include surface wave, which will be described below.)

- **Reference wave.** Both the Green's theorem method and inverse scattering series (ISS) method (which will be studied in this dissertation) start from perturbation

[1] A land survey uses shallow borehole explosives such as dynamite, or vibratory mechanisms mounted on a truck; a marine survey uses air guns to fire air bubbles into the water (`http://editors.eol.org/eoearth/wiki/Seismic_exploration`).

[2] Receiver can be a hydrophone that measures pressure changes of the wave traveling in water, or a geophone that measures displacement/velocity of the wave traveling in water or earth.

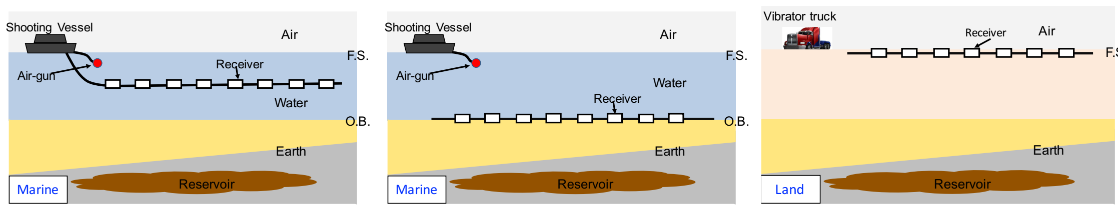

(a) (b) (c)

Fig. 1.1: Diagrams of three types of seismic acquisition; (a) marine towed streamer; (b) ocean bottom sensors; (c) onshore surface receivers. F.S. is free surface; O.B. is ocean bottom.

theory. Perturbation theory separates the actual medium into a reference medium plus a perturbation. The choice of a reference medium depends on the specific seismic objective and application. The waves that propagate in the reference medium are called reference waves. The waves that travel in the actual medium are called total waves. The difference between the total and reference waves is defined as the scattered wave (or reflection data).

For marine acquisition, if the reference medium is chosen to be a half-space of air over a half-space of water, the reference wave contains a direct wave[3] and wave that first travels up to the free surface[4] and then to the receiver. The reference wave does not experience the earth; hence, it does not carry any earth information.

For land acquisition, if the reference medium is chosen to be a homogeneous air half-space over a homogeneous earth half-space, the major portion of the reference wave is the Rayleigh wave (also called ground roll). Ground roll travels along the earth's surface and causes the particles near earth's surface to move retrogradely, as shown in Figure 1.3.

- **Ghost.** A ghost begins its propagation history by traveling up from the source to the free surface (called **source ghost**) or ending its history by traveling down from the free surface to the receiver (called **receiver ghost**) or both (called **source-receiver**

[3] Direct wave travels straightly from source to a receiver.
[4] Free surface refers to air/water boundary in marine or air/earth boundary onshore.

ghost).

The remaining waves that begin their history going downward from the source and end their history going upward at the receiver are divided into primary and multiple:

- **Primary.** A primary has only one upward reflection in its entire propagation history.

- **Multiple.** A multiple experiences more than one upward reflection in its history. Depending on the location of downward reflection between two consecutive upward refections, multiple is further classified as free-surface multiple and internal multiple. Multiples that have at least one downward reflection at the free surface are called free-surface multiples, whereas multiples that have all of their downward reflections below the free surface are called internal multiples. The order of a free-surface multiple is determined by the total number of downward reflections at the free surface. The order of an internal multiple is defined by the total number of the downward reflections that it has experienced from any subsurface reflectors (Weglein et al., 1997).

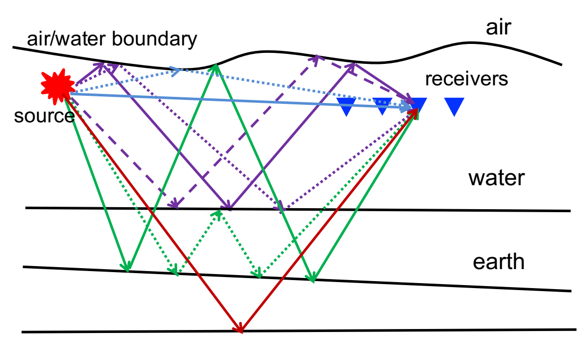

Fig. 1.2: Marine seismic waves: 1, reference wave (blue solid line and blue dotted line); 2, source ghost (purple dotted line); 3, receiver ghost (purple dashed line); 4, source-receiver ghost (purple solid line); 5, free-surface multiple (green solid line); 6, internal multiple (green dotted line); and 7, primary (red solid line).

Although different types of seismic waves are recorded, the methods for extracting subsurface information from seismic data typically assume that the data consist exclusively of primaries (Weglein et al., 2003). There are two reasons for a primary-only assumption.

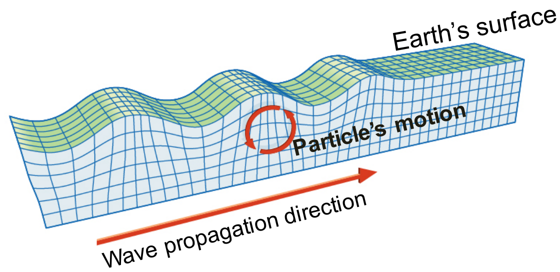

Fig. 1.3: A diagram of Rayleigh wave. (`https://www.britannica.com/science/seismograph`)

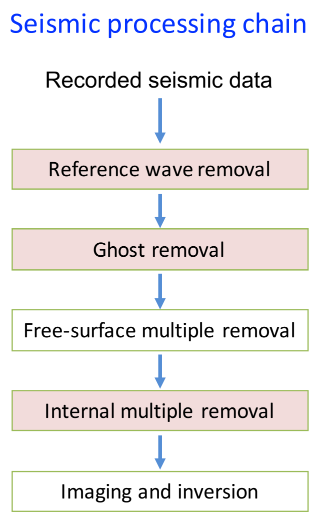

Fig. 1.4: Seismic processing chain. This dissertation contributes to the three highlighted steps.

First, this assumption can simplify the processing of seismic data for migration and inversion. Second, a smooth and continuous velocity model is generally assumed in practice for different imaging methods (e.g., Claerbout (1971); Whitmore (1983); McMechan (1983); Baysal et al. (1983); Weglein et al. (2011a,b); Liu and Weglein (2014)). When a smooth and continuous velocity model is used, only primaries are required to locate reflectors, whereas other waves, such as multiples, will result in false images of reflectors (Weglein, 2016). Therefore, a key goal of seismic processing is to take the recorded seismic data, remove the reference waves, the ghosts and the multiples, and end up with primaries without distorting the primaries. Figure 1.4 illustrates a typical seismic processing chain that this dissertation follows in order to remove different types of waves and get primaries for migration and inversion. The first two steps are considered as the preprocessing. As a linked chain of steps, the effectiveness of any given step not only depends upon how well its own assumptions are satisfied but also how well the preceding tasks in the chain have been achieved.

This dissertation focuses on three specific steps (highlighted with the pink box in Figure 1.4):

1. Reference wave identification and removal;
2. Ghost removal / deghosting;
3. Internal multiple removal.

1.2 Challenge and advance for removing the reference wave and ghosts

As the first two steps of the seismic processing chain (Figure 1.4), the quality of reference wave removal and ghost removal has a direct impact on all the subsequent steps: multiple removal, migration, and inversion.

This section describes (1) the challenge of each step, (2) the capability and open issues of the Green's theorem preprocessing methods and (3) contributions made to improve the Green's theorem methods in this dissertation.

Challenge of the reference wave removal

Reference wave removal could be a difficult task for both offshore and onshore processing. First, in marine experiment, especially for shallow water exploration, the high-energy reference wave (the direct arrival and its ghost) can seriously interfere with and mask the reflection data that are from the water bottom. A filtering method (e.g., singular value decomposition) may not fully remove the reference wave, and the residual artifact can still affect the imaging of the shallowest part of the water column (Piété et al., 2013). Second, in onshore experiment, the reference wave contains strong surface waves. On one hand, the removal of the ground roll without damaging the reflection data is a high priority and an outstanding challenge for onshore processing. The coherency of ground roll makes it non-trivial to be removed (Socco et al., 2010). On the other hand, ground roll can be useful for near surface inversion (Nolet and Panza, 1976; McMechan and Yedlin, 1981). Various filtering methods have been developed to separate ground roll from reflection data (Yilmaz, 2001). However, those methods may damage reflection data (ground roll is also harmed).

Challenge of deghosting

Deghosting has attracted a great deal of industry attention especially because of the increasing interest in marine broadband[5] seismic technology (Amundsen et al., 2013b; Amundsen and Zhou, 2013). The destructive interference between primaries and ghosts can lead to notches[6] that can negatively affect the spectral bandwidth of recorded data and therefore compromise the interpretability of data (van Borselen et al., 2013). Additionally, the low-frequency information of seismic data can be significant in seismic imaging and inversion and can be damaged by ghost notches (Farouki et al., 2010; Wang and Peng, 2012). A major issue of many current deghosting methods (e.g., the industry widely used $P - V_z$ method in industry) is that they are derived with an assumption of a horizontal acquisition surface (Amundsen, 1993; Amundsen et al., 2013a; Osen et al., 1999), which often violates the reality. The shape of a marine towed streamer (Figure 1.1) can be depth variant due to feathering; onshore and ocean bottom acquisition can be deployed along an undulating surface (air/earth boundary or water/earth boundary). Under those circumstances, applying the $P - V_z$ method is inappropriate in principle and can cause severe consequences to subsequent multiple removal and imaging (Shen and Weglein, 2017; Zhang and Weglein, 2017). (Note: the variable topography could be shifted to a horizontal surface before applying the $P - V_z$ method. That correction is often done with traditional static correction (Yilmaz, 2001). The difference between static correction and Green's theorem wave prediction (which

[5] Broadband refers to a wider band of frequencies being recorded than in conventional seismic exploration.
[6] Ghost notch refers to the frequency where the spectrum destructive interference occurs.

is wave theoretical (Weglein et al., 2011a) and more accurate) is shown in Appendix A.)

The capability of Green's theorem wave separation method

Originating from wave theory, Green's theorem can satisfactorily achieve two objectives: (1) the separation of reference wave and reflection data without damaging the reference wave and the reflection data (Weglein and Secrest, 1990; Keho et al., 1990) and (2) deghosting the reflection data without damaging the primaries and multiples (Weglein et al., 2002; Zhang, 2007; Mayhan et al., 2011; Mayhan and Weglein, 2013). This method can automatically accommodate a non-horizontal measurement surface. It supersedes the $P - V_z$ method. In addition, Green's theorem deghosting is performed without any prior information about (1) the source wavelet, (2) the shape of and the reflection at the sea surface and (3), the earth property below the measurement surface.

The open issue of Green's theorem wave separation method and the advances made in this dissertation

Green's theorem has shown its distinct advantages; however, it requires a further development and advancement for more ambitious offshore and onshore application. In summary, in order to address the aforementioned challenges that neither the traditional methods (e.g., the filtering methods and the $P - V_z$ method) nor the current available Green's theorem method can fully solve, this dissertation advances the Green's theorem method from three aspects.

1) Deghosting the recorded data on a depth-variable acquisition surface

Although Green's theorem deghosting method (expressed in the space-frequency domain) can accommodate a non-horizontal measurement surface, it can only output the deghosted result at a surface above the acquisition surface. In addition, for onshore or ocean bottom acquisition, deghosting right on the measurement surface is necessary. If the measurement surface is horizontal, the algorithm can be expressed in the wavenumber-frequency domain (equivalent to $P - V_z$ method), and the recorded data can be deghosted on the measurement surface. However, that procedure is not available with non-horizontal measurement surface. **Chapter 2** proposes a new two-step strategy (Wu and Weglein, 2017) by combining Green's theorem deghosting and Green's theorem one-way wave prediction (Weglein et al., 2011a,b). It can achieve deghosting on the measurement surface without assuming the measurement surface to be horizontal. Onshore and ocean bottom acquisition with complicated topography can also benefit from this new approach and method.

2) Deghosting ocean bottom data

The application of Green's theorem methods is mature for marine towed streamer data today. A natural extension is to develop more sophisticated algorithms for deghosting the ocean bottom data. Typically, the pressure data are acquired slightly above the ocean bottom in water, while the multicomponent displacement is measured slightly below the ocean bottom in the solid earth. The current algorithm (Zhang, 2007) is applicable to deghost the pressure data. But in order to deghost the displacement data, an elastic reference medium should be chosen and an elastic version of Green's theorem wave separation algorithm is required. Pao and Varatharajulu (1976) and Weglein and Secrest (1990) put forward the original theory for the separation of data with an elastic reference medium. **Chapter 3** utilizes and develops that theory to deghost the ocean bottom displacement data without assuming a horizontal ocean bottom (Wu and Weglein, 2016b).

3) Removing ground roll and ghosts onshore

Another extension of Green's theorem wave separation is for onshore application. **Chapter 4** derives the algorithm for data in the PS space[7] (Wu and Weglein, 2014, 2015b) to separate the reference wave (including ground roll) and reflection data and then to deghost the reflection data. **Chapter 5** develops the algorithm for data in the displacement space

[7] The acquired data are in form of displacements, which can be decomposed into P (longitudinal) and S (transverse) components (Weglein and Stolt, 1995; Zhang, 2006)

(Wu and Weglein, 2015a). A significant advantage of the Green's theorem method over the current linear filtering methods is that it can directly predict either the reference wave (including ground roll) or the reflection data, and without damaging the reference wave and reflection data. However, the complete algorithms (in Chapter 4 and 5) require both the multicomponent data and their spatial derivatives. For example, to carry out the wave separation algorithm for data in the displacement space, both the multicomponent displacement and the traction are needed. The requirement of multicomponent displacement can at times be recorded with the current acquisition, whereas traction can not. **Chapter 6** proposes a simplified algorithm (Wu and Weglein, 2016a) that can achieve the wave separation with a reduced data requirement: the requirement of traction is replaced by a simple source wavelet. Another issue to be further investigated in future is how to remove ground roll with near surface lateral variance without knowing near surface property. An initial study in Appendix B indicates that Green's theorem could provide a helpful solution.

1.3 Challenge and advance for internal multiple removal in anelastic media

Internal-multiple removal is a longstanding and very significant and only partially addressed problem in seismic exploration. Many methods (e.g., stacking, deconvolution, Radon transform, feedback loop, etc.) have been developed based on the assumptions of the data characteristic or the nature of the earth (Weglein and Dragoset, 2005). These methods are often effective when the assumptions are satisfied. However, as the petroleum industry moves to ever-more complex and challenging offshore and onshore plays, the assumptions behind those methods and providing detailed and accurate subsurface information have become (and will continue to be) increasingly difficult to satisfy. The inability to adequately provide that accurate and detailed subsurface information is a contributing factor to the breakdown and failure of seismic processing methods and subsequent dry holes during drilling. That drives the search for capabilities that will not require subsurface information

(Weglein, 2015; Ma, 2016).

Distinguished from all aforementioned methods, the inverse scattering series (ISS) method stands alone in its ability to predict all internal multiples with exact phase and approximate amplitude, and without any subsurface information or interpretive intervention (Carvalho, 1992; Weglein et al., 1997, 2003). Previous synthetic data tests on this algorithm have involved acoustic and elastic media (Coates and Weglein, 1996). However, the anelastic property (Q absorption and dispersion[8]) can be significant in many exploration regions. **Chapter 7** demonstrates with analytic and numerical examples that applying the ISS internal-multiple-attenuation method to anelastic data can achieve internal-multiple prediction with the correct time and approximate amplitude, without any subsurface elastic or anelastic properties (Wu and Weglein, 2014). This study adds to the theory that the ISS attenuator is model-type independent (Weglein et al., 2003).

For the ISS internal-multiple attenuation algorithm in an anelastic medium, there are two factors contributing to the amplitude difference between the predicted and the actual multiples: (a) the elastic transmission loss at interfaces above and at the interface where the internal multiple has downward reflection, and (2) the anelastic transmission loss due to the energy absorption in the layers above the interface where the first order multiple experiences its downward reflection. Note that if the medium is acoustic/elastic, only the first factor contributes to the amplitude prediction, and an ISS elimination algorithm developed by Zou and Weglein (2013, 2015) can surgically eliminate the internal multiple. Obviously, the second factor will contribute if the medium is absorptive and dispersive, possibly leading to a significantly smaller predicted amplitude than the actual multiple. **Chapter 8** proposes a modified attenuation method to remove the second factor by purposely incorporating a Q compensation to improve the prediction amplitude for an anelastic medium (Kostov et al., 2017).

[8] Q (or seismic quality factor) is used to quantify the effects of anelastic attenuation on the seismic wavelet caused by fluid movement and grain boundary friction.

2. A NEW METHOD FOR DEGHOSTING DATA COLLECTED ON A DEPTH-VARIABLE ACQUISITION SURFACE

2.1 Introduction

Deghosting is among the key steps in marine seismic data processing. Removing ghosts can boost low frequency and facilitate seismic broadband processing. In addition, effective deghosting is beneficial to all the subsequent processing tasks, e.g., multiple removal, imaging, and inversion. Among different deghosting methods, one unique advantage of the Green's theorem deghosting algorithm is that it can accommodate an arbitrary acquisition surface, e.g., horizontal, slanted, or undulating. However, it can only output deghosted data at a depth above the cable, but not on the receiver cable. The practical acquisition is always performed with a finite spatial sampling interval; therefore, a finite sum is utilized to numerically approximate the Green's theorem based spatial integral formula. As the output point comes close to the cable, the Green's function in the integrand becomes narrower and shrinks below what a finite-sampled sum for the integral can adequately approximate (Weglein et al., 2013). Consequently, with the application of this method, you achieve deghosting a new data that are at a new (shallower) depth; you cannot deghost the actual measured data on the cable itself. Furthermore, for those acquisitions (onshore or ocean bottom) at a boundary (air/earth boundary or water/earth boundary), a deghosting result right on the measurement surface is necessary.

If the measurement surface is horizontal, Green's theorem spatial-integral algorithm can be implemented in the wavenumber domain, which is equivalent to the $P - V_z$ method that is widely used today in the industry. In so doing, there is no problem of deghosting measured data. However, that procedure is not available with a non-horizontal measurement surface, e.g., a feathered cable in marine, or an experiment either at the earth's surface or at the ocean bottom with complicated topography.

In order to achieve an effective deghosting result on the actual measurement surface to deghost the acquired data, while accommodating the cable with an arbitrary shape, we propose a two-step strategy. The first step employs the current Green's theorem based deghosting algorithm and outputs the result at a depth which is shallower than the actual cable. The second step employs the Green's theorem one-way wave prediction; by doing so, the upgoing wave provided by the first step can be relocated from a shallower depth to the cable. We test the method with three datasets, one is acquired from a horizontal cable, and the other two are acquired from a non-horizontal cable. All examples show: (1) the effectiveness and the accuracy of this new deghosting method to accommodate an arbitrary cable and to separate the data right on the cable, and (2) its capability to deal with a rough sea situation and without requiring any information about the sea surface. We focus on the receiver-side deghosting, though it can be used to remove the ghosts at the source side as well. In a step further, the concept of this idea can be extended to both on-shore and ocean bottom acquisitions which can often have a significantly variable topography.

2.2 Theory of the two-step deghosting method

An experiment with receivers in the water column (Figure 2.1) is employed to describe how to deghost data right on the receiver cable that has an arbitrary shape. We first review the current Green's theorem deghosting method that is the first step of the new method. The second step is a Green's theorem based one-way wave prediction from the output of step one (that is above the cable) to a point on the cable.

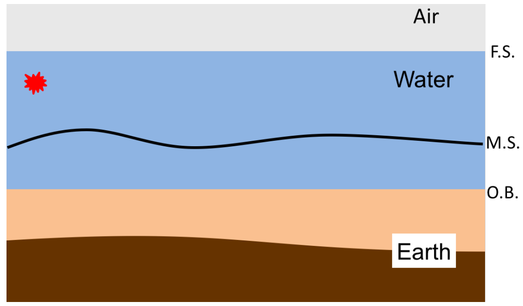

Fig. 2.1: Schematic of a marine experiment. Red star is an airgun, F.S. is free surface; M.S. is measurement surface; O.B. is ocean bottom.

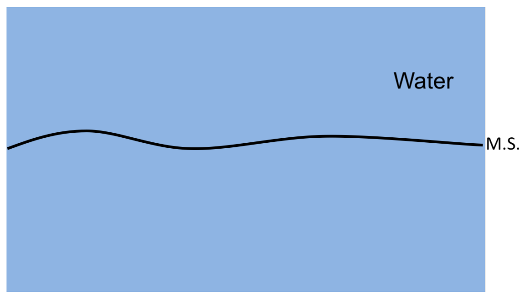

Fig. 2.2: A homogeneous whole-space acoustic reference.

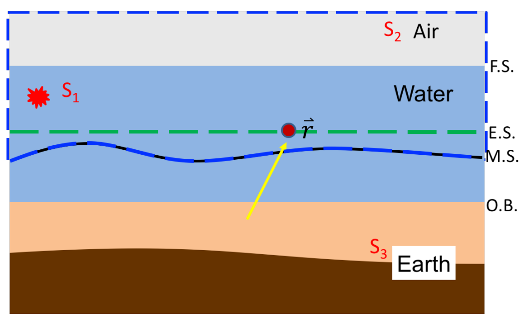

Fig. 2.3: Illustration of deghosting at point $\vec{r}$. E.S. is evaluation surface.

2.2.1 Step 1: Predicting deghosted data at a depth above cable

Basically, wave separation by using Green's theorem employs a model of the world that consists of the reference medium and the sources. The choice of reference medium will determine what the sources have to be in order to arrange for the reference medium and the sources together to correspond to the actual medium and to the experiment (Weglein et al., 2003). We choose the reference medium to be a homogeneous water whole space (Figure 2.2), whose properties are the same as the medium (Figure 2.1) along the measurement surface. There are three sources acting on the reference medium. As can be seen from Figure 2.3, S_1 is the energy source; S_2 is the air perturbation; and S_3 is the earth perturbation. We pick a point at $\vec{r}$ that is below S_1 and S_2 and above the cable. With a causal Green's function of the homogeneous whole-space reference medium, the contribution from S_1 and S_2 are both downgoing at $\vec{r}$, including the direct wave and its ghost, and the receiver-side ghosts; whereas the contribution from S_3 is the only upgoing portion. Therefore, separating the contribution due to S_1 and S_2 from that due to S_3 is actually separating the total wavefield at $\vec{r}$ into upgoing and downgoing. Following Morse and Feshbach (1953), Weglein and Secrest (1990), and Weglein et al. (2002), by selecting a closed semi-infinite surface (highlighted with the dashed blue line in Figure 2.3) that is bounded below by the measurement surface, making the Green's theorem based surface integral along the closed surface, and evaluating the result at $\vec{r}$ (it is inside the volume), will provide the contribution by the source outside the volume (S_3) to the total wavefield at a point ($\vec{r}$) inside the volume. For the location of $\vec{r}$ we have specified, the integral (Equation 2.1) outputs the entire upgoing portion of the total wavefield there. The receiver-side deghosting formula is (Zhang, 2007)

$$P^{up}(\vec{r},\omega) = \int\limits_{m.s.} [P(\vec{r}',\omega)\nabla' G_0^+(\vec{r}',\vec{r},\omega) - G_0^+(\vec{r}',\vec{r},\omega)\nabla' P(\vec{r}',\omega)] \cdot \hat{n} d\vec{r}', \tag{2.1}$$

where ω is the temporal frequency; P is the measured total pressure, and $\nabla' P$ is its gradient; $\hat{n}$ is a outward normal unit vector along the measurement surface; G_0^+ is the causal Green's function in the reference medium composed by a homogeneous whole-space of water; and the output P^{up} is the predicted receiver-side deghosted result at $\vec{r}$. The integral contribution is only along the measurement surface, because the contribution from other three infinite boundaries approaches zero by invoking the Sommerfeld radiation condition (Sommerfeld, 1949). Similarly, we can output the deghosted result at a series of points, along a fixed depth, called evaluation surface (E.S.) that is indicated with a green dashed line in Figure 2.3. This is the first step, using the acquired data at measurement surface to predict a receiver-side deghosted data at a shallower depth in comparison with the cable.

It is worth mentioning two points in terms of Equation 2.1. First, it effectively accommodates the cable with an arbitrary shape. Second, it is performed without any prior information about the "sources"; i.e., neither the source wavelet nor the passive sources are required. Specifically, the properties not assumed known include density, velocity, and the shape of the sources. Consequently, as well as accommodating a non-horizontal cable, it accommodates a sea surface with an arbitrary shape and without needing its shape and reflection there.

2.2.2 Step 2: Predicting deghosted data on the cable

To predict the deghosted/upgoing wave right on the cable, the Green's theorem based one-way wave prediction method is applied (Weglein et al., 2011a,b; Weglein, 2016). The basic concept can be described with a simple example, as plotted in Figure 2.4. There is a finite volume V with top boundary a and lower boundary b, where both pressure P and its normal derivative P_n are measured. Assuming a known property inside V, which is used to define the reference medium, then Green's theorem integral along a and b can predict the wavefield at any point inside V; e.g., at point $\vec{r}$. If we further assume the medium inside V is homogeneous and P inside is one-way and moving up, and an anti-causal Green's function G_0^- is used, then the wave prediction can be achieved with the integral on the top boundary a only (refer to Weglein (2016) for detail).

In a marine experiment, by using the upgoing wave at E.S. as input which is the output result of step 1, the upgoing wave at the cable can be predicted. As is shown in Figure 2.5, a finite volume enclosed by dashed blue line is selected, whose top boundary is E.S.. The cable is inside the volume. We assume the wavefield has been deghosted and it is going

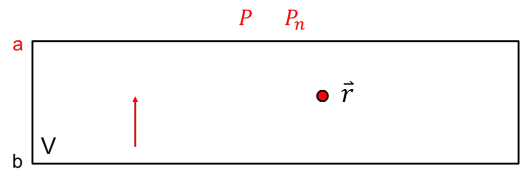

Fig. 2.4: A cartoon of wavefield prediction inside volume V.

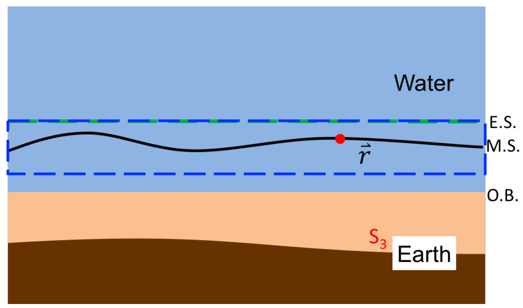

Fig. 2.5: Predicting deghosted data at $\vec{r}$ on the cable.

up inside the volume. By selecting a water whole space as the reference medium, S_3 (the earth perturbation) is the only source that contributes to the wavefield inside the volume. Similar to Figure 2.4, applying the integral (Equation 2.2) in terms of the G_0^- along E.S. and outputting the result inside the volume can predict the upgoing wave (e.g., at point $\vec{r}$ on the cable). The algorithm is

$$P^{up}(\vec{r},\omega) = -\int_{e.s.} [P^{up}(\vec{r}',\omega)\partial_{z'}G_0^-(\vec{r}',\vec{r},\omega) - G_0^-(\vec{r}',\vec{r},\omega)\partial_{z'}P^{up}(\vec{r}',\omega)]dx', \tag{2.2}$$

where $P^{up}(\vec{r}')$ and $P^{up}(\vec{r})$ are deghosted data at the evaluation surface and at the cable, respectively. This step deghosts data on the exact acquisition surface. There are several options to handle $\partial_{z'}P^{up}$. One is making $G_0^-(\vec{r}',\vec{r},\omega) = 0$ (Dirichlet boundary condition) when $\vec{r}'$ is on the E.S. to get rid of need of $\partial_{z'}P^{up}$.

2.3 Numerical tests

Three tests are conducted to examine the effectiveness of this two-step deghosting method. The first one is with a flat cable, while the others are with undulating cables. The first two are using flat sea surfaces, whereas the third one is with an undulating sea surface.

2.3.1 Example 1: Flat sea surface and flat cable

Figure 2.6 is the model to generate the data along a constant depth of 40 m. Although the $P - V_z$ method can deghost acquired data when the cable is horizontal, this new two-step method can accomplish the task as well.

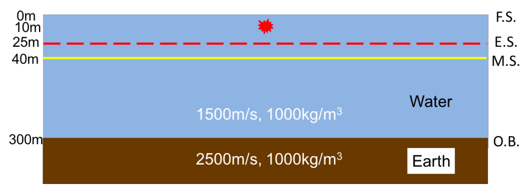

Fig. 2.6: A model with a horizontal sea surface and a flat cable. Source is at 10 m; E.S. is at 25 m.

Figure 2.7(a) is the total pressure. There are three events in the shot gather: the direct wave, the primary and the receiver-side ghost of the primary. For all these events, only primary is upgoing, which is expected to be separated from others. Notice that each event comes along with their source-side ghosts. We don't step into source-ghost removal (the same for the following two examples) in this chapter.

The first step predicts the deghosted data at a shallower depth (25 m), as shown in Figure 2.7(b), where only primary exists, the direct wave and the receiver ghost are extinguished. In the second step, we downward continue the intermediate result from step 1 to cable's depth of 40 m (in Figure 2.7(c)). The green dashed lines in the three figures locate the arrival time of the primary in the acquired data at offset 0m. It tells us that the result from step 1 is arriving later, while that from step 2 is having the same time as the acquired

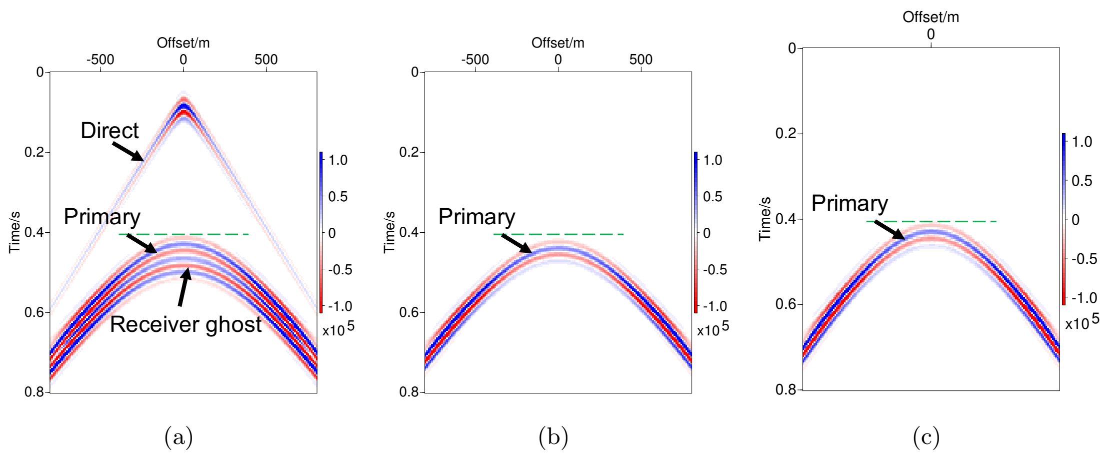

Fig. 2.7: Deghosting results with a flat free surface and a flat cable. (a) total pressure; (b) deghosted result at E.S.; (c) deghosted result at cable. Green lines locate the arrival time of primary. The color bars represent the amplitude (unit of N/m^2) of wavefield.

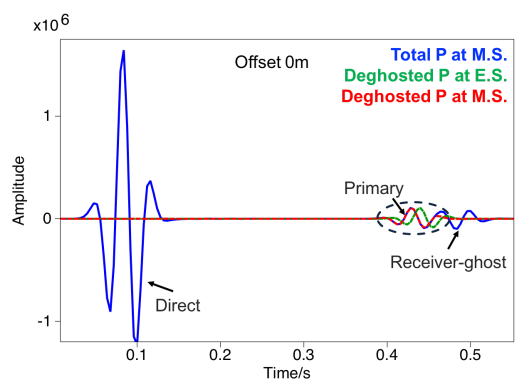

Fig. 2.8: Trace comparison at offset 0 m of Figure 2.7. The unit of amplitude is N/m^2.

primary. The single trace plot (in Figure 2.8) at offset 0 m illustrates the detail. In the black circle, the predicted primary from step 2 (marked with red) matches well with the primary (marked with blue) of data, whereas the result from step 1 (in green) arrives later.

2.3.2 Example 2: Flat sea surface and undulating cable

We generate data (Figure 2.10(a)) on a cable with a sine shape (centered at 40 m, and with an amplitude of 10 m). With a non-horizontal cable, the events in the data are not

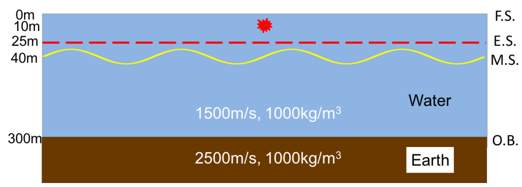

Fig. 2.9: A model with a flat free surface and an undulating cable centered at 40 m.

symmetric along the two sides of the source. Similar to Example 1, we first predict the upgoing wave at a depth of 25 m (Figure 2.10(b)). The intermediate output shot gather is symmetric for a horizontal reflector and horizontal output depth. Substituting it into step 2 predicts the deghosted data at the cable (Figure 2.10(c)). The deghosted portion of acquired data is finally achieved with satisfactory result. Instead of predicting a new deghosted dataset consisting of an up wave, which is what the current Green's theorem method (Equation 2.1) can deliver, this new two-step method predicts the deghosted data at the same location as the recorded data.

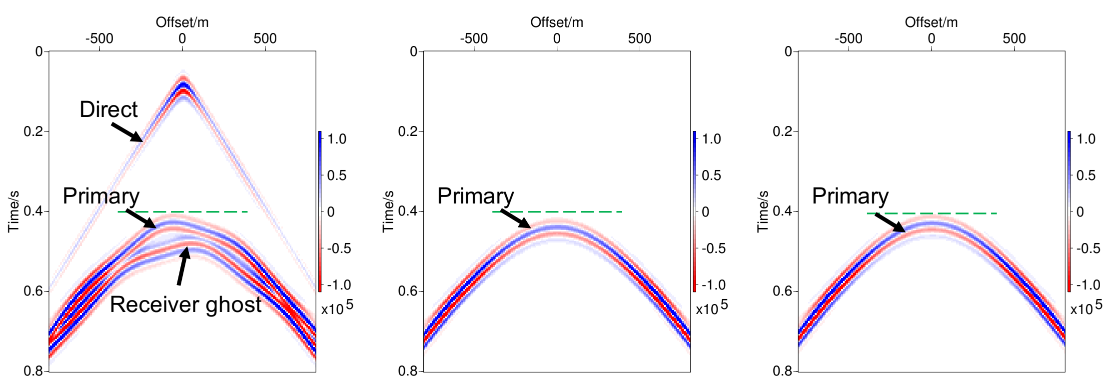

(a) (b) (c)

Fig. 2.10: Deghosting with a flat free surface and an undulating cable. (a) total pressure; (b) deghosted data at E.S.; (c) deghosted data at cable. Green lines locate the arrival time of primary. The color bars represent the amplitude (unit of N/m^2) of wavefield.

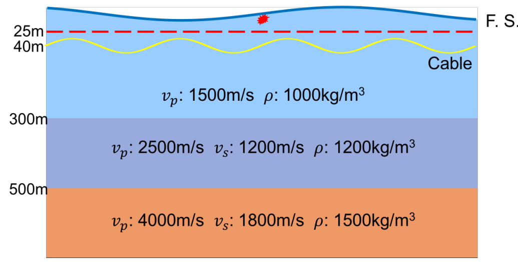

Fig. 2.11: A model with an undulating free surface centered at 0 m and an undulating cable centered at 40 m.

2.3.3 Example 3: Undulating sea surface and undulating cable

In this example, we consider a rough sea case and a non-horizontal cable (Figure 2.11). The earth below the ocean bottom is elastic. We generate data (Figure 2.12(a)) with all the information about the sea surface, the cable and the medium properties. However, only the cable's shape and the water property are needed for the deghosting calculation. The method doesn't need to know the shape of the ocean top, the ocean bottom, and the properties of the elastic earth. We predict the upgoing wave at a depth of 25 m in step 1 (Figure 2.12(b)). Substituting the up wave at 25 m into Green's theorem one-way wave-prediction algorithm, the deghosted portion of the acquired data (Figure 2.12(c)) can be achieved. A trace plot at offset 0 m (Figure 2.13) further shows detail. This example illustrates that the method is independent of earth model type.

2.4 Conclusion

The ability to effectively remove ghosts has a positive impact on subsequent processing and interpretation, that can support effective drilling decisions. We provide a two-step strategy that combines the usages of Green's theorem based wave separation and wave prediction algorithms. The new method can successfully deghost actual acquired data at the acquisition depth, without assuming a horizontal measurement surface. As a useful tool, this study extends the capability of current Green's theorem wave separation method

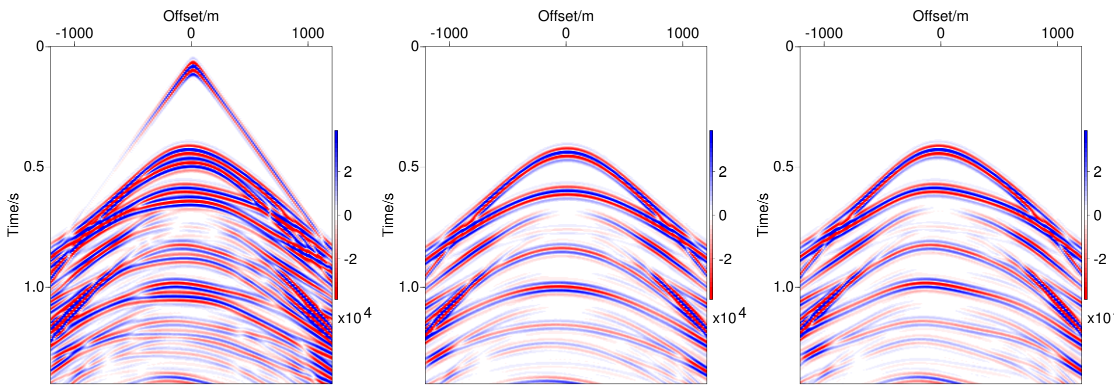

(a) (b) (c)

Fig. 2.12: Deghosting result with an undulating sea surface and an undulating cable. (a) total pressure; (b) deghosted data at E.S.; (c) deghosted data at cable. The color bars represent the amplitude (unit of N/m^2) of wavefield.

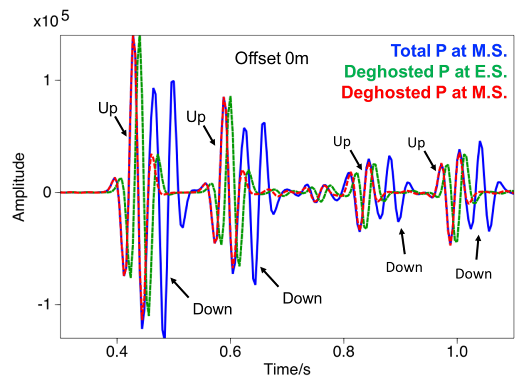

Fig. 2.13: Trace comparison at offset 0 m of Figure 2.12. The unit of amplitude is N/m^2.

towards seismic onshore and ocean-bottom exploration with complicated topography.

3. PREDICTING DEGHOSTED PRESSURE AND MULTICOMPONENT DISPLACEMENT AT THE OCEAN BOTTOM

3.1 Introduction

Ocean bottom acquisition is used in offshore exploration to improve the signal-to-noise ratio, providing a quieter seafloor environment compared to conventional streamer data acquisition. However, the ghost problem is usually more serious for ocean bottom measurements. The destructive interference between the ghosts and the upgoing reflection data can lead to notches. The deeper the depth, the lower the frequency the first non-zero notch can touch. Here is a simple example to illustrate the significance and issue (Weglein et al., 2013). The frequency of the first non-zero notch can be approximately $f = c/(2z)$ at near offset, where c is water speed, and z is the depth of streamer. For typical towed streamer data at 6 m, a non-zero notch occurs at 125 Hz, which is usually outside data spectrum; however, for ocean bottom data at 150 m, the first non-zero notch can come in at 5 Hz. This example indicates that ghost is a serious problem for ocean bottom data since the notches are inside the seismic bandwidth. Therefore, deghosting the reflection data is an essential step in ocean bottom data analysis. In addition, deghosting is an important prerequisite for the inverse scattering algorithms to remove free surface and internal multiples. One step further, it is also asked so as to enhance structural analysis and amplitude analysis.

This chapter will introduce the Green's theorem based deghosting theory to the ocean bottom acquisition (Wu and Weglein, 2016b), deghosting both pressure data and multicomponent displacement data that can be measured at the seabed. Inherently, Green's theorem based wave separation method starts with a reference medium for the interest of a certain purpose and characterizes the difference between the actual world and reference medium as sources. Within the wave separation task, different applications call for different choices of reference medium. Taking ocean bottom data as an example, we assume both hydrophones and multicomponent geophones are utilized for acquisition. The hydrophones collect pressure component slightly above the ocean bottom, whereas the geophones measure the displacement components along different directions in the earth sediment, slightly below the ocean bottom. Then, based on the same general wave separation idea from Green's theorem, the pressure data deghosting employs a whole space of water as reference (Zhang and Weglein, 2006), while the displacement data deghosting adopts a whole space of elastic medium. This application essentially requires multicomponent data with no assumption or limitation of acquisition topography.

We begin by summarizing the ocean bottom acquisition geometry to be used in the chapter. Then the deghosting methodology to ocean bottom data will be described in detail. Finally, as a special case, a synthetic example with a horizontal ocean bottom is presented to show the effectiveness of the methods for deghosting pressure and displacement data, respectively.

3.2 Ocean bottom acquisition and boundary condition

As is shown in Figure 3.1, a generic ocean bottom experiment is deployed on a model consisting of an air half-space, and a finite depth of water, and then the heterogeneous earth (the colors of orange and brown represent different properties). An airgun (indicated by the red star in Figure 3.1) is located in the water. We put hydrophones right above the ocean bottom to measure the pressure (P) of water and put geophones slightly below the ocean bottom to measure multicomponent wave displacement ($\vec{u}$) of the earth. The displacements contain both longitudinal (P) waves and transverse (S) waves, which is a unique benefit provided by the ocean bottom acquisition in comparison with the towed streamer acquisition.

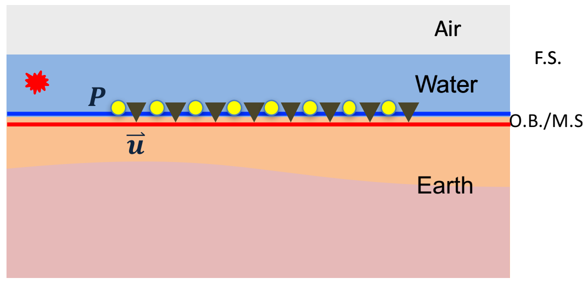

Fig. 3.1: Ocean bottom experiment. Yellow circles denote hydrophones; green triangles denote geophones. F.S. is free surface, or air/water boundary; M.S. is measurement surface; O.B. is ocean bottom; P is pressure; $\vec{u}$ is displacement.

Along the two sides of the ocean bottom, traction and displacement satisfy respective boundary conditions. Displacements are continuous along normal direction. Along both normal direction and tangential direction, tractions have the same values while towards opposite directions. Hence,

$$u_{\mathbf{wn}} = \vec{u}_{\mathbf{w}} \cdot \hat{n} = \vec{u} \cdot \hat{n}, \tag{3.1}$$

where $\vec{u}_w$ is the displacement in the water at the ocean bottom, with its normal component $u_{\mathbf{wn}}$, $\vec{u}$ is the measured multicomponent displacement of earth, and $\hat{n}$ is the normal unit vector towards the lower side.

$$\vec{t}_{\mathbf{e}} = -P\hat{n}, \tag{3.2}$$

where $\vec{t}_{\mathbf{e}}$ is traction at ocean bottom in the earth, and P is the measured pressure component of water. Traction is zero along the tangential direction, assuming that water is an ideal fluid.

3.3 The theory of predicting the deghosted ocean bottom data

We will describe how Green's theorem wave separation is adopted to the ocean bottom experiment, deghosting both the pressure data and the multicomponent displacement data.

Both pressure and displacement components are required as input to deghost either one.

3.3.1 Green's theorem based pressure deghosting

To deghost the pressure data that are acquired in water and slightly above the ocean bottom, the theory is the same as deghosting the conventional towed streamer data. The detail refers to Chapter 2.2.1.

Using the definition of pressure and the Newton's law,

$$\frac{\partial P}{\partial n} = \rho \omega^2 u_{\mathbf{wn}}, \tag{3.3}$$

where ρ is water's density, ω is temporal frequency, $\frac{\partial P}{\partial n}$ is the gradient of pressure along the normal direction.

Combining Equation 3.1 and 3.3, the Green's theorem 2.1 method for deghosting the ocean bottom pressure data is

$$\begin{aligned} P^{up}(\vec{r},\omega) &= \int_{m.s.} [P(\vec{r}\,',\omega)\nabla' G_0^+(\vec{r}\,',\vec{r},\omega) - G_0^+(\vec{r}\,',\vec{r},\omega)\nabla' P(\vec{r}\,',\omega)] \cdot \hat{n} d\vec{r}\,' \\ &= \int_{m.s.} [P(\vec{r}\,',\omega)\frac{\partial G_0^+(\vec{r}\,',\vec{r},\omega)}{\partial n} - \rho\omega^2 G_0^+(\vec{r}\,',\vec{r},\omega) u_{\mathbf{wn}}(\vec{r}\,',\omega)] d\vec{r}\,', \end{aligned} \tag{3.4}$$

where $\vec{r}\,'$ denotes receiver point, $\vec{r}$ denotes output point; G_0^+ is the causal scalar Green's function in the reference medium of water; P^{up} is the predicted upgoing (receiver side deghosted) wave. Noting that the displacement data provide the normal derivative of pressure, which is required for the integral algorithm.

We can further locate the output point on the measurement surface and deghost the recorded pressure data with the method in Chapter 2.

3.3.2 Green's theorem based displacement deghosting

To deghost the displacement data that are acquired in earth sediment and slightly below the ocean bottom, the reference medium is selected as a homogeneous elastic whole space (see Figure 3.2), whose property agrees with the actual earth along the measurement surface and that is indicated by orange. We here assume the property right below the ocean bottom is homogeneous and known. There are four sources (Figure 3.3) acting on the reference medium: S_1 is energy source; S_2 is the air perturbation above the air/water boundary; S_3 is the perturbation of water between the air/water boundary and the ocean bottom; S_4 is the earth perturbation deviating from the reference earth. Similar to the theory for deghosting pressure data, Green's theorem based surface integration along the measurement surface can predict the portion of the wavefield inside the enclosed volume (e.g., at point $\vec{r}$) that is caused by source S_4 and is going up.

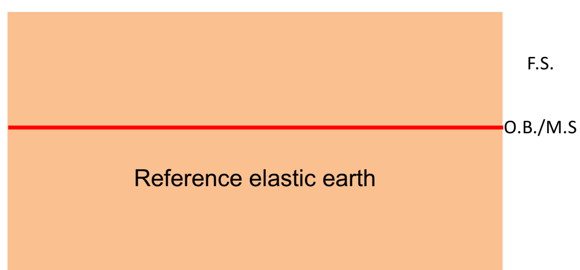

Fig. 3.2: A homogeneous whole-space elastic reference medium for deghosting the displacement data. Abbreviations same as those used in Figure 3.1.

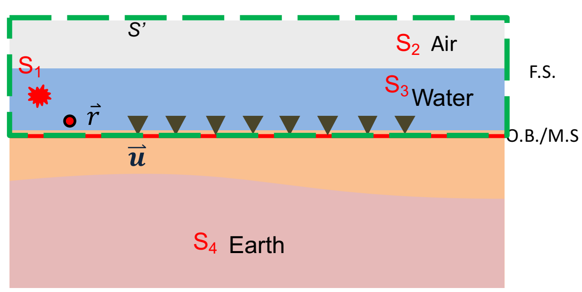

Fig. 3.3: Surface integral along S' extracts the contribution from S_4 for output point $\vec{r}$ inside volume.

Green's theorem deghosting algorithm for displacement data (Appendix C) is (by combining boundary condition of Equation 3.2)

$$\begin{aligned}
&\vec{u}^{up}(\vec{r},\omega) \\
&= -\int_{m.s.} [\vec{t_{\mathbf{e}}}(\vec{r}\,',\omega)\cdot \boldsymbol{G}_0^{+}(\vec{r}\,',\vec{r},\omega) - \vec{u}(\vec{r}\,',\omega)\cdot(\hat{n}\cdot\boldsymbol{\Sigma}_0^{+}(\vec{r}\,',\vec{r},\omega))]d\vec{r}\,' \\
&= \int_{m.s.} [P(\vec{r}\,',\omega)\hat{n}\cdot \boldsymbol{G}_0^{+}(\vec{r}\,',\vec{r},\omega) + \vec{u}(\vec{r}\,',\omega)\cdot(\hat{n}\cdot\boldsymbol{\Sigma}_0^{+}(\vec{r}\,',\vec{r},\omega))]d\vec{r}\,',
\end{aligned} \tag{3.5}$$

where $\boldsymbol{G}_0^{+}$ is causal Green's displacement tensor, $\boldsymbol{\Sigma}_0^{+}$ is Green's stress tensor; $\vec{u}^{up}$ is the predicted upgoing (receiver-side deghosted) wave. $\cdot$ denotes a tensor product. To removal the ghost of displacement data, the pressure data are substituted into the algorithm to meet the requirement of the "derivative of displacement" (traction can be expressed in terms of the derivative of displacement).

A short discussion: for point $\vec{r}$ in the water column, the contribution from source of water perturbation S_3 includes both upgoing and downgoing. Consequently, the predicted upgoing wave at $\vec{r}$ due to S_4 is not total/only upgoing portion. It is not a rigorous up/down separation at $\vec{r}$. If the ocean bottom is horizontal or smoothly varying, and we locate the output point $\vec{r}$ on the measurement surface (slightly below the ocean bottom), then the contribution from S_3 is downgoing and contribution from S_4 is the only up. Otherwise, if the ocean bottom is not horizontal, what Equation 3.5 produces is not total upgoing wave even the output point $\vec{r}$ is on the measurement surface. That is because there is a piece of water perturbation contributing to the upgoing portion at $\vec{r}$. Although the total upgoing portion of measured data is generated by both the earth perturbation and a part of the water perturbation, the purpose for seismic deghosting is to extract the upgoing waves from the earth where potential reservoir exists. Hence, my view is that Equation 3.5 or a further step to locate the output on the actual measurement has already provided the expected result.

3.4 Numerical examination

In this section, we conduct a 2D line source experiment as an example to illustrate the performance of Green's theorem in the separation of pressure just above the ocean bottom, and separation of displacements just below the ocean bottom into their upgoing and downgoing portions, respectively. The model is shown in Figure 3.4, and the parameters are listed in Table 3.1. The output point $\vec{r}$ is on the measurement surface by applying the wave separation formula in (k_x, ω) domain.

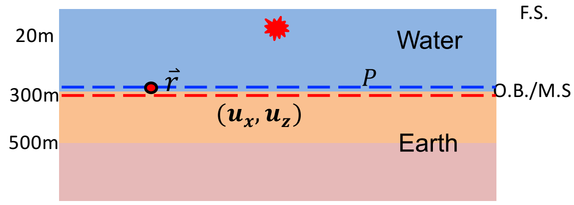

Fig. 3.4: Synthetic model for numerical test. Symbol same as Figure 3.1.

Layer Number	P-Velocity (m/s)	S-Velocity (m/s)	Density (kg/m^3)
1(water)	1500	0	1000
2(top earth)	2500	1200	1200
3(bottom earth)	4000	1800	1500

Tab. 3.1: The parameters of the model in Figure 3.4.

3.4.1 Pressure wave deghosting

The wave separation results of pressure data are shown in Figure 3.5. By subtracting the predicted upward waves (Figure 3.5 (b)) from the total waves (Figure 3.5 (a)), we obtain the downward waves (Figure 3.5 (c)). Several early-arriving events (depicted with yellow arrows) of upgoing and downgoing waves are selected to plot the ray paths to understand their meanings. The ray plots are illustrated in Figure 3.6, where the measurement surface is plotted slightly above the ocean bottom for the convenience of comparison; however, the measurement surface is actually right sitting on the ocean bottom. Therefore, there are up wave and down wave pairs, such as $U1/D1$, $UM1/DM1$ and $UM2/DM2$, which have the same arriving times. There is no corresponding downgoing wave to the upgoing wave $U2$, the primary from the second reflector; hence at the time zone of $U2$, the downgoing wave in Figure 3.5(c) is blank. $U2$, $UM2$, and $DM2$ consist of three events. It is because in the elastic layer right beneath the seafloor, the wavefield can propagate with either P wave or S wave. There are four possible propagation histories in the elastic layer: $\grave{P}\acute{P}$, $\grave{P}\acute{S}$, $\grave{S}\acute{P}$, and $\grave{S}\acute{S}$, where ` is for downward propagation and ´ is for upward. $\grave{P}\acute{S}$ and $\grave{S}\acute{P}$ have the same travel times in the horizontal homogeneous elastic layer.

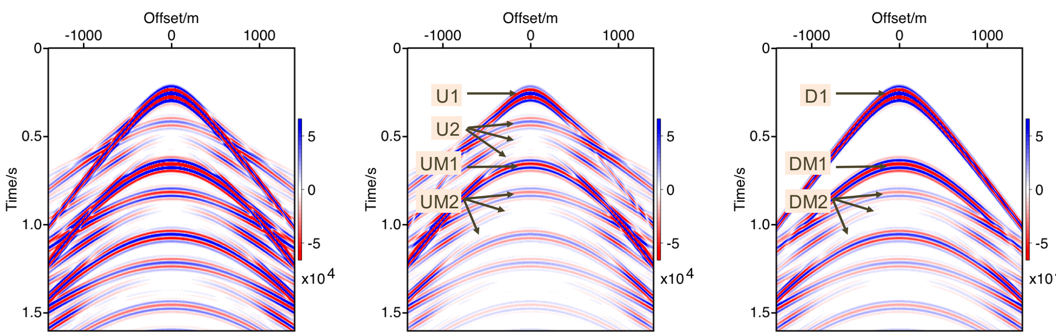

(a) P (b) P^{up} (c) P^{down}

Fig. 3.5: Wave separation on pressure field. (a) for total waves; (b) for up waves; (c) for down waves. The color bars represent the amplitude (unit of N/m^2) of wavefield.

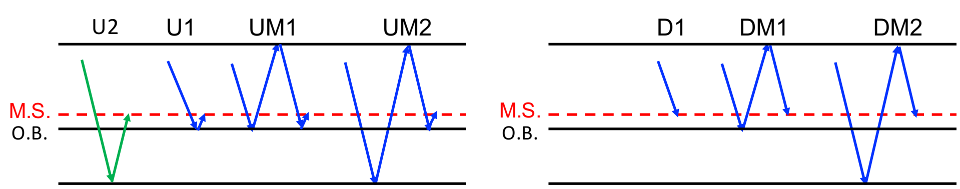

(a) P^{up} (b) P^{down}

Fig. 3.6: The ray path plots of depicted events in Figure 3.5. (a) is up wave; (b) is down wave.

3.4.2 Displacement wave deghosting

The wave separation results of multicomponent displacements are shown in Figure 3.7 for x component and Figure 3.8 for z component. The down waves are obtained by subtracting the separated upgoing waves from the total wavefield. To further understand the results, the z component results are selected to analyze the ray path of early arriving events (depicted with yellow arrows). The ray plots are shown in Figure 3.9, where the measurement surface is put slightly below the ocean bottom so that we can see clearly the downgoing waves whose last reflections happen at the ocean bottom; however, the measurement surface is actually right beneath the ocean bottom. Similarly, the up wave and down wave pairs, such as $U2/D2$, and $UM2/DM2$, arrive simultaneously. The downgoing waves, all the propagation is within the water layer, have no companion up waves; thereby, at the time zones of $D1$, $DM1$, and $DM11$, the upgoing wave plot in Figure 3.8(b) is blank. Besides, there are internal multiples in the shot records and two events are pointed out by the red arrows in Figure 3.8(b).

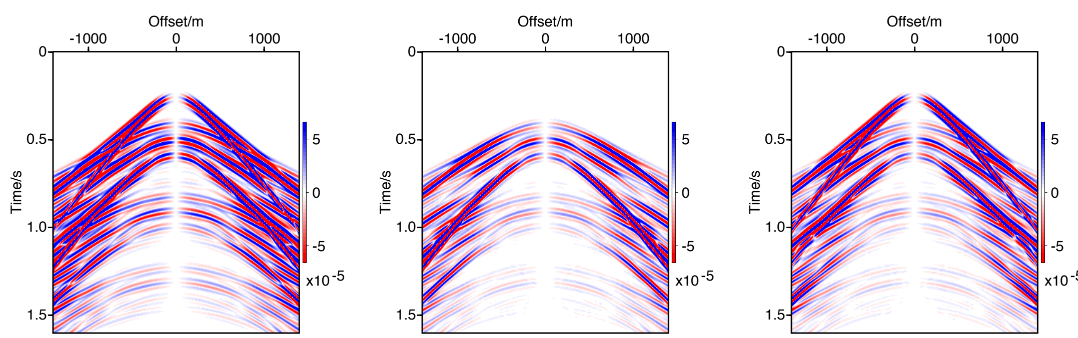

(a) U_x (b) U_x^{up} (c) U_x^{down}

Fig. 3.7: Wave separation on x component of displacement field. (a) is total wave; (b) is up wave; (c) is down wave. The color bars represent the amplitude (unit of m) of wavefield.

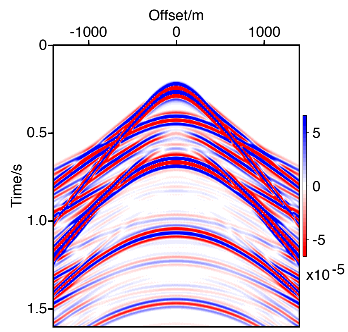

(a) U_z (b) U_z^{up} (c) U_z^{down}

Fig. 3.8: Wave separation on z component of displacement field. (a) is total wave; (b) is up wave; (c) is down wave. The color bars represent the amplitude (unit of m) of wavefield.

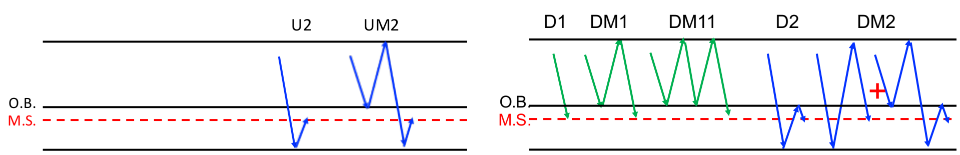

(a) U_z^{up} (b) U_z^{down}

Fig. 3.9: The ray path plots of depicted events in Figure 3.8. (a) is up wave; (b) is down wave.

3.5 Conclusion

By choosing appropriate reference media, the Green's theorem wave separation concepts can be extended and applied to ocean bottom data. This method can effectively separate the pressure, and the multicomponent displacements, into their up and down parts. We provide a general wave separation formula which has three advantages: (1) it doesn't require source information; (2) it works on one experiment at a time, with a low computational cost; (3) it can accommodate the measurement surface without any topographic assumption, and is well suited for complicated ocean bottom problems. The synthetic example in this chapter using a horizontally layered model indicates that the algorithm works yielding positive and encouraging results.

4. ONSHORE PREPROCESSING IN THE PS SPACE: GROUND ROLL REMOVAL AND DEGHOSTING

4.1 Introduction

Onshore seismic exploration and processing seek to use reflection data (the scattered wavefield) to detect the subsurface information. However, the measured total wavefield consists of the reflection data and the reference wave. Reflection data contain the surface wave (also named as ground roll); hence, it is necessary to separate the reference wave and the scattered wave. Traditional filtering methods may damage the reflection data, especially where ground roll interferes with the reflection data; meanwhile, the separated ground roll is injured as well.

In addition, reflection data contain ghosts, which are preferred to be separated out too. The receivers (typically geophones) employed in land experiments can be either close to the air/earth surface as a conventional survey, or beneath the air/earth surface with a predetermined depth (known as buried receivers) that is usually used for a 4D application (Liang and Keho, 2015). In either case, not only upgoing waves are in the reflection data, there are also receiver-side ghosts, which correspond to the events ending their propagating histories with downward reflection at the receiver side. The mainstream processing techniques prefer to process the upgoing portion of reflection data; hence, deghosting is another important issue as well as ground roll removal that has to be solved. In the case of buried source (e.g., the Dynamite), ghosts can exist at the source side, and start the propagation upward to the air/earth boundary. In this study, we will assume that the source is located slightly above the air/earth boundary (it could be infinitely close, or actually on, the air/earth boundary), so there are receiver-side ghosts but no source-side ghosts.

Green's theorem provides a method to achieve two goals – identification and removal of the reference wave (including ground roll onshore) without damaging the reflection data, and removal of the ghosts without damaging the upgoing reflection data. For onshore plays, the extended elastic Green's theorem wave separation method is applicable for data either in PS space where displacement is decomposed into P and S components or in the displacement space directly. The choice of data space (either the PS space or the displacement space) depends on the convenience to the subsequent processing objectives (Matson, 1997).

This chapter focuses on describing an elastic Green's theorem based wave separation method for land data in the PS space. Chapter 5 will explain the algorithm for data in the displacement space. Application of the algorithm presented in this chapter can essentially achieve two goals. Firstly, with a choice of reference medium to be composed by a half-space of air over a half-space of the elastic earth, the reference wave (including ground roll) and the scattered wave can be separated. Secondly, by choosing a homogeneous elastic whole space as the reference medium, we can further remove the ghosts from the scattered wave. To achieve either step, there is no need for any prior information about the impulse source. The algorithm applies to one experiment for each time; i.e., wave separation is carried out on its own for each shot record. As a result, the method studied in this chapter possesses its superiority in terms of data requirement and computational efficiency. In addition, the algorithm, as an integral along the acquisition surface, doesn't assume the shape of the measurement, which is free with an arbitrary shape. Thus property is important and useful when the topography of the earth's surface is complicated and the measurement is deployed right beneath that. The synthetic examinations on a model with layered earth demonstrate the effectiveness of the method to be able to separate the reference wave and reflection data and remove the ghosts in a further step, and meanwhile retain the upgoing reflection data.

4.2 Background of 2D elastic wave theory

The elastic wave separation method starts with the elastic formulation. For convenience, the basis is changed from $\vec{u} = \begin{pmatrix} u_x \\ u_z \end{pmatrix}$ to $\boldsymbol{\Phi} = \begin{pmatrix} \phi^P \\ \phi^S \end{pmatrix}$. $\vec{u}$ represents the displacement that consists of x and z components; $\boldsymbol{\Phi}$ has isolated P-wave and S-wave components. We here take 2D case as an example to show the wave separation theory and its application, which can be extended to 3D situation. Below is a brief review of 2D elastic wave theory.

In the PS space, the basic wave equations (Weglein and Stolt, 1995; Zhang, 2006) are

$$\begin{aligned} &\hat{\boldsymbol{L}}\boldsymbol{\Phi} = \boldsymbol{F}, \\ &\hat{\boldsymbol{L}}\hat{\boldsymbol{G}} = \delta, \\ &\hat{\boldsymbol{L}}\hat{\boldsymbol{G}} = \delta, \\ &\hat{\boldsymbol{L}}_{\boldsymbol{0}}\hat{\boldsymbol{G}}_{\boldsymbol{0}} = \delta, \\ &\hat{\boldsymbol{V}} = \hat{\boldsymbol{L}}_{\boldsymbol{0}} - \hat{\boldsymbol{L}}, \end{aligned} \tag{4.1}$$

where $\hat{\boldsymbol{L}}$ and $\hat{\boldsymbol{L}}_{\boldsymbol{0}}$ are the differential operators that describe the wave propagation in the actual medium and the reference medium, respectively; $\boldsymbol{F}$ is the source term; $\hat{\boldsymbol{G}}$ and $\hat{\boldsymbol{G}}_{\boldsymbol{0}}$ are the corresponding Green's operators for the actual and reference media. $\hat{\boldsymbol{V}}$ is the perturbation operator.

4.3 Green's theorem wave separation algorithm in the PS space

The theory of Green's theorem based wave separation method in the PS space is derived in this section. We begin with a brief explanation of generic land experiment; then explain how the concept of Green's theorem wave separation is employed to achieve two objectives: (1) the separation of reference waves and scattered waves, and (2) the removal of receiver-side ghosts (refer Appendix E for theoretical derivation).

4.3.1 Description of a generic earth model

As is shown in Figure 4.1, the generic onshore model consists of an air half space and an elastic earth half space. Receivers highlighted by green triangles are plugged into the earth. The measurement surface (the location of receivers) can be close to the air/earth surface as in the case of on-surface-receiver acquisition; it can also be of several meters below the air/earth surface for a buried-receiver survey. For either situation, the receivers are coupled with the elastic medium. The geophones record the particles' vibration in their vicinity area and transfer it to be a signal of the multicomponent displacement (u_x, u_z). With the basis transform from displacement to PS space, that is described in Appendix D, the collected data at receiver side can be expressed in form of (ϕ^P, ϕ^S). We assume that the source is located slightly above the air/earth boundary, could be infinitely close to that boundary. Because the source exists in the air, it is a P-type source and there is no source-side ghost.

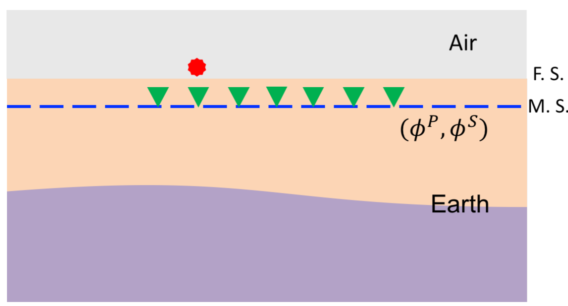

Fig. 4.1: A generic model describing the onshore experiment. F.S., air/earth boundary; M.S., the measurement surface and marked with a blue dashed line; the red star, energy source slightly above the F.S.; green triangles, receivers measuring the wavefield in the PS space.

4.3.2 Reference wave and scattered wave separation in the PS space

In exploration seismology, it is useful for us to choose the reference medium to agree with the actual earth at and above the measurement surface. If the near-surface properties in the actual earth are homogeneous and known, the simplest reference medium can be chosen as two discontinuous half spaces, with a half-space of homogeneous air over a half-space of the homogeneous elastic earth (see Figure 4.2). There are two sources on the selected reference medium (see Figure 4.3 and Figure 4.4). S_1 is the energy source; acting on the reference medium, it generates the reference wave. S_2 is the earth perturbation (or passive source), representing the difference between the actual earth (highlighted in purple) and the reference earth (highlighted in orange) below the measurement surface; acting on the reference medium, it generates the scattered wave (also known as the reflection data).

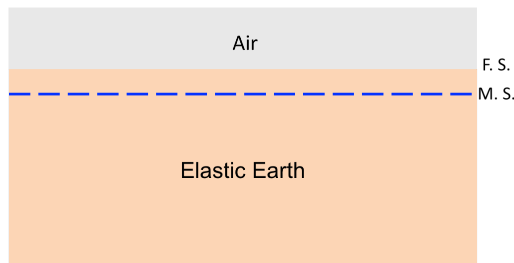

Fig. 4.2: Reference medium for separating the reference wave and the scattered wave.

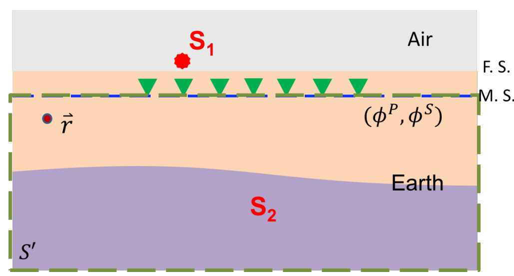

Fig. 4.3: Illustration of reference wave prediction with a surface integral along S'; $\vec{r}$ is the evaluation (output) point below M.S..

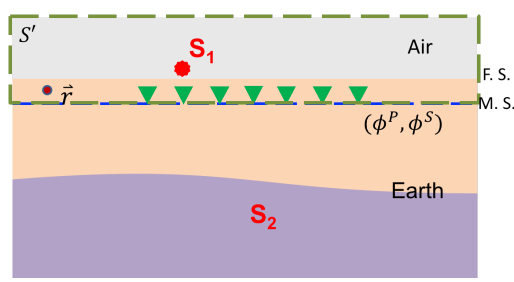

Fig. 4.4: Illustration of scattered wave prediction with a surface integral along S'; $\vec{r}$ is the evaluation (output) point above M.S..

The reason why Green's theorem derived integral algorithm can achieve wavefield separation can be explained by comparing it with the Lippmann-Schwinger equation (Weglein and Secrest, 1990). The exhaustive derivation can be found in Appendix F. For this specific experiment, choosing a closed semi-infinite surface S' (highlighted by dark green in Figure 4.3) bounded above by the measurement surface, and evaluating (or outputting) the Green's theorem based surface integral at any point inside the volume, the contribution due to source outside the volume (it is S_1) to the total field at that point can be predicted. With a causal Green's function of the reference medium, source S_1 generates reference wave at any point inside the volume. Hence, in this case, with the output point at $\vec{r}$ inside the volume which is below the measurement surface, the integral algorithm can predict the reference wave $\mathbf{\Phi}_0$ at $\vec{r}$. The reference wave includes both the direct wave and the surface wave. Oppositely, choosing a closed semi-infinite surface S' (highlighted by dark green in Figure 4.4) bounded below by the measurement surface, and evaluating (or outputting) the Green's theorem based surface integral at any point above the measurement surface, the contribution due to source outside the volume (it is S_2) to the total field at that point (for example at point $\vec{r}$) can be predicted, which is the scattered wave $\mathbf{\Phi}_s$, or the reflection data.

The Green's theorem formulas for separating reference waves and scattered waves in the space-frequency domain are

$$\begin{aligned}
\mathbf{\Phi}_0(\vec{r},\vec{r}_s,\omega) &= \int_{m.s.} \Big(\mathbf{\Phi}(\vec{r}\,',\vec{r}_s,\omega)\cdot\nabla'\hat{\boldsymbol{G}}_0(\vec{r}\,',\vec{r},\omega) - \nabla'\mathbf{\Phi}(\vec{r}\,',\vec{r}_s,\omega)\cdot\hat{\boldsymbol{G}}_0(\vec{r}\,',\vec{r},\omega)\Big)\cdot\hat{n}d\vec{r}\,' \\
&\qquad\qquad\qquad\qquad\qquad\qquad\qquad\qquad\qquad\qquad\text{for } \vec{r} \text{ below the M.S.,} \\
\mathbf{\Phi}_s(\vec{r},\vec{r}_s,\omega) &= \int_{m.s.} \Big(\mathbf{\Phi}(\vec{r}\,',\vec{r}_s,\omega)\cdot\nabla'\hat{\boldsymbol{G}}_0(\vec{r}\,',\vec{r},\omega) - \nabla'\mathbf{\Phi}(\vec{r}\,',\vec{r}_s,\omega)\cdot\hat{\boldsymbol{G}}_0(\vec{r}\,',\vec{r},\omega)\Big)\cdot\hat{n}d\vec{r}\,' \\
&\qquad\qquad\qquad\qquad\qquad\qquad\qquad\qquad\qquad\qquad\text{for } \vec{r} \text{ above the M.S.,}
\end{aligned} \tag{4.2}$$

where $\mathbf{\Phi}_0 = \begin{pmatrix} \phi_0^P \\ \phi_0^S \end{pmatrix}$, $\mathbf{\Phi}_s = \begin{pmatrix} \phi_s^P \\ \phi_s^S \end{pmatrix}$, and $\hat{\boldsymbol{G}}_0(\vec{r}\,',\vec{r},\omega)$ is causal Green's function in a reference medium composed by an air half space over an elastic half space. $\hat{n}$ is a outward normal unit vector along the measurement surface. $\cdot$ represents tensor product. The integral contribution is only along the measurement surface, because the contribution from other three infinite boundaries approaches zero by invoking the Sommerfeld radiation condition (Sommerfeld, 1949).

The analytic $\hat{\boldsymbol{G}}_0(\vec{r}', \vec{r}, \omega)$ is

$$
\begin{aligned}
\hat{\boldsymbol{G}}_0(\vec{r}', \vec{r}, \omega) &= \begin{pmatrix} \hat{G}_0^P(\vec{r}', \vec{r}, \omega) + \hat{G}_0^{PP}(\vec{r}', \vec{r}, \omega) & \hat{G}_0^{PS}(\vec{r}', \vec{r}, \omega) \\ \hat{G}_0^{SP}(\vec{r}', \vec{r}, \omega) & \hat{G}_0^S(\vec{r}', \vec{r}, \omega) + \hat{G}_0^{SS}(\vec{r}', \vec{r}, \omega) \end{pmatrix} \\
&= \frac{1}{2\pi} \int e^{ik_x(x'-x)} dk_x \left[\begin{pmatrix} \frac{e^{i\nu_2|z'-z|}}{2i\nu_2} & 0 \\ 0 & \frac{e^{i\eta_2|z'-z|}}{2i\eta_2} \end{pmatrix} + \begin{pmatrix} \acute{P}\grave{P}\frac{e^{i\nu_2 z}e^{i\nu_2 z'}}{2i\nu_2} & \acute{S}\grave{P}\frac{e^{i\eta_2 z}e^{i\nu_2 z'}}{2i\eta_2} \\ \acute{P}\grave{S}\frac{e^{i\nu_2 z}e^{i\eta_2 z'}}{2i\nu_2} & \acute{S}\grave{S}\frac{e^{i\eta_2 z}e^{i\eta_2 z'}}{2i\eta_2} \end{pmatrix} \right],
\end{aligned}
\tag{4.3}
$$

where $\acute{P}\grave{P}$, $\acute{P}\grave{S}$, $\acute{S}\grave{P}$, $\acute{S}\grave{S}$ represent the reflection coefficients along the air/elastic-earth boundary, the subscript 2 represents the elastic half space of the reference medium, and

$$
\nu_2 = \begin{cases} \sqrt{k_{\alpha_2}^2 - k_x^2} & \text{if } k_x < k_{\alpha_2} \\ i\sqrt{k_x^2 - k_{\alpha_2}^2} & \text{if } k_x > k_{\alpha_2} \end{cases} \qquad k_{\alpha_2} = \frac{\omega}{\alpha_2},
$$

$\eta_2 = \begin{cases} \sqrt{k_{\beta_2}^2 - k_x^2} & \text{if } k_x < k_{\beta_2} \\ i\sqrt{k_x^2 - k_{\beta_2}^2} & \text{if } k_x > k_{\beta_2} \end{cases} \qquad k_{\beta_2} = \frac{\omega}{\beta_2},$ where α_2 and β_2 represent P-wave and S-wave velocities in the elastic reference medium, respectively. The derivation of this Green's function in the PS space is in Appendix E.

If the measurement surface is horizontal, $\hat{n} = (0, -1)$ for the situation shown in Figure 4.3, while $\hat{n} = (0, +1)$ for the situation in Figure 4.4. 4.2 is altered to be

$$
\begin{aligned}
&\int_{m.s.} \Big(\boldsymbol{\Phi}(\vec{r}', \vec{r}_s, \omega) \cdot \partial_{z'} \hat{\boldsymbol{G}}_0(\vec{r}', \vec{r}, \omega) - \partial_{z'} \boldsymbol{\Phi}(\vec{r}', \vec{r}_s, \omega) \cdot \hat{\boldsymbol{G}}_0(\vec{r}', \vec{r}, \omega) \Big) \cdot \hat{n} dx' \\
&= \begin{cases} -\boldsymbol{\Phi}_0(\vec{r}, \vec{r}_s, \omega) & \vec{r} \text{ below the M.S.} \\ \boldsymbol{\Phi}_s(\vec{r}, \vec{r}_s, \omega) & \vec{r} \text{ above the M.S.} \end{cases}
\end{aligned}
\tag{4.4}
$$

Using the reciprocity of the Green's function and Fourier transforming over x in Equation

4.4 with $\int e^{-ik_x x}dx$, the formulas in the wavenumber-frequency (k_x, ω) domain are

$$
\begin{aligned}
&\left[\tilde{\mathbf{\Phi}}(k_x, z', \vec{r}_s, \omega) \cdot \partial_{z'} \tilde{\hat{\boldsymbol{G}}}_0^T(k_x, z, z', \omega) - \partial_{z'} \tilde{\mathbf{\Phi}}(k_x, z', \vec{r}_s, \omega) \cdot \tilde{\hat{\boldsymbol{G}}}_0^T(k_x, z, z', \omega)\right] |_{z'=\epsilon_g} \\
&= \begin{cases} -\tilde{\mathbf{\Phi}}_0(k_x, z, \vec{r}_s, \omega) & z \geq \epsilon_g^+, \\ \tilde{\mathbf{\Phi}}_s(k_x, z, \vec{r}_s, \omega) & z \leq \epsilon_g^-. \end{cases}
\end{aligned}
\tag{4.5}
$$

Tildes represent the terms in the k_x domain, $\tilde{\hat{\boldsymbol{G}}}_0^T$ is the transpose of $\tilde{\hat{\boldsymbol{G}}}_0$, and ϵ_g is the depth of the receiver cable. z' is evaluated at ϵ_g.

By applying the algorithm in the (k_x, ω) domain, we can arrange to locate the output point $\vec{r}$ on the measurement surface at depth of ϵ_g to separate the actual measured data into the reference wave and the scattered wave. We can obtain the reference wave of the measured data by choosing $\vec{r}$ on the measurement surface to be part of the volume below the measurement surface; or, we can obtain the scattered wave of the measured data by choosing $\vec{r}$ on the measurement surface to be part of the volume above the measurement surface. The detailed explanation can be found in Weglein et al. (2013).

Green's theorem can also be applied to deghost the reflection data, or up-down separate the reflection data. If the properties along the measurement surface are assumed to be homogeneous and known, the reference medium can be chosen as a whole space of homogeneous elastic earth(Figure 4.5), whose properties are consistent with the actual along the measurement surface. There are two sources acting on the selected reference medium (Figure 4.6). S_1 is the air perturbation, representing the difference between the air (highlighted in gray) and the reference earth (highlighted in orange) above the air/earth surface. S_2 is the earth perturbation, standing for the difference between the actual earth (highlighted in purple) and the reference earth below the measurement surface.

4.3.3 Deghosting the scattered wave in the PS Space

Choosing a closed surface S' (highlighted by dark green in Figure 4.6) lower bounded by the measurement surface, and evaluating (or outputting) the Green's theorem based surface integral at any point inside the volume, the contribution due to source outside the volume (it is S_2) to the total reflection data at that point can be predicted. With a causal Green's function, source S_2 generates the upgoing wave at any point inside volume. If the evaluation point (e.g., at $\vec{r}$ as marked with a red dot in Figure 4.6) is below the air/earth boundary and above the measurement surface, the contributions from S_1 is downgoing at $\vec{r}$. Hence, the surface integral from Green's theorem indeed up-down separates the total scattered wavefield at point $\vec{r}$.

The elastic Green's-theorem deghosting formula in the space-frequency domain is

$$\mathbf{\Phi}_{up}(\vec{r}, \vec{r}_s, \omega) = \oint_{m.s.} \left(\mathbf{\Phi}_s(\vec{r}\,', \vec{r}_s, \omega) \cdot \nabla' \hat{\boldsymbol{G}}_0(\vec{r}\,', \vec{r}, \omega) - \nabla' \mathbf{\Phi}_s(\vec{r}\,', \vec{r}_s, \omega) \cdot \hat{\boldsymbol{G}}_0(\vec{r}\,', \vec{r}, \omega) \right) \cdot \hat{n} d\vec{r}\,', \tag{4.6}$$

where $\mathbf{\Phi}_{up} = \begin{pmatrix} \phi_{up}^P \\ \phi_{up}^S \end{pmatrix}$ is the predicted upgoing wave, and $\hat{\boldsymbol{G}}_0(\vec{r}\,', \vec{r}, \omega)$ is Green's function of the reference medium that is composed by a homogeneous whole-space of elastic earth. It has the analytic form of

$$\hat{\boldsymbol{G}}_0(\vec{r}\,', \vec{r}, \omega) = \begin{pmatrix} \hat{G}_0^P(\vec{r}\,', \vec{r}, \omega) & 0 \\ 0 & \hat{G}_0^S(\vec{r}\,', \vec{r}, \omega) \end{pmatrix} = \frac{1}{2\pi} \int dk_x e^{ik_x(x'-x)} \begin{pmatrix} \frac{e^{i\nu_2|z'-z|}}{2i\nu_2} & 0 \\ 0 & \frac{e^{i\eta_2|z'-z|}}{2i\eta_2} \end{pmatrix}. \tag{4.7}$$

Similarly, we can Fourier transform Equation 4.6 to the (k_x, ω) domain if the measurement surface is horizontal and flat.

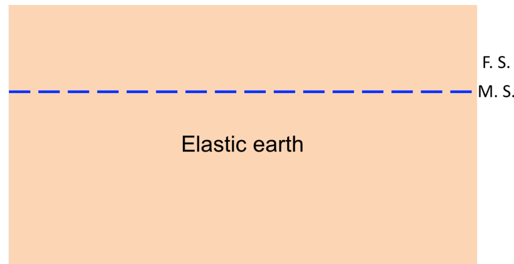

Fig. 4.5: A homogeneous elastic whole space as reference medium for deghosting.

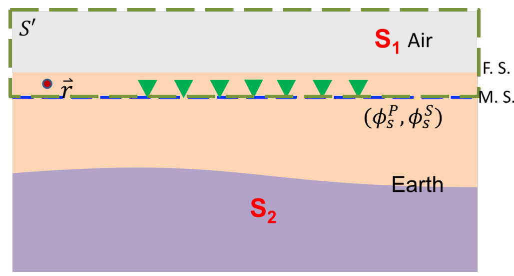

Fig. 4.6: Illustration of deghosting with a surface integral along S'; $\vec{r}$ is the evaluation (output) point above M.S..

4.4 *Numerical evaluation*

The methods that we develop in this chapter for separating the reference wave and the scattered wave, and for deghosting, we can test on an air/elastic-earth model. As is shown in Figure 4.7, the model consists of a half-space of air and a half-space of a two-layered elastic earth, the parameters of which are listed in Table 4.1. A P source is employed on the air/earth surface. The receivers are 5m below the free surface and they record both P- and S-waves. The output point $\vec{r}$ is on the measurement surface and the formulas in the (k_x, ω) domain is applied.

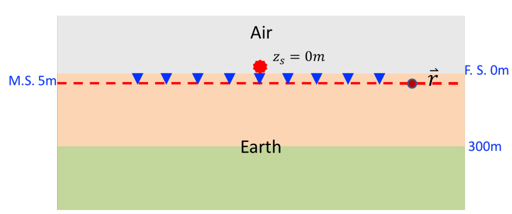

Fig. 4.7: The air/elastic-model for the numerical tests.

Layer Number	P-Velocity (m/s)	S-Velocity (m/s)	Density (kg/m^3)
1	340	0	3
2	2000	1200	1500
3	4000	3000	1800

Tab. 4.1: Parameters of the air/elastic-earth model used in Figure 4.7.

4.4.1 Numerical test for the separation of reference and scattered waves

The data for the total wavefield in the PS space (Figure 4.8(a) for ϕ^P and Figure 4.8(d) for ϕ^S) are created with the convolution of Ricker wavelet and the analytic forms of Green's function. Ground roll, as a type of the reference waves, dominates the energy of the total wavefield. We input the data to Equation 4.5 for the separation of reference waves and scattered waves. Since the output point $\vec{r}$ is on the measurement surface, we can predict the reference waves (Figure 4.8(b) for ϕ_0^P and Figure 4.8(e) for ϕ_0^S) of actual measured data by choosing $\vec{r}$ to be part of volume below, and we can similarly predict the scattered waves (Figure 4.8(c) for ϕ_s^P and Figure 4.8(f) for ϕ_s^S) of the actual measured data by choosing $\vec{r}$ to be part of the volume above the measurement surface. All the images are plotted in the same scales. Comparing the separated reference waves from the Green's theorem wave separation algorithm with that of the input data, both their amplitudes and phases match well. The same conclusion applies to the prediction results of scattered waves.

4.4.2 Numerical test for deghosting

The scattered waves (Figure 4.9(a) for ϕ_s^P and Figure 4.9(d) for ϕ_s^S) can be further separated into upgoing and downgoing waves. We apply the deghosting algorithm in the wavenumber domain so as to predict the upgoing wave of the actual measured reflection data (Figure 4.9(b) for the predicted upgoing P wave ϕ_{up}^P and Figure 4.9(e) for the predicted upgoing S wave ϕ_{up}^S), by choosing the output point $\vec{r}$ on the measurement surface to be part of the volume above. To evaluate the accuracy of the separation results, we analytically generate

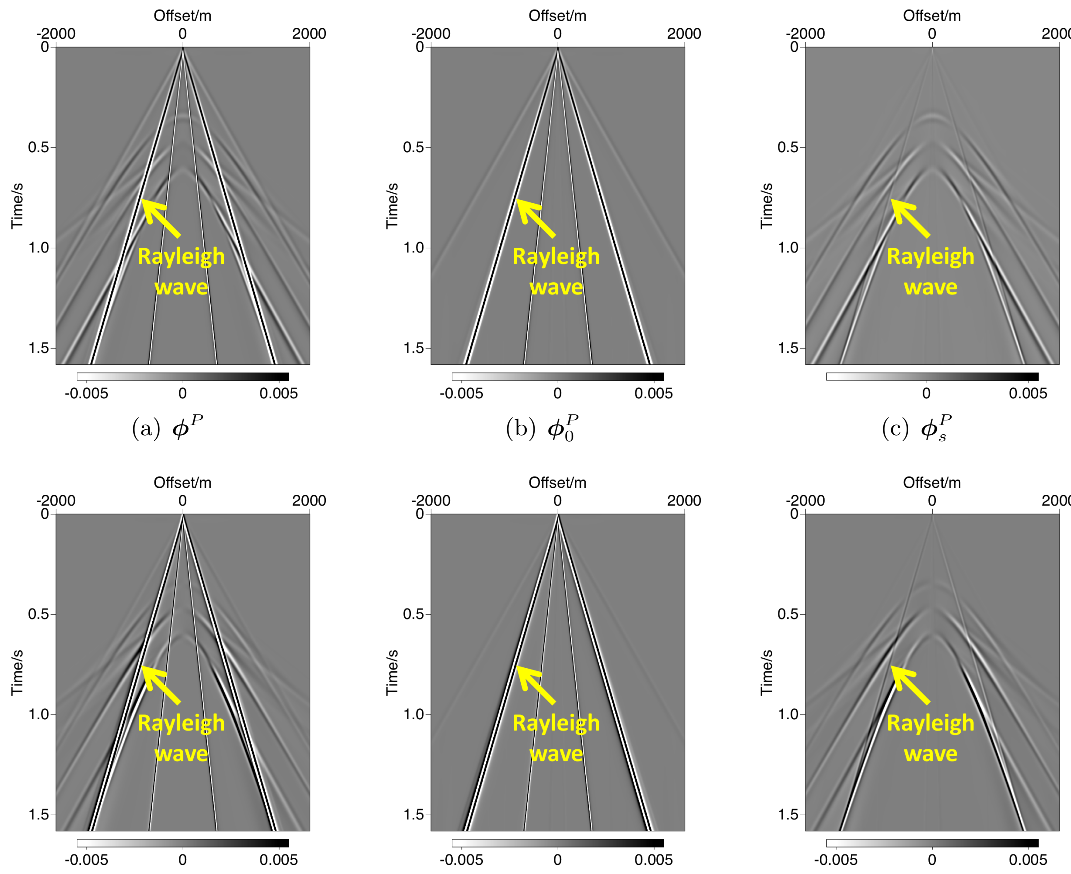

(a) $\boldsymbol{\phi}^P$ (b) $\boldsymbol{\phi}_0^P$ (c) $\boldsymbol{\phi}_s^P$

(d) $\boldsymbol{\phi}^S$ (e) $\boldsymbol{\phi}_0^S$ (f) $\boldsymbol{\phi}_s^S$

Fig. 4.8: Reference and scattered wave separation results. (a) P component total waves; (b) predicted P component reference waves, by choosing $\vec{r}$ to be part of volume below; (c) predicted P component scattered waves, by choosing $\vec{r}$ to be part of the volume above; (d) S component total waves; (e) predicted S component reference waves; and (f) predicted S component scattered waves. The color bars represent the amplitude (unit of N/m^2) of wavefield.

data that include the upgoing waves only (Figure 4.9(c) for synthetic ϕ_{up}^P and Figure 4.9(f) for synthetic Φ_{up}^S). The synthetic data can be treated as the ground truth results. Comparing Figure 4.9(b) with Figure 4.9(c) for the P components, and comparing Figure 4.9(e) with Figure 4.9(f) for the S components, the upgoing waves have been effectively predicted without distortion.

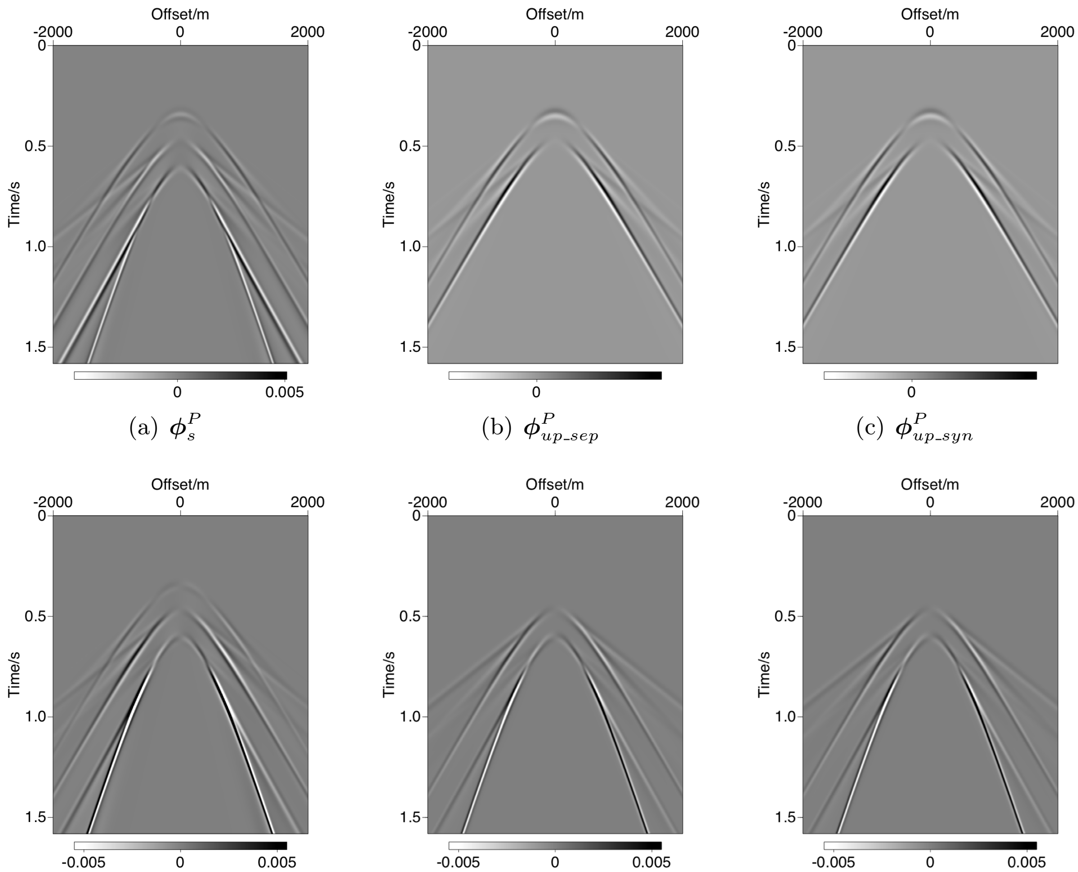

(a) ϕ_s^P (b) $\phi_{up\_sep}^P$ (c) $\phi_{up\_syn}^P$

(d) ϕ_s^S (e) $\phi_{up\_sep}^S$ (f) $\phi_{up\_syn}^S$

Fig. 4.9: Deghosting results. (a) P component input scattered waves; (b) predicted P component upgoing waves, by choosing $\vec{r}$ to be part of the volume above; (c) synthetic P component upgoing waves; (d) S component input scattered waves; (e) predicted S component upgoing waves; and (f) synthetic S component upgoing waves. The color bars represent the amplitude (unit of N/m^2) of wavefield.

4.5 Conclusion

We apply the elastic Green's theorem method to separate the reference waves and the scattered waves and to remove the ghosts from reflection data. For onshore experiments, this method has the potential to (1) remove the ground roll, which is a major portion of the reference waves and is a challenging issue for land data processing, and (2) to remove the ghosts from the reflection data. Neither damages the reflection data.

5. ONSHORE PREPROCESSING IN THE DISPLACEMENT SPACE: GROUND ROLL REMOVAL AND DEGHOSTING

5.1 Introduction

This chapter derives a method to tackle the land data in the displacement space. By choosing a homogeneous elastic whole space as the reference medium, a single application of the algorithm can separate both the surface waves and the receiver-side ghosts out from the acquired land data. The source is assumed in the form of a force (e.g., the Vibroseis truck can generate the force energy) at ground surface; therefore, there are no source-side ghosts existing in the data. The promise of the method is exemplified with two experiments, one using the buried receivers and the other using the on-surface receivers. It turns out that only the upgoing reflection component is predicted for both cases, and there is no injury on the upgoing reflection data. We develop this method to obtain seismic data without the contamination by either ground roll or ghosts, in preparation for the subsequent onshore processing and interpretation.

5.2 Theory

5.2.1 Description of a generic earth model

In this chapter, we take a 2D case as an example to explain the fundamental theory of Green's theorem based wave separation method and its application. 2D stands for a 2D earth (the property varies along both x- and z- directions, but not y-direction) and a 2D line source. Note that the theory is not limited to a 2D assumption, it can be extended to a more complicated 3D experiment.

As is shown in Figure 5.1, the generic onshore model consists of an air half space and an elastic earth half space. Receivers highlighted by green triangles are plugged into the earth. The measurement surface (the location of receivers) can be close to the air/earth surface as in the case of on-surface-receiver acquisition; it can also be of several meters below the air/earth surface for a buried-receiver survey. For either situation, the receivers are coupled with the elastic medium. The geophones record the particles' vibration in their vicinity area and transfer it to be a signal of the multicomponent displacement (u_x, u_z). The source in form of a force vector can be expressed as (f_x, f_z) (e.g., the vibroseis). It impinges on the air/earth boundary. In this case, there is no source-side ghost.

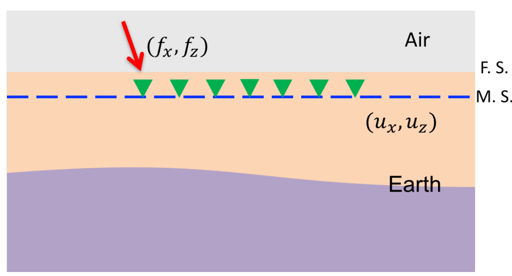

Fig. 5.1: A schematic of onshore experiment. Red arrow for a force vector; Green triangles for receivers; F. S. for air/earth boundary; M.S. for the measurement surface and marked with a blue dashed line.

For a 2D elastic isotropic medium, the wave equation is

$$\nabla \cdot \boldsymbol{\tau}(\vec{r}, \omega) + \rho\omega^2 \vec{u}(\vec{r}, \omega) = \vec{f}(\vec{r}, \omega), \tag{5.1}$$

where

$$\boldsymbol{\tau} = \lambda \nabla \cdot \vec{u} \boldsymbol{I} + \mu \left(\nabla \vec{u} + \vec{u} \nabla \right). \tag{5.2}$$

$\vec{u} = \begin{pmatrix} u_x \\ u_z \end{pmatrix}$ is the displacement, the 2^{nd}-order tensor $\boldsymbol{\tau} = \begin{pmatrix} \tau_{xx} & \tau_{xz} \\ \tau_{zx} & \tau_{zz} \end{pmatrix}$ is the stress, $\vec{f} = \begin{pmatrix} f_x \\ f_z \end{pmatrix}$ is a volume source, λ and μ are the Lamé's parameters of the earth, ρ is the density of the earth, and ω is the temporal frequency.

In this chapter, we assume that the portion of the earth in the vicinity of the measurement surface is homogeneous and known. Within that assumption, we choose the reference medium to be a homogeneous elastic whole space, as shown in Figure 5.2, whose properties agree with those of the actual earth along the measurement surface.

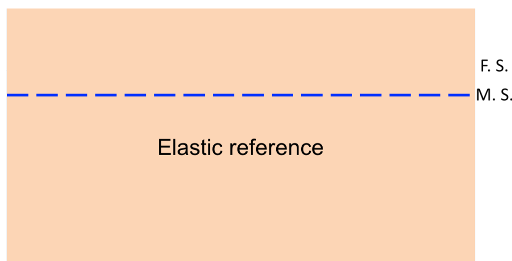

Fig. 5.2: A homogeneous whole-space of reference medium, with property consisting with the actual earth along the M.S..

The corresponding impulse response of the reference medium can be expressed as

$$\nabla \cdot \boldsymbol{\Sigma}_0(\vec{r}, \vec{r}\,', \omega) + \rho_0 \omega^2 \boldsymbol{G}_0(\vec{r}, \vec{r}\,', \omega) = \delta(\vec{r} - \vec{r}\,')\, \boldsymbol{I}, \tag{5.3}$$

where,

$$\Sigma_{0ijk} = \lambda_0 \partial_m G_{0mk} \delta_{ij} + \mu_0 (\partial_i G_{0jk} + \partial_j G_{0ik}), \qquad i, j, k = x, z. \tag{5.4}$$

$\boldsymbol{G}_0 = \begin{pmatrix} G_{0xx} & G_{0xz} \\ G_{0zx} & G_{0zz} \end{pmatrix}$ is the 2^{nd}-order Green's displacement tensor, $\boldsymbol{\Sigma}_0$ is the 3^{rd}-order Green's stress tensor, and the source term (as shown at the right side of Equation 5.3) consists of a diagonal matrix as $\boldsymbol{I}$ is an unit dyadic.

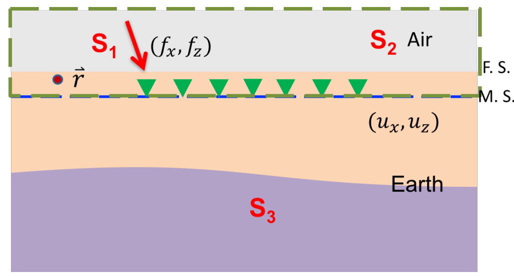

Fig. 5.3: The integral along the dashed Green line extracts the contributions from source S_3 for evaluation point $\vec{r}$ inside the volume.

5.2.2 Wave separation algorithm in space-frequency domain

Choosing a homogeneous reference as described in the last section, there are three sources (S_1, S_2 and S_3) acting on it. As can be seen from Figure 5.3, S_1 is the external force, called energy source; S_2 is the air perturbation that stands for the difference between the air (highlighted in gray) and the reference earth (highlighted in orange) above the air/earth boundary; S_3 is the earth perturbation that represents the difference between the actual earth (highlighted in purple) and the reference earth (highlighted in orange) below the measurement surface.

Under this specific definition of the actual onshore experiment, we choose a closed semi-infinite surface (highlighted by dark green in Figure 5.3) bounded below by the measurement surface, and evaluate (or output) the Green's theorem based surface integral at any point (e.g., at $\vec{r}$ as marked with a red dot in Figure 5.3) inside the volume. Then at that point, the contribution due to source outside the volume (it is S_3) to the total field can be predicted (The reason why Green's theorem derived integral algorithm can achieve wavefield separation is explained in Appendix C). With a causal Green's function to the reference medium, source S_3 generates the upgoing wave at a point inside volume. If the evaluation point $\vec{r}$ is below the air/earth boundary and above the measurement surface, the contributions from both S_1 and S_2 are downgoing, including the direct wave, the receiver-side ghosts, and ground roll. Therefore, S_3 actually produces the total/only upgoing portion of wavefield at point $\vec{r}$; i.e., the surface integral from Green's theorem can up-down separate the total wavefied at point $\vec{r}$. Eventually, we can predict the wavefield at $\vec{r}$ and that is with both ground roll and receiver-ghost removed.

Starting from Equation 5.1 and Equation 5.3, and using Green's theorem, we can derive the wave separation algorithm (check Appendix C for detail); that is, we can extract the upgoing waves generated by S_3.

In the space-frequency domain, the formula is

$$\vec{u}^{up}(\vec{r},\omega) = -\int_{m.s.} [(\hat{n}\cdot\boldsymbol{\tau}(\vec{r}\,',\omega)\cdot\boldsymbol{G}_0(\vec{r}\,',\vec{r},\omega) - \vec{u}(\vec{r}\,',\omega)\cdot(\hat{n}\cdot\boldsymbol{\Sigma}_0(\vec{r}\,',\vec{r},\omega))]d\vec{r}\,', \tag{5.5}$$

where $\vec{r}\,'$ is a receiver point at the measurement surface (abbreviated to m.s.), $\vec{r}$ is the evaluation/output point, $\hat{n}$ is the normal unit outside vector along the measurement surface, $\cdot$ represents a tensor product; and particularly,

$$\boldsymbol{\tau}(\vec{r}\,',\omega) = \lambda_0\nabla'\cdot\vec{u}(\vec{r}\,',\omega)\,\boldsymbol{I} + \mu_0(\nabla'\vec{u}(\vec{r}\,',\omega) + \vec{u}(\vec{r}\,',\omega)\nabla'). \tag{5.6}$$

Actually, $\vec{t} = \hat{n}\cdot\boldsymbol{\tau}$ is known as the traction along the measurement surface. In order to compute stress $\boldsymbol{\tau}$ or $\vec{t}$, there are two informations required: (1) the local property of earth in the vicinity of the measurement surface which is used to define the reference medium as well and, (2) the derivatives of multicomponent displacement along different directions, which is studied in Chapter 6. As a complete and direct examination of the algorithm provided in this chapter, we assume both requirements are satisfied in the subsequent initial synthetic examples.

The integral (Equation 5.5) performs along the measurement surface (the lower boundary of the closed surface) only. Since the closed surface is semi-infinite, the contribution from other three boundaries is zero by invoking the Sommerfeld radiation condition (Sommerfeld, 1949). By applying this equation, we can remove ground roll, the direct wave, and the receiver-side ghosts simultaneously. There is no assumption about the shape of the measurement surface, and it can be flat, inclined or uneven.

5.2.3 Wave separation algorithm in wavenumber-frequency domain

If the measurement surface is horizontal and flat, then $\hat{n} = (0,1)$. Equation 5.5 can be Fourier transformed into the (k_x, ω) domain. Considering $\hat{n} = (0,1)$, Equation 5.5 can be expanded explicitly as

$$\begin{aligned} u_x^{up}(\vec{r},\omega) = &- \int_{m.s.} [\tau_{zx}(\vec{r}\,',\omega)G_{0xx}(\vec{r}\,',\vec{r},\omega) + \tau_{zz}(\vec{r}\,',\omega)G_{0zx}(\vec{r}\,',\vec{r},\omega) \\ &- u_x(\vec{r}\,',\omega)\Sigma_{0zxx}(\vec{r}\,',\vec{r},\omega) - u_z(\vec{r}\,',\omega)\Sigma_{0zzx}(\vec{r}\,',\vec{r},\omega)]dx', \\ u_z^{up}(\vec{r},\omega) = &- \int_{m.s.} [\tau_{zx}(\vec{r}\,',\omega)G_{0xz}(\vec{r}\,',\vec{r},\omega) + \tau_{zz}(\vec{r}\,',\omega)G_{0zz}(\vec{r}\,',\vec{r},\omega) \\ &- u_x(\vec{r}\,',\omega)\Sigma_{0zxz}(\vec{r}\,',\vec{r},\omega) - u_z(\vec{r}\,',\omega)\Sigma_{0zzz}(\vec{r}\,',\vec{r},\omega)]dx'. \end{aligned} \tag{5.7}$$

With reciprocity,

$$\begin{aligned} &G_{0ij}(\vec{r}\,',\vec{r},\omega) = G_{0ji}(\vec{r},\vec{r}\,',\omega), \\ &\Sigma_{0ijk}(\vec{r}\,',\vec{r},\omega) = \lambda_0 \partial_{i'} G_{0ki}(\vec{r},\vec{r}\,',\omega)\delta_{ij} + \mu_0(\partial_{i'} G_{0kj}(\vec{r},\vec{r}\,',\omega) + \partial_{j'} G_{0ki}(\vec{r},\vec{r}\,',\omega)), \\ &i,j,k = x,z. \end{aligned} \tag{5.8}$$

Fourier transforming over x to Equation 5.7 with $\int e^{-ik_x x}dx$, we will have

$$\begin{aligned} \tilde{u}_x^{up}(k_x,z,\omega) = &- [\tilde{\tau}_{zx}(k_x,z',\omega)\tilde{G}_{0xx}(k_x,z,z',\omega) + \tilde{\tau}_{zz}(k_x,z',\omega)\tilde{G}_{0xz}(k_x,z,z',\omega) \\ &- \tilde{u}_x(k_x,z',\omega)\tilde{\Sigma}_{0zxx}(k_x,z',z,\omega) - \tilde{u}_z(k_x,z',\omega)\tilde{\Sigma}_{0zzx}(k_x,z',z,\omega)]|_{z'=\epsilon_g}, \\ \tilde{u}_z^{up}(k_x,z,\omega) = &- [\tilde{\tau}_{zx}(k_x,z',\omega)\tilde{G}_{0zx}(k_x,z,z',\omega) + \tilde{\tau}_{zz}(k_x,z',\omega)\tilde{G}_{0zz}(k_x,z,z',\omega) \\ &- \tilde{u}_x(k_x,z',\omega)\tilde{\Sigma}_{0zxz}(k_x,z',z,\omega) - \tilde{u}_z(k_x,z',\omega)\tilde{\Sigma}_{0zzz}(k_x,z',z,\omega)]|_{z'=\epsilon_g}, \end{aligned} \tag{5.9}$$

where $'\tilde{\ }'$ represents the term in the k_x domain, and z' is evaluated at the receiver's depth

ϵ_g. Specifically,

$$
\begin{aligned}
\tilde{\Sigma}_{0zxx}(k_x, z', z, \omega) &= \mu_0[\partial_{z'}\tilde{G}_{0xx}(k_x, z, z', \omega) - ik_x\tilde{G}_{0xz}(k_x, z, z', \omega)], \\
\tilde{\Sigma}_{0zzx}(k_x, z', z, \omega) &= \gamma_0\partial_{z'}\tilde{G}_{0xz}(k_x, z, z', \omega) - \lambda_0(ik_x)\tilde{G}_{0xx}(k_x, z, z', \omega), \\
\tilde{\Sigma}_{0zxz}(k_x, z', z, \omega) &= \mu_0[\partial_{z'}\tilde{G}_{0zx}(k_x, z, z', \omega) - ik_x\tilde{G}_{0zz}(k_x, z', z, \omega)], \\
\tilde{\Sigma}_{0zzz}(k_x, z', z, \omega) &= \gamma_0\partial_{z'}\tilde{G}_{0zz}(k_x, z, z', \omega) - \lambda_0(ik_x)\tilde{G}_{0zx}(k_x, z, z', \omega),
\end{aligned}
\tag{5.10}
$$

where γ_0 is the bulk modulus, and $\gamma_0 = \lambda_0 + 2\mu_0$.

For a homogeneous elastic whole space, both the Green's displacement tensor and its stress tensor can be expressed analytically in the (k_x, ω) domain (e.g., see Appendix G for $\boldsymbol{G}_0$).

By applying the algorithm in the (k_x, ω) domain, we can locate the output point $\vec{r}$ on the measurement surface and can arrange for it to become part of the volume above the measurement surface. Then, we are able to extract the upgoing wavefield that is exact a portion of the actual measured data. In the next section, we will numerically evaluate the method by applying algorithm in the (k_x, ω) domain, and locate the output point right on the measurement surface.

5.3 Numerical evaluation

We test the (k_x, ω) domain wave separation algorithm on a buried receiver experiment (as is seen in Figure 5.4) and an on-surface receiver experiment (as is seen in Figure 5.8), respectively. For both experiments, a vertical force $(0, F_z)$ is applied on the air/earth boundary, and both the multicomponent displacement and multicomponent traction are available at the receiver points as input. The models include one air layer and two elastic layers. The properties of different layers are listed in Table 5.1. The only difference between these two tests comes from the depths of the receivers. For the simplicity and convenience of comparison, the reflection events consist of the primaries and their ghosts only, but not the multiples and their corresponding ghosts; hence the up waves are actually the primaries in the two examples.

Layer Number	P-Velocity (m/s)	S-Velocity (m/s)	Density (kg/m^3)
1	340	0	3
2	1800	1200	1500
3	4000	2500	1800

Tab. 5.1: The parameters of the earth model used in Figure 5.4 and Figure 5.8.

5.3.1 Buried-receiver experiment

For the buried receiver survey, the measurement surface is at depth of 100m. Both the displacement and the corresponding traction are generated by multiplying their analytic Green's functions with a Ricker wavelet. As can be seen in Figure 5.5, the input displacement data consist of Rayleigh wave, direct wave, up reflection (primaries) and receiver-side ghosts. Due to a relatively deep measurement depth (100m below the free surface), the surface wave has already been attenuated and its energy is comparable to the reflection data. Besides, the three primary events as pointed by black arrows from top to bottom are with the propagation histories of $\grave{P}\acute{P}$, $\grave{P}\acute{S}/\grave{S}\acute{P}$, and $\grave{S}\acute{S}$ in the elastic layer.

All those multicomponent data ($\vec{u}(u_x, u_z), \vec{t}(t_x, t_z)$) are substituted into Green's theorem wave separation formula in (k_x, ω) domain as described in Equation 5.9. The output point $\vec{r}$ is arranged to be on the measurement surface, at depth 100m, and it is arranged as part of the volume above that surface. Finally, we can predict the upgoing waves of x and z components (see Figure 5.6(a) and Figure 5.7(a)). To evaluate the accuracy of the results, we analytically generate the data consisting of only the up waves, with the model of Figure 5.4. These data will serve as criteria for the examination of prediction results. The comparison between (1) the x component of predicted upgoing waves from the Green's theorem wave separation algorithm (Figure 5.6(a)) and (2) the x component of upgoing waves created with its analytic form (Figure 5.6(b)) shows that both their amplitudes and phases match well. Comparison of z components (see Figure 5.7(a) and Figure 5.7(b)) has a same conclusion to that of x component. As the results shown in Figure 5.6 and Figure 5.7 show, all the unexpected events (including Rayleigh waves, direct waves, and ghosts) are extinguished, and meanwhile the upgoing reflection data are not distorted.

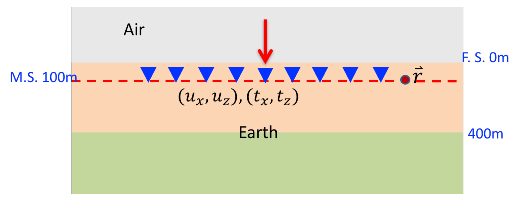

Fig. 5.4: A two-layer elastic earth model with buried receivers at 100 m below the free surface.

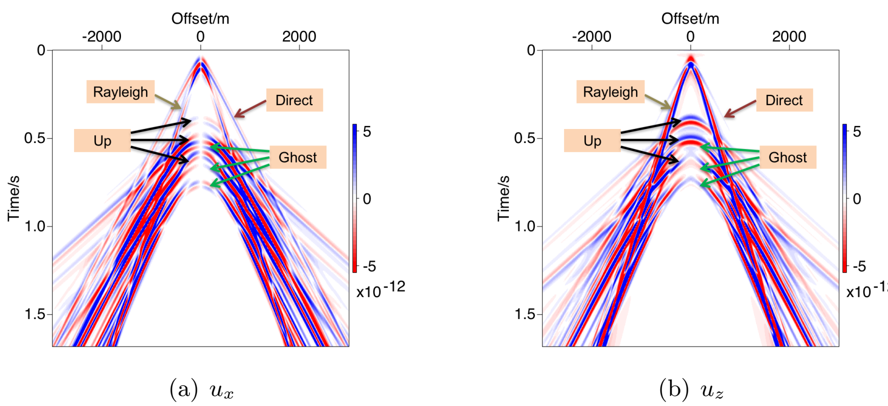

Fig. 5.5: Input total waves for buried receiver experiment. (a) for x component total wave; (b) for z component total wave. The color bars represent the amplitude (unit of m) of wavefield.

5.3.2 *On-surface-receiver measurement*

For the on-surface receiver experiment, the measurement surface is at depth of 0m. Similar to the previous example, both the displacement and the corresponding traction are generated by multiplying their analytic Green's functions with a Ricker wavelet, as plotted in Figure 5.9. But unlike the previous one, the measurement surface is infinitely close to the free surface; thus, the displacement data display a strong Rayleigh wave and a relatively weak reflection. In addition, the ghosts are interfering with the upgoing waves; and what's

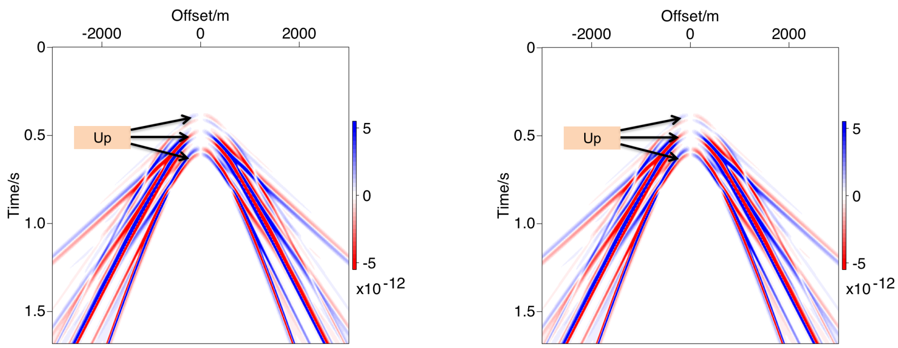

(a) $u^{up}_{x_{cal}}$ (b) $u^{up}_{x_{syn}}$

Fig. 5.6: X component wave separation results for buried receiver experiment. (a) the separated x component up wave; (b) the analytic synthetic x component up wave. The color bars represent the amplitude (unit of m) of wavefield.

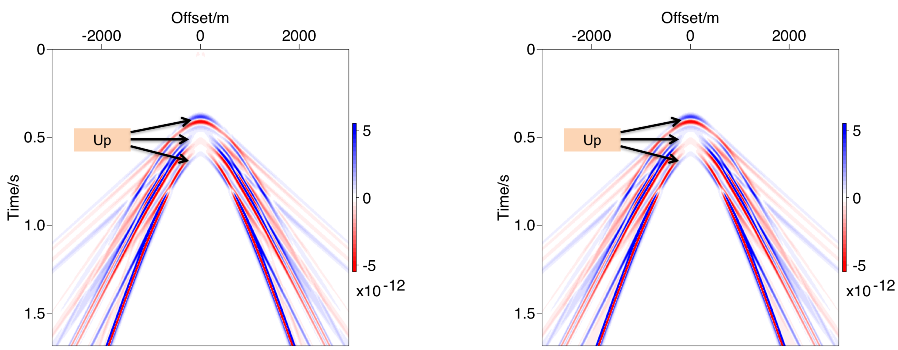

(a) $u^{up}_{z_{cal}}$ (b) $u^{up}_{z_{syn}}$

Fig. 5.7: Z component wave separation results for buried receiver experiment. (a) the separated z component up wave; (b) the analytic synthetic z component up wave. The color bars represent the amplitude (unit of m) of wavefield.

more, they interfere/overlap with each other at all offsets.

After applying the wave separation algorithm of Equation 5.9, we can predict the upgoing waves with both x (Figure 5.10(a)) and z components (Figure 5.11(a)). Comparing the separated up going waves with those from analytic generation (Figure 5.10(b) and Figure 5.11(b)), Green's theorem wave separation method shows its capability to effectively remove both the ground roll and the ghosts, and retain the up reflection data without damage.

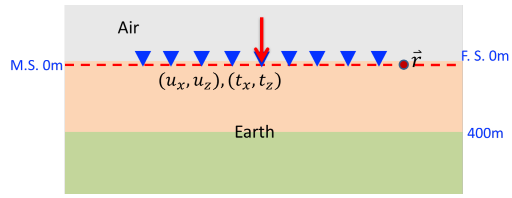

Fig. 5.8: A two-layer elastic earth model with on-surface receivers.

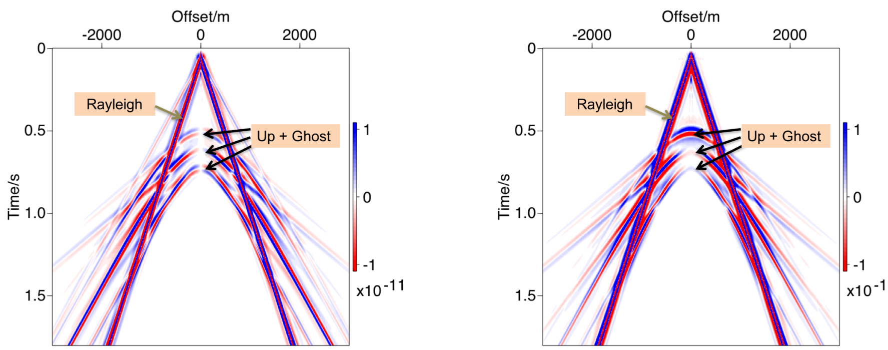

(a) u_x

(b) u_z

Fig. 5.9: Input total waves for on-surface receiver experiment. (a) x component total wave; (b) z component total wave. The color bars represent the amplitude (unit of m) of wavefield.

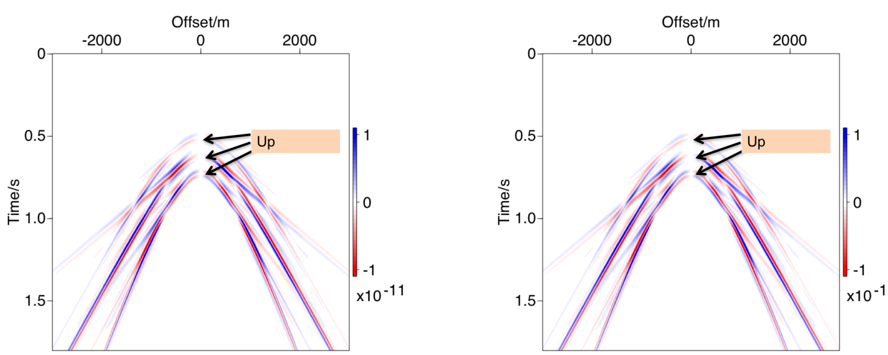

(a) $u^{up}_{x_{cal}}$

(b) $u^{up}_{x_{syn}}$

Fig. 5.10: X component wave separation results for on-surface receiver experiment. (a) the separated x component up wave; (b) the analytic synthetic x component up wave. The color bars represent the amplitude (unit of m) of wavefield.

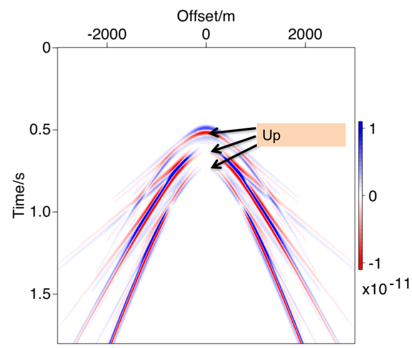

(a) $u^{up}_{z_{cal}}$

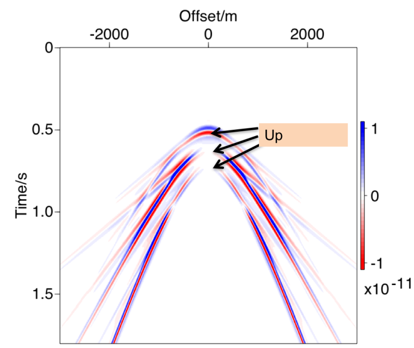

(b) $u^{up}_{z_{syn}}$

Fig. 5.11: Z component wave separation results for buried receiver experiment. (a) the separated z component up wave; (b) the analytic synthetic z component up wave. The color bars represent the amplitude (unit of m) of wavefield.

5.4 Conclusion

From the theoretical derivation and numerical tests, the elastic Green's theorem based wave separation method in the displacement space has ability to remove both the ground roll and the ghosts from land data. In addition, by choosing a homogeneous elastic whole space as the reference medium, we can remove these two types of waves simultaneously. The algorithm has two requirements: (1) both the displacement and the traction (or the directional derivative of displacement) should occur along the measurement surface, and (2) the properties along the measurement surface should be known. We are interest in reducing the demands of onshore data collection and the requirement of knowing near surface properties. Recently, we have developed a new simplified algorithm (Wu and Weglein, 2016a) to reduce the requirement of traction, which will be discussed in Chapter 6. In addition, an initial study (Appendix B) indicates that Green's theorem wave separation can separate a portion of wavefield caused by the near surface perturbation without knowing the near surface property. This property could benefit the ground roll removal without providing the information about the near surface. A further investigation will be made in the future.

6. ONSHORE PREPROCESSING FOR REFERENCE WAVE (INCLUDING GROUND ROLL) REMOVAL AND DEGHOSTING, AND ACHIEVING THAT OBJECTIVE WITH A REDUCED DATA REQUIREMENT

6.1 Introduction

As described and exemplified in Chapter 5, by applying the algorithm in the displacement space with an appropriate Green's function, both ground roll and the receiver-side ghosts can be separated out from the upgoing reflection data with satisfaction. However, the algorithm demands the multicomponent traction and the multicomponent displacement as input, in which the traction is not directly available in general. Traction can be computed via the constitutive (stress-strain) relationship only if the derivatives of each component of displacement wavefield are provided, assuming the earth property in the vicinity of the acquisition surface is known as well. This requirement restricts the practical application of this method, owing to the fact that the current leading-edge onshore acquisition can only record the multicomponent displacement at one depth. There are research experiments that perform receiver lines at two depths onshore for time lapse application or CO_2 monitoring (Bakulin et al., 2012; Neut et al., 2013); however, those two-depth-buried-receiver acquisitions have not been widely developed yet at the present stage.

In this chapter, we focus on the study to reduce the requirement of traction or the requirement of the derivatives of the displacement wavefield (traction is in a form of derivatives of displacement). Actually, this issue has started attracting researchers' attention since the

1990s, when the Green's theorem based wave separation method aimed to process marine data in priority. Yet the algorithm asked not only pressure measurement but also the normal derivative of pressure, which was an obstacle towards the application. There were a series of literature discussing data requirement (the requirement of normal derivate of pressure) reduction (Osen et al., 1998; Tan, 1999) and those works achieved significant accomplishments for marine exploration. The study in this chapter respecting to the land case is new. We develop a method to get rid of the reliance on traction. The original formula can be modified to call for the approximate source wavelet information rather than traction at all the receiver points along the acquisition surface, by assuming: (1) the medium to be composed of a half space of vacuum over a half space of earth, (2) the external force acting on the ground surface is local, and (3) the acquisition is right beneath the vacuum/earth boundary (i.e., the receivers are infinitesimally close to the vacuum/earth boundary from the earth side). The new and simplified algorithm has a significantly reduced data requirement, which is obtainable from current onshore leading-edge acquisition capability.

We begin with a short review of the research related to the marine experiment, which is in analogy with the issue that is encountered on the land application and in fact facilitate the understanding of study in this chapter. Afterward, a brief description of the data requirement of the original Green's theorem onshore preprocessing methodology is shown. Next, we concentrate in deriving the simplified algorithm by adopting a few approximations. And in the subsequent section, a numerical test is conducted to examine the usefulness of the vacuum/earth approximation and the new algorithm. The input data to the simplified algorithm are generated from a half space of air over a half space of elastic earth, but the new method processes the data as though they were from a vacuum/earth boundary. The outcome is a promising result that majority energy of ground roll and the ghosts is removed, and meanwhile, the upgoing reflection data are retained without injury. It is encouraging that the current onshore acquisition is able to benefit from the Green's theorem based wave separation method with the approach proposed in this chapter; i.e., the ground roll can be removed without needing traction anymore.

6.2 Historic work in marine application

Green's theorem derived method employs a model of the world that consists of the reference medium and the sources. The choice of reference medium will determine what the sources have to be in order to arrange for the reference medium and the sources together to correspond to the actual medium and to the experiment. The freedom of choosing a convenient reference medium means Green's theorem offers a flexible framework for deriving various useful algorithms. As can be seen from Figure 6.1, one instance in marine experiment is that selecting a reference medium as composed by a half-space of air over a half-space of water is used for the reference wave P_0 (which consists of the direct wave P_0^d and its ghost P_0^{FS}) and scattered wave P_s separation (Weglein and Secrest, 1990). Picking a volume bounded by the measurement surface (abbreviated to M.S.) and a hemisphere extending to infinity (marked with green in Figure 6.1(c), then the reference wave at any point inside the volume can be predicted by adopting the Green's theorem along the closed surface S'. The algorithm is

$$P_0(\vec{r}, \vec{r}_s, \omega) = \int_{m.s.} [P(\vec{r}', \vec{r}_s, \omega)\nabla G_0^+(\vec{r}', \vec{r}, \omega) - G_0^+(\vec{r}', \vec{r}, \omega)\nabla P(\vec{r}', \vec{r}_s, \omega)] \cdot \hat{n} dS', \quad (6.1)$$

where $\vec{r}$ is the prediction point where the reference wave is achieved; $\vec{r}'$ is the integral variable along the measurement surface; $\vec{r}_s$ is the source point; $\hat{n}$ is the normal outside vector along the measurement surface; ω is the radial frequency; P and $\nabla P \cdot \hat{n} = P_n$ are the pressure field and its normal derivative along the measurement surface; G_0^+ is causal Green's function in the reference medium. The integral is carried out along the measurement surface only, that is because the contribution form the infinite hemisphere approaches zero, by invoking the Sommerfeld radiation condition (Sommerfeld, 1949).

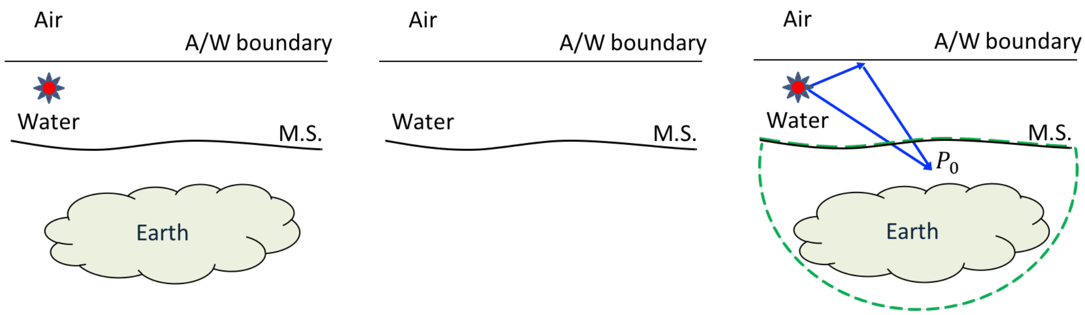

(a) (b) (c)

Fig. 6.1: A cartoon of marine experiment and wave separation. (a) for actual experiment; (b) for reference medium composed by an air half space over a water half space; (c) for reference-wave prediction. The red star for an airgun; A/W for air/water; M. S. for the measurement surface; the blue arrows for the predicted reference wave; the green dash line for the closed surface selected to apply Green's theorem.

Although theoretically elegant and rigorous, this algorithm was not easily practically utilized at that time due to the limited acquisition capability. The pressure measurement was deployed at a single depth, and that acquisition could not provide the normal derivative. With the important work done by Osen et al. (1998); Tan (1999), the requirement of P_n was reduced. The basic concept is that they imposed the Dirichlet boundary condition onto Green's function to make it vanish at the measurement surface. The detailed strategy and modification designed in order to estimate the wavelet can be found in those papers. Today the seismic acquisition technique has been advanced and P_n is obtainable; e.g., both the over-under cable (Moldoveanu et al., 2006) and the dual-sensor geo-streamer (Carlson et al., 2007) can effectively provide information of P_n.

However, there is an analogous requirement of spatial derivatives towards the onshore application. That requirement is in form of a traction, which is rarely provided currently and reducing the requirement of traction is the key point in the chapter. For completeness, the meaning of traction and its computation, and the way how wave separation theory calls for it inside the algorithm are to be discussed in detail at the beginning of the next section.

6.3 Theory

6.3.1 Data requirement of the complete onshore wave separation algorithm

Chapter 5 has explained in detail about the wave separation algorithm for data in the displacement space, which is able to separate out both ground roll and the receiver-side ghosts from the upgoing reflection data effectively. The corresponding algorithm (Equation 5.5) calls for both the multicomponent displacement and multicomponent traction. The current onshore acquisition can provide the knowledge of displacement but rarely the traction. Recalling the theoretical way to compute traction, it can explain the reason why the needing of traction is not easily met under current onshore survey status.

The concept of traction is used to analyze the internal forces acting mutually between adjacent particles within a continuum. Traction is a vector, being the force acting per unit area across an internal surface within the continuum, and quantifies the contact force (per unit area) with which particles on one side of the surface act upon particles on the other side (Aki and Richards, 2002).

Traction $\vec{t}$ can be computed using Hooke's law. Considering an isotropic elastic medium,

$$\vec{t} = \hat{n} \cdot \boldsymbol{\tau}, \tag{6.2}$$

and

$$\boldsymbol{\tau} = \lambda \nabla \cdot \vec{u} \boldsymbol{I} + \mu(\nabla \vec{u} + \vec{u} \nabla), \tag{6.3}$$

where $\hat{n}$ is the unit normal of the internal surface on which the traction acts; $\boldsymbol{\tau}$ is the stress tensor; λ and μ are Lamé's parameters of the elastic medium; and $\boldsymbol{I}$ is a unit dyadic.

This equation shows that in order to compute the traction along the measurement surface as input, the derivatives of each displacement component, the local property of earth in the vicinity of the measurement surface, and the shape of acquisition surface are required. We assume the property information along the measurement surface is known in this chapter and it is used as the reference medium. The shape of acquisition line is obtainable from acquisition geometry. The derivatives of displacement along different directions (e.g., the derivatives of u_x and u_z along both x direction and z direction in a 2D experiment) at a receiver point can be numerically approximated by finite difference method, which asks for the measurements of displacement at that receiver point itself and an extra receiver next to it. The neighboring geophones at a single depth can be used for the calculation of x direction. However, the measurement at two adjacent different depths is needed for the calculation of z direction, which is rarely what seismic acquisition performs today.

In summary, traction is not easily achievable either from the direct measurement or from the theoretical computation that requires derivatives of displacement.

6.3.2 Simplified algorithm for traction reduction

Similar to a marine case, reducing the requirement of traction (expressed in terms of the derivatives of displacement, and displacement is the typically measured wavefield) can enhance the value of elastic Green's theorem wave separation method from the practical point of view. Alternatively, instead of introducing Dirichlet boundary condition to the Green's function, we add several approximations/assumptions on the land experiment, which are:

1, A vacuum half-space is used to approximate the air half space, hence a vacuum/earth (V/E) boundary (as seen in Figure 6.2) replaces the actual air/earth boundary (as shown in Figure 5.1).

2, The external force acting on the vacuum/earth boundary is assumed to be concentrated at a point for simplicity, considering the size of a vibrator is much smaller in comparison with the whole exploration region. The force on the boundary (assuming the depth z equals to zero on the boundary) can be expressed as $\vec{f}(t)\delta(x - x_s)$, where $\vec{f}(t)$ is a time function representing the source wavelet, x_s is the source location, and the spatial delta function $\delta(x - x_s)$ states the local property of the source as a limiting case.

3, The receivers are right beneath the vacuum/earth boundary, corresponding to the conventional on-surface experiment. The depth of receivers approaches to zero from the earth side. As depicted in Figure 6.2, we push the measurement surface to be actually overlapping with the vacuum/earth boundary.

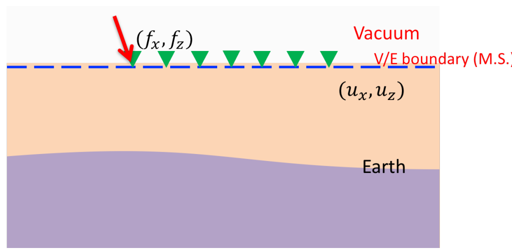

Fig. 6.2: An on-surface experiment with a vacuum/earth boundary approximation. V/E for vacuum/earth. Other symbols the same as those in Figure 5.1.

Taking these three approximations and applying the force boundary condition, we can have that along the measurement surface,

$$\vec{t}(x, z = 0, \omega) = -\vec{f}(\omega)\delta(x - x_s). \tag{6.4}$$

Substituted it into Equation 5.5, the wave separation formula is altered to be

$$\vec{u}^{up}(\vec{r}, \omega) = \vec{f}(\omega) \cdot \mathbf{G}_0(\vec{r}_s, \vec{r}, \omega) + \int_{m.s.} \vec{u}(\vec{r}', \omega) \cdot (\hat{n} \cdot \mathbf{\Sigma}_0(\vec{r}', \vec{r}, \omega))d\vec{r}', \tag{6.5}$$

The first integral in Equation 5.5 turns out to be a product between the source wavelet and the Green's function. The Green's function can be computed analytically. Instead of requiring traction at all the points along the measurement surface in the original algorithm (Equation 5.5), only the force information at the source point or an approximate wavelet information is needed in the new algorithm (Equation 6.5), which has an immediate data requirement reduction. The methods of estimating the external force or the source wavelet

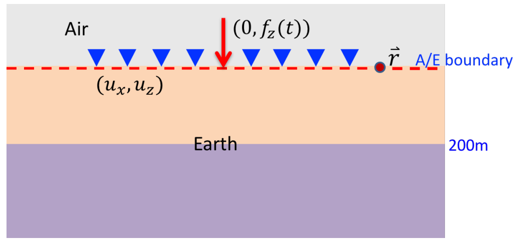

Fig. 6.3: A two-layer air/elastic-earth model for data generation. Symbols same as Figure 5.1.

have been developed and improved by many papers (e.g., Baeten and Ziolkowski (1990); Noorlandt and Drijkoningen (2016)).

The new and simplified algorithm derived in this section shows that under a vacuum/earth approximation, Green's theorem based wave separation method is practically applicable as long as a multicomponent displacement data and an estimated source wavelet are provided, which are available from current capability. So far, the objective of traction reduction is achieved by the new algorithm. It is natural to consider its performance on the wave separation, which is to be examined in the following section.

6.4 Numerical evaluation on an air/earth model

A numerical test is conducted now to evaluate the usefulness of the vacuum/earth approximation and the consequent new formula expressed in Equation 6.5. We generate the data using a model composed of a half space of air over a half space of elastic earth. Such model is more realistic to describe an exploration environment. The synthetic data are then substituted into Equation 6.5, with which the method can process the data as if they were from a vacuum/earth boundary. Given all that, if the computation result is still reasonable or even promising, a vacuum/earth boundary will be an effective approximation to the actual air/earth boundary and the new algorithm will be valuable in practice.

Figure 6.3 describes the specific air/earth model used for data simulation, with parameters shown in Table 6.1. The source as a vertical force vector is exerting on the air/earth

Layer Number	P-Velocity (m/s)	S-Velocity (m/s)	Density (kg/m^3)
1	340	0	3
2	700	400	600
3	1500	800	1000

Tab. 6.1: The parameters of the air/earth model in Figure 6.3.

boundary. That the vertical component can be expressed as a time function $f_z(t)$, which is assumed known or estimable and is used as an input of Equation 6.5. The receivers, measuring the displacement along both x and z directions, are right beneath the surface at a depth of 0m. Both f_z and $\vec{u}$ are substituted into Equation 6.5, which is derived with a vacuum/earth assumption.

The point $\vec{r}$ is an output location, which is arranged to be located at the measurement surface to be part of the volume above. In order to achieve that, one option is to implement the algorithm in the wavenumber-frequency (k_x, ω) domain (see, e.g., Weglein et al. (2013)), which assumes a horizontal measurement surface. The formula in space-frequency (x, ω) domain can accommodate a measurement surface with an arbitrary shape; however, the numerical consideration precludes the output point being too close to the acquisition surface and it cannot be on that surface. The measurement surface in this specific example is horizontal and meets the assumption to be able to carry out the algorithm in the wavenumber domain. We prefer to locate the output point on the actual measurement surface, that is because what to be predicted will be a portion of the input data if the algorithm can produce a satisfying result, in fact, it is convenient for the comparison between input and output data.

The shot record $\vec{u}$ is shown in Figure 6.4(a) for u_x and Figure 6.5(a) for u_z. To generate the data, we first use the corresponding impulse response in the (k_x, ω) domain, where the plane-wave reflections at horizontal reflectors can be achieved with analytical forms. Then an Inverse Fourier Transform is applied to transform the expression back to the space-time (x, t) domain. Finally, a shot record is obtained by convolving it with a source wavelet.

Since the receivers are right beneath the air/earth surface, the displacement profiles display particularly strong Rayleigh waves and relatively weak reflection waves (including primaries and their ghosts). In addition, the upgoing waves (or primaries) and their ghosts have the same traveling times; therefore, the interferences among the ghosts and the primaries exist at all offsets. The three primary events as pointed by black arrows from top to bottom are $\grave{P}\acute{P}$, $\grave{P}\acute{S}/\grave{S}\acute{P}$, and $\grave{S}\acute{S}$. We purposefully do not include multiples and their corresponding ghosts in the data, as it is convenient for analysis; however, the method doesn't have that limitation. The wave separation results from the new algorithm (by inputting both f_z and $\vec{u}$) are as shown in Figure 6.4(b) for x component displacement and Figure 6.5(b) for z component displacement. It is obvious that the Rayleigh waves are effectively reduced. In fact, if the new algorithm can provide accurate results, only the upgoing reflection data (or primaries) can exist in the wave separation results. Thereby, to further evaluate the effectiveness of the numerical results, the analytic primaries are plotted in Figure 6.4(c) for x component and Figure 6.5(c) for z component. The differences between the predicted primaries using the simplified algorithm and the ground truth primaries can be seen in Figure 6.4(d) for x component and Figure 6.5(d) for z component, which can be treated as errors produced by the new algorithm.

We can further understand the results by looking back to the approximations that have been made to the actual experiment for simplifying the original algorithm. We assume (1) a vacuum/earth model, (2) a local force that can be expressed by a spatial delta function, and (3) an on-surface measurement. The last two approximations agree with the actual experiment designed here. Therefore, the only approximation taken in the simplified algorithm for this example is a vacuum/earth boundary. In addition, if there is any difference between the final results from Equation 5.5 (without approximation) and from Equation 6.5 (with approximation), the difference can be caused by the difference between the first integral of Equation 5.5 and the product of Equation 6.5 only. We are about to analytically compare these two parts. It has been verified (Chapter 5) that the original algorithm

(Equation 5.5) can produce satisfying results. Hence, if the differences between those two parts are smaller, the new algorithm theoretically will be closer to accuracy.

With a vertical force as the excitation source, both the x component traction t_x of Equation 5.5 and the x component external force f_x of Equation 6.5 are zero. The first integral respecting to $\vec{t}$ in Equation 5.5 (it is under an air/earth assumption which is true) is

$$\begin{aligned}
& -\int_{m.s.} \vec{t}(\vec{r}', \omega) \cdot \mathbf{G}_0(\vec{r}', \vec{r}, \omega) d\vec{r}' \\
=& -\int_{m.s.} (0, t_z(\vec{r}', \omega)) \cdot \mathbf{G}_0(\vec{r}', \vec{r}, \omega) d\vec{r}' \\
=& -\int_{m.s.} (t_z(\vec{r}', \omega) G_{0zx}(\vec{r}', \vec{r}, \omega), t_z(\vec{r}', \omega) G_{0zz}(\vec{r}', \vec{r}, \omega)) d\vec{r}' \\
=& (0, -\int_{m.s.} t_z(\vec{r}', \omega) G_{0zz}(\vec{r}', \vec{r}, \omega) d\vec{r}'),
\end{aligned} \tag{6.6}$$

where the radiation pattern is used: in a homogeneous medium, $G_{0zx}(\vec{r}', \vec{r}, \omega) = 0$ for the same depth (0m in this experiment) of source point $\vec{r}$ and receiver point $\vec{r}$.

The product between the source wavelet and the Green's function in Equation 6.5 (it is with a vacuum/earth assumption which not accurate) is

$$\begin{aligned}
& \vec{f}(\omega) \cdot \mathbf{G}_0(\vec{r}_s, \vec{r}, \omega) \\
=& (0, f_z(\omega)) \cdot \mathbf{G}_0(\vec{r}_s, \vec{r}, \omega) \\
=& (f_z(\omega) * G_{zx}(\vec{r}_s, \vec{r}, \omega), f_z(\omega) * G_{zz}(\vec{r}_s, \vec{r}, \omega)) \\
=& (0, f_z(\omega) * G_{zz}(\vec{r}_s, \vec{r}, \omega)),
\end{aligned} \tag{6.7}$$

where the radiation pattern that $G_{zx}(\vec{r_s}, \vec{r}, \omega) = 0$ for $z_s = z = 0$ is also used.

Equation 6.6 and Equation 6.7 show that neither the first integral of Equation 5.5 nor the product of Equation 6.5 contributes to the x component result. The algorithm with an air/earth assumption is able to produce an accurate x component result, hence the same to the new algorithm in this chapter. It explains the negligible error, as plotted in

Figure 6.4(d), which has a scale that is 10^{-6} order smaller in comparison with the most accurate result in Figure 6.4(c).

Regarding the z component results, they are not equal between Equation 6.6 and Equation 6.7 because the vertical component of traction is not zero along the measurement surface in the actual experiment. However, the plot in Figure 6.5(d) shows that there is an only very small residual of Rayleigh wave, and the primaries are never damaged or distorted by the simplified algorithm. This conclusion can also be found from the plot in Figure 6.6, where three traces from Figure 6.5(a), 6.5(b), 6.5(c) at offset of 320 m, are isolated for comparison. The predicted primary (marked by a red dash line) from the new algorithm are almost overlapping with the accurate analytic primary (marked by a blue dash line). The purple circle is the difference between the prediction and accuracy, and the difference indicates a very small residual of Rayleigh waves.

The preliminary numerical test demonstrates the effectiveness of the simplified new algorithm. It is able to reduce both ground roll and ghosts from land data and preserve the up-going reflection data. The new algorithm is obtained with a vacuum/earth approximation, which mismatches the reality that the actual input data are generated from an air/earth boundary. Nevertheless, the result is reasonable and acceptable. What is more important is that the new algorithm doesn't depend on the multicomponent traction anymore.

6.5 Conclusion

The elastic Green's theorem based wave separation method has potential to remove both ground roll and ghosts for the onshore application. The original algorithm demands both the multicomponent displacement and the multicomponent traction, yet traction is not easily achieved from current acquisition ability. Consequently, in general, the acquisition today is hard to benefit from the original algorithm for ground roll removal. In this chapter, we develop a simplified new formula that requires the displacement but not the traction,

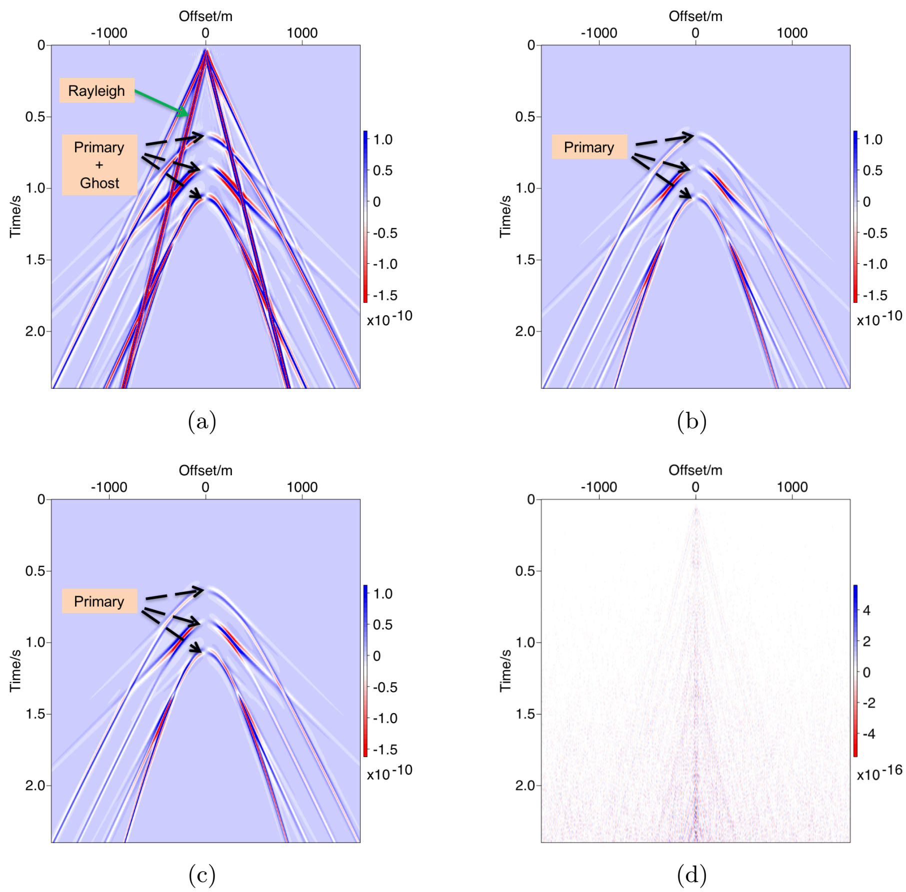

Fig. 6.4: X component wave separation result. (a) total wave; (b) separated upgoing wave from the new algorithm; (c) analytic upgoing wave; (d) the difference between (b) and (c). The color bars represent the amplitude (unit of m) of wavefield.

as long as the force information at the source point or an approximate source wavelet information can be provided or estimated. The new method assumes a vacuum/earth model and measurements are performed at a vacuum/earth surface. Although the new formula is derived under a vacuum/earth-model approximation, the preliminary synthetic test indicates that it is still valuable for an air/earth model. The air/earth boundary is not exactly satisfying the assumption but is closer to the realistic exploration situation. This chapter provides a potential and positive opportunity for the practical application of Green's theorem based wave separation method to facilitate onshore exploration.

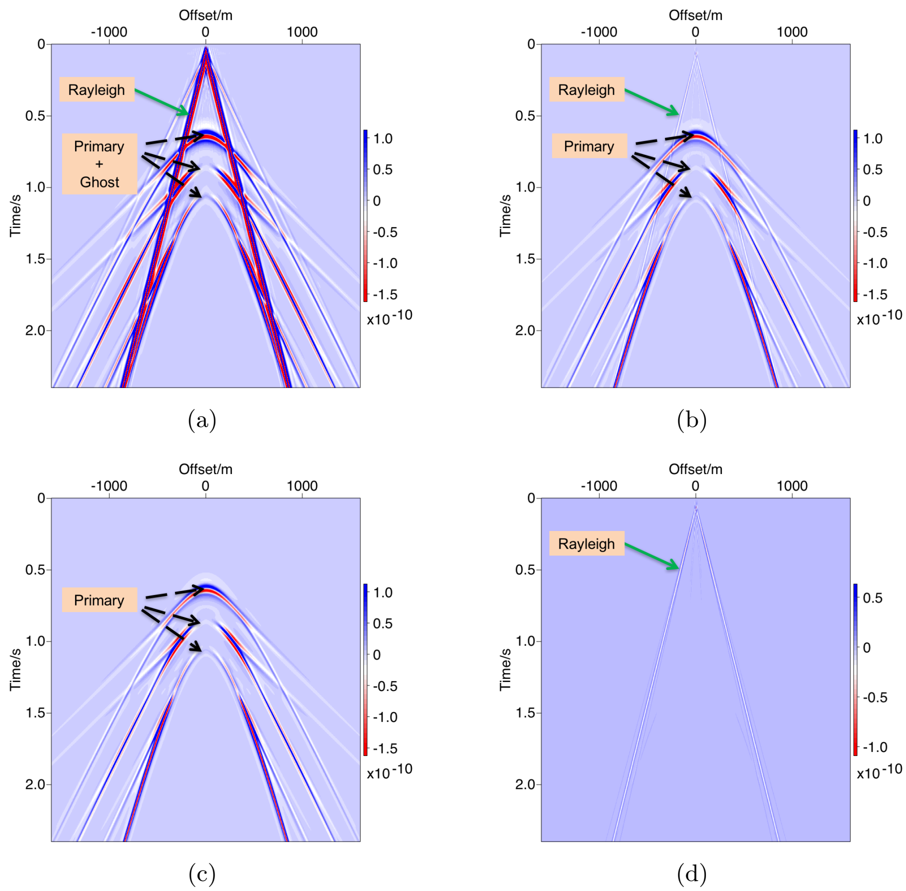

Fig. 6.5: Z component wave separation result. (a) total wave; (b) separated upgoing wave from the new algorithm; (c) analytic upgoing wave; (d) the difference between (b) and (c). The color bars represent the amplitude (unit of m) of wavefield.

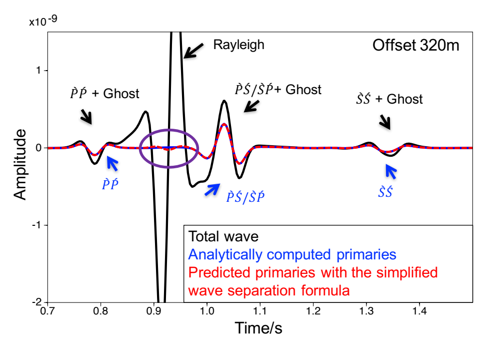

Fig. 6.6: A single-trace comparison at 320 m (Figure 6.5(a), (b), (c)). Black line is total wave; blue line is analytically computed primary; red line is predicted primary from Equation 6.5. Blue arrows point to events of data; the blue arrows point to primaries. Purple circle is the residual Rayleigh wave (or error) in the result. The unit of amplitude is m.

7. TESTING THE INVERSE SCATTERING SERIES INTERNAL MULTIPLE ATTENUATION ALGORITHM FOR AN INELASTIC EARTH WITHOUT ELASTIC OR INELASTIC SUBSURFACE PROPERTIES

7.1 Introduction

The inverse scattering series (ISS) can achieve all processing objectives directly by using distinct isolated task-specific sub-series and without subsurface information (Weglein et al., 2003). Besides, there is a general proof in Weglein et al. (2003) that for both the ISS free-surface multiple elimination algorithm and the ISS internal multiple (IM) attenuation algorithm, those corresponding sub-series not only do not care about the subsurface information, they do not care about the model type. The subsurface earth model can be acoustic, elastic, or inelastic, and those algorithms require no modifications; i.e., they are both model-type independent.

Previous synthetic data tests on this algorithm have involved multidimensional acoustic medium (e.g., Araújo, 1994; Weglein et al., 1997) and elastic medium (Coates and Weglein, 1996). Previous research demonstrates that selecting a homogeneous acoustic background, the ISS method can effectively predict the multiples of the data, which are generated from either acoustic earth or elastic earth.

However in practice, the earth material can be in many cases different from an ideal (acoustic/elastic) solid; e.g., anisotropic, porous, etc. The seismic waves propagating in such inelastic media will encounter energy loss (particularly the component of high frequency) and velocity dispersion. In this chapter, for the first time, the ISS internal multiple attenuator is tested on data from this type of medium. Specifically, although the actual world is absorptive and dispersive, the reference medium doesn't take that information but keeps to be homogeneous acoustic. We will demonstrate in this chapter that applying the industry-standard ISS internal multiple attenuator can attenuate the multiples. Two situations will be considered here, the 1D normal incidence plane wave (Wu and Weglein, 2014), and the 1D-earth, 3D-point-source pre-stack data. For both cases, we show analytic and numerical evaluations[1]. The results with an attenuating medium show that the method retains its value and promise to directly predict internal multiples with a correct time and an approximate amplitude, without knowing or estimating any elastic or inelastic subsurface properties.

7.2 ISS attenuator evaluation for data with Q: 1D normal incidence plane wave

7.2.1 Wavefield expression in the attenuating medium

For an absorptive-dispersive medium, the one-way Helmholtz wave equation in 1D medium can be written as

$$\frac{d^2P(x,\omega)}{dx^2} + \frac{\omega^2}{c^2(\omega)}P(x,\omega) = 0, \tag{7.1}$$

Assuming a constant Q (or frequency-independent Q) model (e.g. Kolsky, 1956; Kjartansson, 1979; Aki and Richards, 2002), and within a reasonable seismic bandwidth,

$$\frac{1}{c(\omega)} = \frac{1}{c_0}\left(1 + \frac{F(\omega)}{Q}\right). \tag{7.2}$$

[1] For concisenessthe numerical test on pre-stack data will be shown in the next chapter while discussing a new method to improve the prediction, and that result is treated as the one from the current method

where

$$F(\omega) = \frac{i}{2}sgn(\omega) - \frac{1}{\pi}log\left(|\frac{\omega}{\omega_r}|\right). \tag{7.3}$$

It is constitute of two terms: the first term is related to the energy attenuation, and the second term is related to velocity dispersion. ω_r here is the reference frequency, and it could be chosen as the maximum frequency or the central frequency in the experiment. c_0 is the velocity at the reference frequency.

Q here is used to represent the energy loss for a wave-field propagating, in one wave length, and is defined as (Aki and Richards, 2002)

$$Q = \frac{2\pi E}{\Delta E}, \tag{7.4}$$

where E is the energy of the wave-field, and ΔE is the energy loss in a wavelength of propagation. Solving Equation 7.1, the wavefield $P(x,\omega)$ can be expressed as

$$P(x,\omega) = e^{i\frac{\omega}{c(\omega)}x} = e^{i\frac{\omega}{c_0}x}e^{-\frac{\omega\,\mathrm{sgn}(\omega)}{2c_0Q}x}e^{-i\frac{\omega}{c_0\pi Q}\log(|\frac{\omega}{\omega_r}|)x}. \tag{7.5}$$

This formula tells that the wavefield is influenced by three terms: the first term corresponds to the phase with the velocity of c_0, the second term contributes to the energy attenuation, and the third term is for the phase delay with velocity dispersion. Only the first term will be left when Q increases to infinity; i.e., the medium is back to be elastic.

7.2.2 *Analytical test of the ISS attenuator with 1D normal incidence plane wave*

Following the explanation in the previous section, we can express the wavefield in an inelastic medium analytically. In this section, the inelastic data will be used as input to test the ISS internal multiple attenuation algorithm analytically.

For 1D normal incidence, the ISS internal multiple attenuation algorithm (e.g., Araújo, 1994; Weglein et al., 1997, 2003) can be expressed as:

$$b_3(k_z) = \int_{-\infty}^{\infty} b_1(z)e^{ik_z z}dz \int_{-\infty}^{z-\epsilon} b_1(z_1)e^{-ik_z z_1}dz_1 \int_{z_1+\epsilon}^{\infty} b_1(z_2)e^{ik_z z_2}dz_2, \tag{7.6}$$

where the deghosted data $D(t)$, for an incident spike wave, satisfy $D(\omega) = b_1(2\omega/c_0)$. $b_1(z) = \int_{-\infty}^{\infty} b_1(k_z)e^{-ik_z z}dk_z$, $k_z = 2\omega/c_0$ is the vertical wavenumber. $b_1(z)$ corresponds to an un-collapsed Stolt migration of the normal-incident spike plane-wave data. ϵ in the formula is used to ensure the events satisfy the lower-higher-lower relationship, and its value is chosen on the basis of wavelet length.

A two-reflector model is provided below as an example, with the parameters listed in Figure 7.1, and with the depths of source and receiver both assumed to be zero.

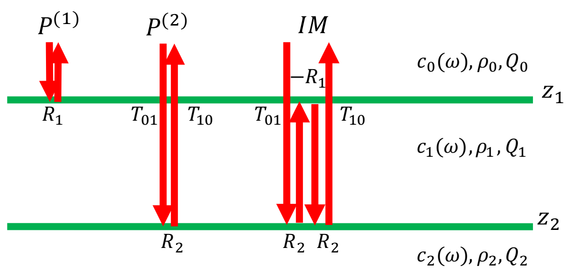

Fig. 7.1: A two-reflector 1D normal incidence model. $P^{(1)}$ and $P^{(2)}$ are primaries from the first and the second interface, respectively; IM is the first-order internal multiple; R_1 and R_2 are reflection coefficients; T_{01} and T_{10} are transmission coefficients. c_i is velocity; ρ_i is density; and Q_i is quality factor; i:0,1,2.

For a 1D model and a 1D normal-incident plane wave, two primaries in the data $D(\omega)$ can be represented as:

$$\begin{aligned} P^{(1)}(\omega) &= R_1(\omega)e^{i\frac{\omega}{c_0(\omega)}2z_1}, \\ P^{(2)}(\omega) &= T_{01}(\omega)T_{10}(\omega)R_2(\omega)e^{i\frac{\omega}{c_0(\omega)}2z_1}e^{i\frac{\omega}{c_1(\omega)}2(z_2-z_1)}, \end{aligned} \tag{7.7}$$

where $\frac{1}{c_i(\omega)} = \frac{1}{c_i}\left(1 + \frac{F(\omega)}{Q_i}\right)$, $i = 0, 1, 2$). All of these velocities are frequency dependent. Both primaries suffer from the absorption and dispersion.

After migrating the data into the pseudo depth domain to get $b_1(z)$, we can substitute it into Equation 7.6. We further assume that two primaries in $b_1(z)$ are isolated and ϵ is chosen reasonably to make sure there is no overlap between the two events among the integrals. The predicted internal multiple $b_3(k_z)$ can be obtained as:

$$b_3(k_z) = \left(T_{01}(k_z)T_{10}(k_z)R_2(k_z)\right)^2 R_1^*(k_z)e^{-\frac{|k_z|}{Q_0}z_1}e^{ik_z\left(1+\frac{F(k_z)}{Q_0}\right)z_1}e^{i2k_z\frac{c_0}{c_1}\left(1+\frac{F(k_z)}{Q_1}\right)(z_2-z_1)}, \tag{7.8}$$

where $F(k_z) = \frac{i}{2}sgn(k_z) - \frac{1}{\pi}\log(|\frac{k_z}{k_{z_r}}|)$, and $k_{z_r} = 2\omega_r/c_0$.

The actual first-order internal multiple in the k_z domain is

$$IM(k_z) = -T_{01}(k_z)T_{10}(k_z)\left(R_2(k_z)\right)^2 R_1(k_z)e^{ik_z\left(1+\frac{F(k_z)}{Q_0}\right)z_1}e^{i2k_z\frac{c_0}{c_1}\left(1+\frac{F(k_z)}{Q_1}\right)(z_2-z_1)}. \tag{7.9}$$

The relation between the predicted internal multiple and the actual internal multiple is

$$b_3(k_z) = -T_{01}(k_z)T_{10}(k_z)\frac{R_1^*(k_z)}{R_1(k_z)}e^{-\frac{|k_z|}{Q_0}z_1}IM(k_z). \tag{7.10}$$

If we define

$$\begin{aligned} TF &= -T_{01}(k_z)T_{10}(k_z)\frac{R_1^*(k_z)}{R_1(k_z)}, \\ QF &= e^{-\frac{|k_z|}{Q_0}z_1}, \end{aligned} \tag{7.11}$$

then

$$b_3(k_z) = TF * QF * IM(k_z). \tag{7.12}$$

TF is the transmission factor, and QF is the Q absorption factor. For this two-reflector model, TF represents the transmission loss at the first interface; whereas QF represents the transmission loss (energy absorption) in the first layer. However, if there are more than two reflectors existing in the absorptive media, both TF and QF will have more complicated forms.

If we use $IM^{(j)}$ to represent the multiple that is generated at the j^{th} interface (i.e., the down-reflection happens at the interface of depth z_j), and $j \geq 1$, then

$$
\begin{aligned}
TF &= \begin{cases} -T_{01}T_{10}\frac{R_1^*}{R_1} & j=1 \\ -\prod_{i=1}^{i=j-1}|T_{i-1,i}T_{i,i-1}|^2 T_{j-1,j}T_{j,j-1}\frac{R_j^*}{R_j} & j>1 \end{cases} \\
QF &= \begin{cases} e^{-\frac{|k_z|}{Q_0}z_1} & j=1 \\ e^{-\sum_{i=1}^{i=j-1}(\frac{|k_z|}{Q_i}\frac{c_0}{c_i}(z_{i+1}-z_i))}e^{-\frac{|k_z|}{Q_0}z_1} & j>1 \end{cases}
\end{aligned}
\tag{7.13}
$$

TF relates to the transmission loss at the interfaces that are above and on the multiple generator, and QF relates to the transmission loss in the layers above the multiple generator. Both TF and QF are smaller than 1; therefore, the prediction amplitude is smaller than actual.

From the analysis above, even though the data go through an absorptive and dispersive medium, doesn't have absorption/dispersion in the reference medium and the background is kept to be homogeneous acoustic (c_0). Given all that, the prediction has the accurate time and approximate amplitude. This is an example of the model-type-independence of the ISS internal multiple attenuation algorithm.

7.2.3 Numerical test of ISS attenuator with 1D normal incidence plane wave

Layer Number	Depth(m)	Velocity (m/s)	Density (kg/m^3)	Q
1	375	1500	1000	60
2	1250	2500	1000	40
3		6000	1000	60

Tab. 7.1: A two-reflector 1D model to generate normal incident plane wave.

A two-reflector 1D model (Table 7.1) is used as an example to numerically evaluate the effectiveness of ISS internal multiple attenuator on inelastic, normal-incident plane wave data. As a blue line shown in Figure 7.2(a), given small Q in each layer, all the primaries and internal multiples suffer seriously from the absorption, and the shapes are broadened at later time. The red line in Figure7.2(a) shows the predicted internal multiple. The specific comparison between the prediction and the actual internal multiple of the data are plotted in Figure 7.2(b). We confirm from this result that, even with significant energy attenuation and velocity dispersion, the ISS attenuator still predicts multiple with the accurate time and an approximate amplitude.

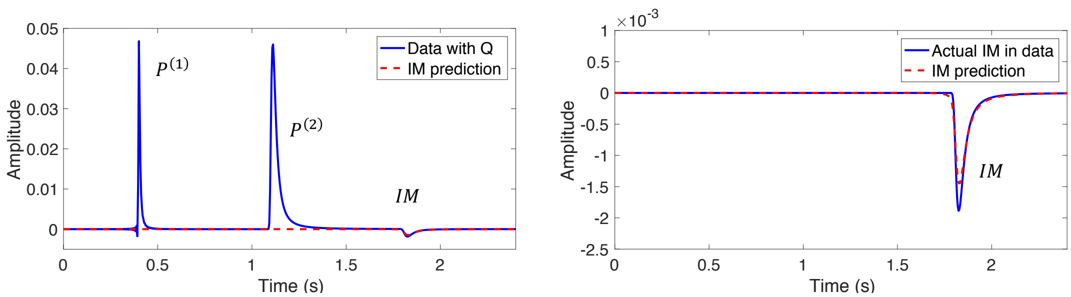

(a) (b)

Fig. 7.2: The numerical result of ISS attenuator with inelastic 1D normal incidence plane wave. (a) shows the input data b_1 (blue line) and the predicted multiple -b_3 (red line); (b) shows the actual internal multiple (blue line) and the predicted internal multiple -b_3 (red line). The unit of amplitude is N/m^2.

7.3 ISS attenuator evaluation for data with Q: 1D earth, 3D-point source pre-stack data

7.3.1 Wavefield expression in the attenuating medium with pre-stack data

7.3.1.1 Green's function

For an absorptive-dispersive medium, Green's function $G_0(\vec{r}, \vec{r}_s, \omega)$ satisfies wave equation that

$$\left(\nabla^2 + \frac{\omega^2}{c^2(\omega)}\right) G_0(\vec{r}, \vec{r}_s, \omega) = \delta(\mathbf{r} - \vec{r}_s), \tag{7.14}$$

where $\vec{r}$ is the receiver point, $\vec{r}_s$ is the source point. Assuming a constant Q model, and using the definition in Formula 7.2 and 7.3, we can solve Equation 7.14 to have

$$G_0(\vec{r}, \mathbf{r}_s, \omega) = \frac{1}{(2\pi)^2} \int_{-\infty}^{\infty} \int_{-\infty}^{\infty} \frac{e^{ik_z|z-z_s|}}{2ik_z} e^{ik_x(x-x_s)} e^{ik_y(y-y_s)} dk_x dk_y, \tag{7.15}$$

where the vertical wavenumber

$$\begin{aligned} k_z &= sgn(\omega)\sqrt{\frac{\omega^2}{c^2(\omega)} - k_x^2 - k_y^2} \\ &= sgn(\omega)\sqrt{\frac{\omega^2}{c_0^2} - k_x^2 - k_y^2 + \frac{\omega^2}{c_0^2}\frac{F(\omega)}{Q}} \\ &= sgn(\omega)\sqrt{q^2 + \frac{\omega^2}{c_0^2}\frac{F(\omega)}{Q}}. \end{aligned} \tag{7.16}$$

$q = sgn(\omega)\sqrt{\frac{\omega^2}{c_0^2} - k_x^2 - k_y^2}$. Green's function can be treated as a sum of weighted plane waves from all the directions. k_z is a complex value caused by $F(\omega)$.

7.3.1.2 *Pre-stack wavefield of a one-reflector 1D absorptive model*

Given a one-reflector 1D earth model as shown in Figure 7.3, and the depth of the interface is z_1, we can express the wavefield based on Equation 7.15. Besides, since the model is horizontally homogeneous, a 3D point source can generate the data with the cylindrical symmetry that cares the offset only. Hence, the original double Fourier transform in Equation 7.15 can be simplified as Hankel transform. Assuming both the source and receiver are located at the depth 0 (i.e., $\epsilon_s = \epsilon_g = 0$),

$$D(r, \omega) = \frac{1}{2\pi} \int_{-\infty}^{\infty} \frac{R_1(k_r, \omega) e^{i2k_z z_1}}{2ik_z} J_0(k_r r) k_r dk_r, \tag{7.17}$$

where $r = \sqrt{(x_g - x_s)^2 + (y_g - y_s)^2}$, k_r is the Fourier conjugate of r, J_0 is the first-kind 0^{th}-order Bessel function, and data in wavenumber domain can be transformed back to

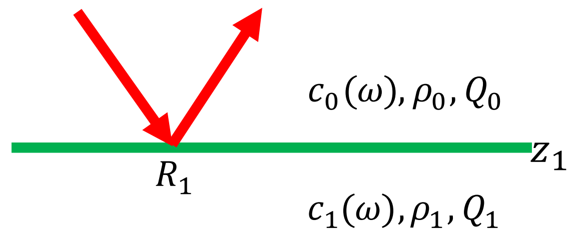

Fig. 7.3: A one-reflector horizontal model to generate pre-stack data.

space domain via Hankel transform.

$$D(k_r, \omega) = \frac{R_1(k_r, \omega) e^{i2k_z z_1}}{2ik_z}. \tag{7.18}$$

The reflection coefficient for plane wave is

$$R_1(k_r, \omega) = \frac{k_z - k_{z_1}}{k_z + k_{z_1}}, \tag{7.19}$$

where $k_z = sgn(\omega)\sqrt{\frac{\omega^2}{c_0^2} - k_r^2 + \frac{\omega^2}{c_0^2}\frac{F(\omega)}{Q_0}}$, and $k_{z_1} = sgn(\omega)\sqrt{\frac{\omega^2}{c_1^2} - k_r^2 + \frac{\omega^2}{c_1^2}\frac{F(\omega)}{Q_1}}$.

7.3.2 Analytic test of ISS attenuator with pre-stack data

In this section, the pre-stack data $D(r, t)$ from the absorptive-dispersive earth will be used to test the ISS internal multiple attenuator analytically. The algorithm of 3D point source and 1D earth is chosen for the analytic evaluation in this section and the subsequent numerical tests. Besides, we assume that the first layer where the source is located does not involve the absorption and dispersion; i.e., Q_0 in the first layer is infinity or $Q_0 \gg 0$.

For 3D source and 1D earth, the ISS internal multiple attenuation algorithm (Lin and Weglein, 2015) is

$$b_3(k_r, 2q) = \int_{-\infty}^{\infty} b_1(k_r, z) e^{i2qz} dz \int_{-\infty}^{z-\epsilon} b_1(k_r, z_1) e^{-i2qz_1} dz_1 \int_{z_1+\epsilon}^{\infty} b_1(k_r, z_2) e^{i2qz_2} dz_2, \tag{7.20}$$

where $q = sgn(\omega)\sqrt{\frac{\omega^2}{c_0^2} - k_r^2}$; and c_0 is the velocity of the first layer, at the reference frequency ω_r.

$b_1(k_r, \omega) = 2iqD(k_r, \omega)$. Since we assume that $Q_0 \gg 0$, the vertical wavenumber in the first layer $k_z = sgn(\omega)\sqrt{q^2 + \frac{\omega^2}{c_0^2}\frac{F(\omega)}{Q_0}} \approx q$, which is approximately a real value. Therefore, multiplying $D(k_r, \omega)$ with $2iq$, the denominator of $D(k_r, \omega)$ as shown in Equation 7.18 is approximately removed in $b_1(k_r, \omega)$. $b_1(k_r, z)$ is in the pseudo depth domain, after applying an un-collapsed migration. $b_3(k_r, 2q)$ is the predicted internal multiple.

Then, as shown in Figure 7.4, a two-reflector 1D earth model is taken as an example, with zero depths of both the source and the receiver.

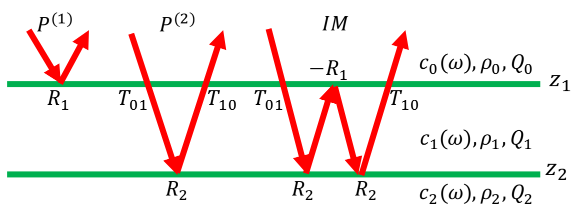

Fig. 7.4: A two-reflector 1D model to generate pre-stack data. Symbols same as Figure 7.1.

Two primaries can be expressed in (k_r, ω) domain with forms

$$\begin{aligned} P^{(1)}(k_r, \omega) &= R_1(k_r, \omega)e^{i2k_z z_1}, \\ P^{(2)}(k_r, \omega) &= T_{01}(k_r, \omega)T_{10}(k_r, \omega)R_2(k_r, \omega)e^{i2k_z z_1}e^{i2k_{z_1}(z_2 - z_1)}, \end{aligned} \tag{7.21}$$

where $k_{z_1} = sgn(\omega)\sqrt{q_1^2 + \frac{\omega^2}{c_1^2}\frac{F(\omega)}{Q_1}}$, and $k_r^2 + q_1^2 = \frac{\omega^2}{c_1^2}$. All the reflection and transmission coefficients are complex values.

$$b_1(k_r, \omega) = P^{(1)}(k_r, \omega) + P^{(2)}(k_r, \omega). \tag{7.22}$$

Changing the variable from ω to $2q$ ($q = sgn(\omega)\sqrt{\frac{\omega^2}{c_0^2} - k_r^2}$),

$$\begin{aligned}
b_1(k_r, 2q) &= P^{(1)}(k_r, 2q) + P^{(2)}(k_r, 2q), \\
P^{(1)}(k_r, 2q) &= R_1(k_r, q)e^{ik_z 2z_1}, \\
P^{(2)}(k_r, 2q) &= T_{01}(k_r, q)T_{10}(k_r, q)R_2(k_r, q)e^{ik_z 2z_1}e^{ik_{z_1}2(z_2 - z_1)},
\end{aligned} \tag{7.23}$$

where

$$\begin{aligned}
k_z &= sgn(q)\sqrt{(k_r^2 + q^2)(1 + \frac{F(k_r, q)}{Q_0}) - k_r^2}, \\
k_{z_1} &= sgn(q)\sqrt{(k_r^2 + q_1^2(q))(1 + \frac{F(k_r, q_1(q))}{Q_1}) - k_r^2}, \\
F(k_r, q) &= \frac{i}{2}sgn(q) - \frac{1}{\pi}log(\frac{\sqrt{(k_r^2 + q^2)}}{|\omega_r|}), \\
F(k_r, -q) &= F^*(k_r, q).
\end{aligned} \tag{7.24}$$

Similarly the internal multiple of the data can be expressed as

$$IM(k_r, 2q) = -T_{01}(k_r, q)T_{10}(k_r, q)R_1(k_r, q)R_2^2(k_r, q)e^{ik_z 2z_1}e^{ik_{z_1}4(z_2 - z_1)}. \tag{7.25}$$

Applying the un-collapse migration (or Fourier transforming b_1 from $2q$ to z),

$$b_1(k_r, z) = P^{(1)}(k_r, z) + P^{(2)}(k_r, z). \tag{7.26}$$

We substitute b_1 with two primaries into the internal multiple attenuation algorithm as shown in Equation 7.20. With the similar assumption used in the 1D normal incidence case, the predicted internal multiple $b_3(k_r, 2q)$ can be obtained finally.

$$\begin{aligned}
b_3(k_r, 2q) &= P^{(2)}(k_r, 2q)P^{(1)}(k_r, -2q)P^{(2)}(k_r, 2q) \\
&= (T_{01}(k_r, q)T_{10}(k_r, q))^2 R_1^*(k_r, q)R_2^2(k_r, q)e^{ik_z 2z_1}e^{ik_{z_1}4(z_2 - z_1)}e^{i(k_z - k_z^*)2z_1} \\
&= (T_{01}(k_r, q)T_{10}(k_r, q))^2 R_1^*(k_r, q)R_2^2(k_r, q)e^{ik_z 2z_1}e^{ik_{z_1}4(z_2 - z_1)}e^{-\mathrm{IMAG}(k_z)4z_1},
\end{aligned} \tag{7.27}$$

where IMAG(k_z) is the imaginary part of k_z.

Comparing the analytic forms between the predicted and the actual multiples, we find

$$b_3(k_r, 2q) = -T_{01}(k_r, q)T_{10}(k_r, q)\frac{R_1^*(k_r, q)}{R_1(k_r, q)}e^{-\text{IMAG}(k_z)4z_1}IM(k_r, 2q). \tag{7.28}$$

Similar to the normal incidence case, we define

$$\begin{aligned} TF &= T_{01}(k_r, q)T_{10}(k_r, q)\frac{R_1^*(k_r, q)}{R_1(k_r, q)}, \\ QF &= e^{-\text{IMAG}(k_z)4z_1}, \end{aligned} \tag{7.29}$$

then

$$b_3(k_r, 2q) = TF * QF * IM(k_r, 2q). \tag{7.30}$$

If there are more than two reflectors existing in the absorptive media, and we assume that the multiple that is generated at the j^{th} interface ($j \geq 1$), then

$$\begin{aligned} TF &= \begin{cases} -T_{01}T_{10}\frac{R_1^*}{R_1} & j = 1 \\ -\prod_{i=1}^{i=j-1}|T_{i-1,i}T_{i,i-1}|^2 T_{j-1,j}T_{j,j-1}\frac{R_j^*}{R_j} & j > 1 \end{cases} \\ QF &= \begin{cases} e^{-\text{IMAG}(kz)4z_1} \approx 1 & j = 1 \\ e^{-\sum_{i=1}^{i=j-1}(\text{IMAG}(kz_i)4(z_{i+1}-z_i))}e^{-\text{IMAG}(kz)4z_1} & j > 1 \end{cases} \end{aligned} \tag{7.31}$$

Again, both TF and QF are smaller than 1, and they will corporate to produce a smaller prediction amplitude; however, the time is exact. Actually, even the first layer is suffering from not slight absorption (e.g., for the model that will be tested in the following numeric section, $Q_0 = 100$), it still comes out a satisfying result.

We skip the numerical test but leave it until the next chapter. The same conclusion would be drawn from the pre-stack test: the current ISS attenuator can predict the exact time and approximate amplitude of the internal multiples without any subsurface information.

7.4 Discussion and conclusion

In this chapter, the ISS internal multiple attenuation algorithm is tested analytically and numerically using Q-influenced data, with the conclusion that the prediction will have the correct phase and an approximate amplitude.

This study gives us confidence that even for an attenuating medium, the ISS internal multiple attenuator can provide a result that retains the primary and partially removes the internal multiple. This is an important step in a strategy to eliminate internal multiples for both elastic and inelastic media. That will allow application for exploration plays where the geology exhibits significant absorption.

There are different approaches and ideas for internal multiple elimination in an anelastic medium. (1) developing an ISS eliminator for anelastic media directly; (2) preprocessing for Q compensation, and then applying the ISS elimination algorithm in the acoustic/elastic media (Zou and Weglein, 2013). In terms of Q compensation, it can be achieved by method either with Q information or without Q information (e.g., Innanen and Weglein, 2003, 2005; Innanen and Lira, 2010). Chapter 8 is a response of improving the prediction amplitude.

7.5 Acknowledgments

I thank Clement Kostov, Debra Dishberger and Schlumberger for providing an outstanding internship and mentoring opportunity.

8. A MODIFIED INVERSE SCATTERING INTERNAL MULTIPLE ATTENUATION ALGORITHM TO IMPROVE THE PREDICTION AMPLITUDE FOR REFLECTION DATA WITH Q ABSORPTION

[1] This chapter provides a new method to improve the prediction of internal multiple from an inelastic medium, where the propagating waves suffer energy attenuation and velocity dispersion. The current Inverse-Scattering-Series (ISS) internal multiple attenuation algorithm has a unique capability to predict the exact time and approximate and well-understood amplitude of all the internal multiplesof a given orderat once, and without assuming (or determining) any elastic or inelastic subsurface properties.For the first order ISS internal multiple attenuationalgorithm in an inelastic medium,there are two factors contributing to the amplitude difference between the predicted and the actual internal multiples: (a) the elastic transmission losses at interfaces above and at the reflector where the internal multiple has its downward reflection, and (2) an inelastic transmission loss due tothe energy absorption in the layers above thereflector where the first order multiple experiences its downward reflection. Note that if the medium is acoustic/elastic, only the first factor contributes to the amplitude prediction. Obviously the second factor contributes if the medium is absorptive and dispersive. That factor may lead to amplitude prediction is significantly smaller than the actual multiple. A modified attenuation method is proposed in this chapter to remove the second and improve the prediction amplitude for an absorptive-dispersive medium. The new methodis exemplified with a simple 1D model and

[1] Modified from 2014 Schlumberger internship report, co-authored with Clement Kostov at Schlumberger and Debra Dishberger previously at Schlumberger.

a complicated synthetic acoustic model, both considering absorption and dispersion. The initial results demonstrate the promise and potential effectiveness of the proposed approach, being able to deliver a more effective internal multiple prediction in an inelastic exploration region.

8.1 Introduction

Internal multiple removal is an important and longstanding problem in seismic exploration. The demand and interest for new and improved capability in removing multiples is driven by the portfolio of the petroleum industry and by current and anticipated future exploration trends (Weglein, 2015). Among all the well-developed de-multiple methods (e.g., stacking, deconvolution, Radon transform, and Feedback loop, etc.), the ISS method is stand alone for its ability to achieve internal multiple prediction without requiring any subsurface information and interpretive intervention (Araújo, 1994; Weglein et al., 1997, 2003).

Coates and Weglein (1996) have shown that the ISS attenuation algorithm can predict internal multiple with the exact time and the approximate amplitude for data from an acoustic/elastic earth which is away from Q absorption. The amplitude difference between the predicted multiple and the actual multiple is related to the transmission losses at the interfaces above and at the reflector that the downward reflection occurs (Weglein and Matson, 1998; Weglein et al., 2003). Zou and Weglein (2013, 2015) have developed an ISS elimination algorithm to remove that transmission loss factor and predict the exact amplitude of internal multiple in case of an acoustic medium.

For data from an inelastic medium, Wu and Weglein (2014) have demonstrated with analytic and numerical evaluations that the ISS attenuation method reaches the same conclusion as the acoustic/elastic case, and without any need or interest in knowing the absorptive/dispersive mechanism. However, in comparison with an acoustic/elastic situation, the prediction amplitude in an inelastic medium is even smaller than the actual multiple.

That is because in addition to the elastic transmission loss at the interfaces, the inelastic transmission loss (energy absorption) in the layers above the interfaces where the downward reflection happens can also cause the difference between the prediction and reality. If the absorptive property is significant above the major reflector where internal multiple has its downward reflection, the influence from the energy absorption will be dramatic to the amplitude inaccuracy, especially at high frequency.

In order to remove the inelastic influence (Q's effect) and improve the prediction amplitude, we alter the current ISS algorithm by purposefully injecting two datasets to its three integral terms: the outer two terms remain not changed with the original Q-attenuated data as input; the inner term takes data with amplitude compensation, using half the estimated Q value. In so doing, the over predicted energy-absorption factor from the current algorithm can be surgically eliminated from the new solution. The prediction amplitude gets closer to the actual, which can benefit an optimal adaptive subtraction and promotes an effective multiple removal ultimately. The new approach would provide value to the exploration areas where absorption is significant, e.g., pre-salt plays in deep water Gulf of Mexico, off-shore Brazil, and the North Sea.

8.2 The current ISS attenuation algorithm

We take a 1D normal-incidence plane wave as an example to explain the current method and its property, and the proposed advancement; however, the solution is extendable to pre-stack data from 1D or multi-D earth. The current ISS internal multiple attenuation algorithm for 1D normal-incident data (Araújo, 1994; Weglein et al., 1997) is

$$b_3(k_z) = \int_{-\infty}^{\infty} b_1(z)e^{ik_z z}dz \int_{-\infty}^{z-\epsilon} b_1(z_1)e^{-ik_z z_1}dz_1 \int_{z_1+\epsilon}^{\infty} b_1(z_2)e^{ik_z z_2}dz_2, \tag{8.1}$$

b_1 relates to data D. For a plane wave, $D(\omega) = b_1(k_z)$. $b_1(z) = \int_{-\infty}^{\infty} b_1(k_z)e^{-ik_z z}dk_z$. ω is temporal frequency, c_0 is water speed, and $k_z = \frac{2\omega}{c_0}$. A water-speed migration maps the data to pseudo-depth, in form of $b_1(z)$. ϵ ensures that the events selected by the three integrals satisfy a deeper-shallower-deeper relationship in pseudo-depth domain; and ϵ's value is determined based on the wavelength of the wavelet. $b_3(k_z)$ is the predicted multiple.

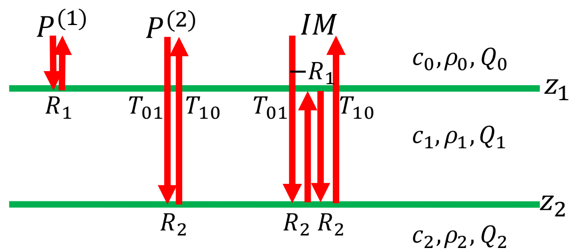

Fig. 8.1: A two-reflector 1D normal-incidence model. $P^{(1)}$ and $P^{(2)}$, primaries; IM, the first-order internal multiple; R_1 and R_2, reflection coefficients; T_{01} and T_{10}, transmission coefficients. c_i, the velocity at central frequency; ρ_i, density; and Q_i, quality factor; i:0,1,2.

As is shown in Figure 8.1, for a two-reflector absorptive model, whose source and receiver depths are both assumed to be zero. Substituting the analytic data into Equation 8.1, the predicted multiple is also analytic (refer to Wu and Weglein (2014)). Comparing the prediction $b_3(k_z)$ with the actual multiple IM,

$$b_3(k_z) = -T_{01}T_{10}\frac{R_1^*}{R_1}e^{-\frac{|k_z|}{Q_0}z_1}IM(k_z) \tag{8.2}$$

* denotes the conjugate. The term highlighted with blue relates to the elastic transmission loss at the first interface, and the one in red relates to the inelastic transmission loss (or, energy absorption) in the first layer. Defining the blue one as the Transmission Factor (TF), and the red one as the Q Absorption Factor (QF),

$$\frac{b_3(k_z)}{IM(k_z)} = TF * QF. \tag{8.3}$$

Both TF and QF are less than one, meaning that the amplitude ratio between the predicted and the actual recorded multiple is also less than one. This yields predicted models with weaker amplitude response than the field multiples. Further, if there are more than two reflectors in the absorptive media, and an internal multiple downward reflects at a deeper interface, both and will have more complicated forms. There is a global transmission loss, starting from the top and down to the reflector that multiple experiences its downward reflection, over-estimated by the current algorithm, Equation 8.1.

A well-log model is employed to calculate the transmission loss upon frequency and the multiple generator. The larger the number of the multiple generator, the deeper the depth where downward reflection happens. A constant Q value is utilized for this analysis. Figure 8.2(a) indicates that the amplitude ratio ($TF*QF$) decreases as frequency increases and the multiple generator gets deeper. On the other hand, if TF is isolated (Figure 8.2(b)), the frequency dependency will disappear, and the value will be obviously amplified at high frequency and deep multiple generator in comparison with $TF * QF$. Therefore, removing QF can increase the amplitude ratio between the prediction and the actual recorded multiple, and essentially improve the prediction amplitude. Similarly, removing TF would also be important for enhancing the prediction amplitudes. Notice that the simple method for estimating TF in Figure 8.2(b) over-estimates the transmission losses as it does not take into account short-period internal multiples (O'Doherty and Anstey, 1971).

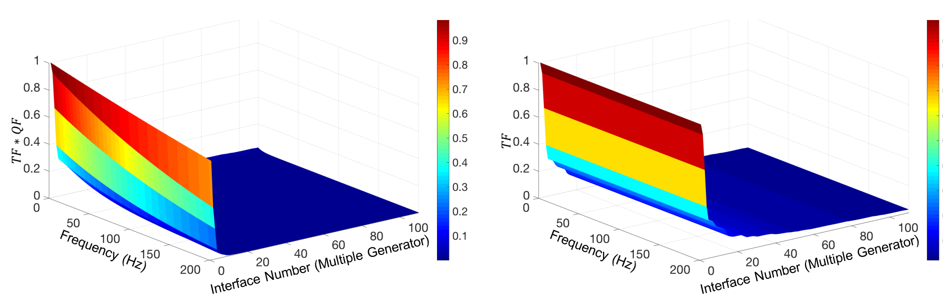

(a) (b)

Fig. 8.2: Transmission losses due to ISS method with a well-log data. (a) $TF * QF$; (b) TF only. The absolute values are used for the plot. The color bars represent the amplitude (no unit) of the factors.

8.3 The new ISS attenuation algorithm

QF is related to the amplitude absorption of an event at a shallower depth, which is selected by the middle integral in Equation 8.1, but with a $Q/2$. For instance, $QF = e^{-\frac{|k_z|}{Q_0}z_1}$ in Equation 8.2, though $e^{-\frac{|k_z|}{2Q_0}z_1}$ is the exact amplitude absorption term of the first primary. With this realization, we modify the ISS algorithm by inputting two versions of datasets so as to remove QF expressed as

$$\hat{b}_3(k_z) = \int_{-\infty}^{\infty} b_1(z)e^{ik_z z}dz \int_{-\infty}^{z-\epsilon} c_1(z_1)e^{-ik_z z_1}dz_1 \int_{z_1+\epsilon}^{\infty} b_1(z_2)e^{ik_z z_2}dz_2, \tag{8.4}$$

where $c_1(z)$ in the middle integral is the dataset after amplitude-only compensation with half the estimated Q value; $\hat{b}_3$ is the prediction result from the new algorithm. The integrands of the outer two integrals remain uncompensated. Then the relationship between the predicted and the actual internal multiples turns to be (refer to Appendix H),

$$\frac{\hat{b}_3(k_z)}{IM(k_z)} = TF. \tag{8.5}$$

Consequently, carrying out Equation 8.4 can remove the influence (QF) that arises from the Q absorption and improve the prediction amplitude in an absorptive and dispersive medium.

8.4 Numerical tests

The new method is exemplified with two models with Q, one is a simple five-layer 1D model, and the other is a synthetic model with complicated structure.

8.4.1 Five-layer 1D model with Q

Table 8.1 lists the parameters of the model, which is used to generate 1D normal-incident data and pre-stack data. Both will be tested on the new attenuation algorithm.

Layer Number	Depth(m)	Velocity (m/s)	Density (kg/m^3)	Q
1	400	1500	1000	100
2	850	2000	1200	40
3	1200	2500	1500	80
4	3200	6500	3000	80
5		4000	3500	100

Tab. 8.1: A five layered model for 1D normal-incident data and pre-stack data generations.

Firstly, Figure 8.3 shows the multiple prediction result with 1D normal-incident plane-wave data. The predicted multiple (from both the current and the new algorithms) has a different polarity with the recorded multiple (there is a - sign in TF). For convenience, all the plots of the prediction results (in Figure 8.3, 8.4, 8.4, and 8.7) have been changed the polarities so as to be agree with the acquired data. The new method, that inputs two different datasets, with and without amplitude compensations, has an improved prediction amplitude when compared with the current one that only inputs data without Q compensation. It is worth mentioning that the prediction amplitude from the new method is still smaller than the actual multiple due to TF (in Equation 8.5), the transmission loss at the interfaces on and above the multiple generator.

Secondly, the new method is examined with a pre-stack data. Data with Q absorption (Figure 8.4(a)) are generated with PWTIM (a Schlumberger software implementing a reflectivity modeling method for 1D layered media). As a pre-processing, a amplitude compensation is done by using the inverse-Q method (OMEGA, a seismic processing software from Schlumberger). The prediction results (Figure 8.4(b) for the current method and 8.4(c) for the new method) draw a conclusion similar to the 1D normal incidence case: the predicted multiple from the new method provides a more accurate amplitude comparing to the current version.

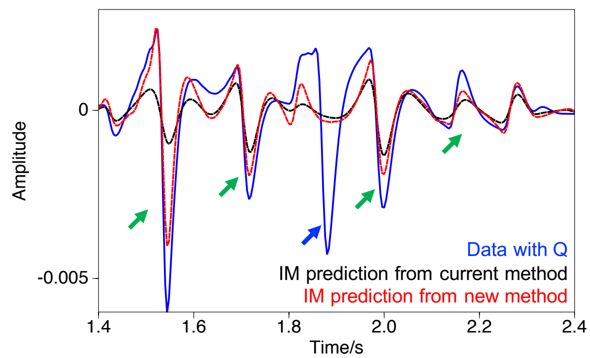

Fig. 8.3: Internal multiple prediction with 1D normal-incident data (1.4s-2.4s): the blue line is input data; the black line is the current prediction, and the red line is the new prediction. Green arrows point to the internal multiples; green arrow points to one primary event of data. IM is short for internal multiple. The unit of amplitude is N/m^2.

As those multiple events pointed by the arrows in Figure 8.5, the single trace plots at both offset 0m and offset 1250m further confirm the improvements.

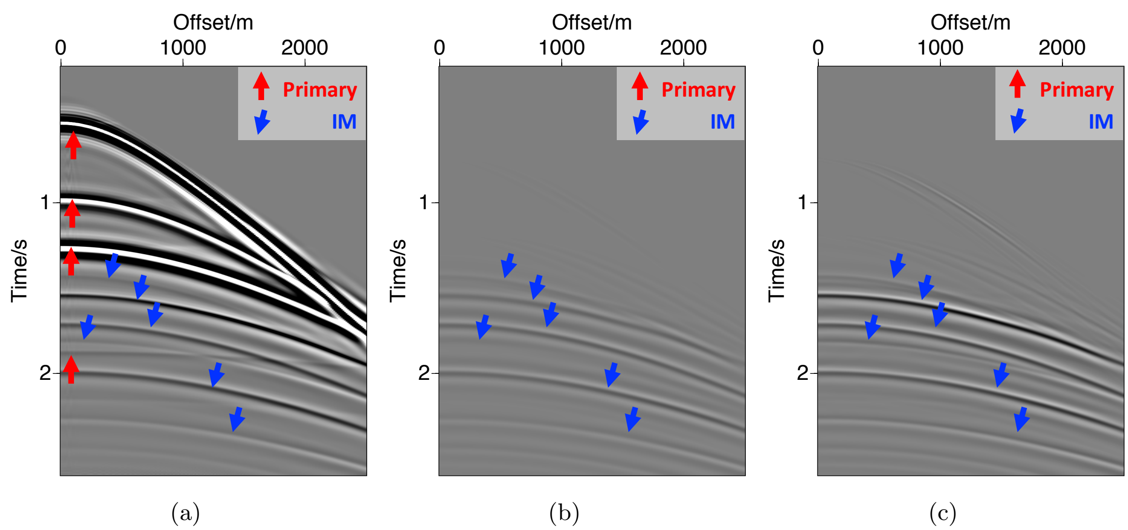

Fig. 8.4: Internal multiple prediction with pre-stack data: (a) input data with Q; (b) current prediction; (c) new prediction. Red and blue arrows point to primaries and multiples, respectively.

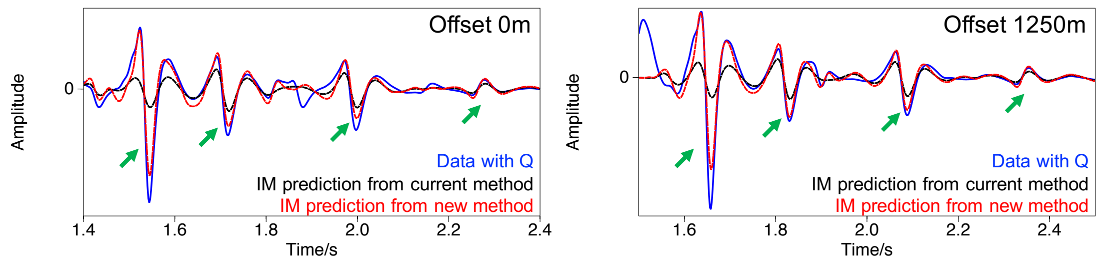

(a) (b)

Fig. 8.5: Single trace (from Figure 8.4) comparison: (a) offset 0m; (b) offset 1250m. The blue line shows data with Q; the black line shows current prediction; the red line shows new prediction. Green arrows indicate internal multiples. The unit of amplitude is N/m^2.

8.4.2 *Synthetic acoustic model with Q*

A synthetic acoustic model is used in this study (Thompson et al., 2003), modified by addition of attenuation parameters. Figure 8.6 shows its velocity, density and modified Q models in order.

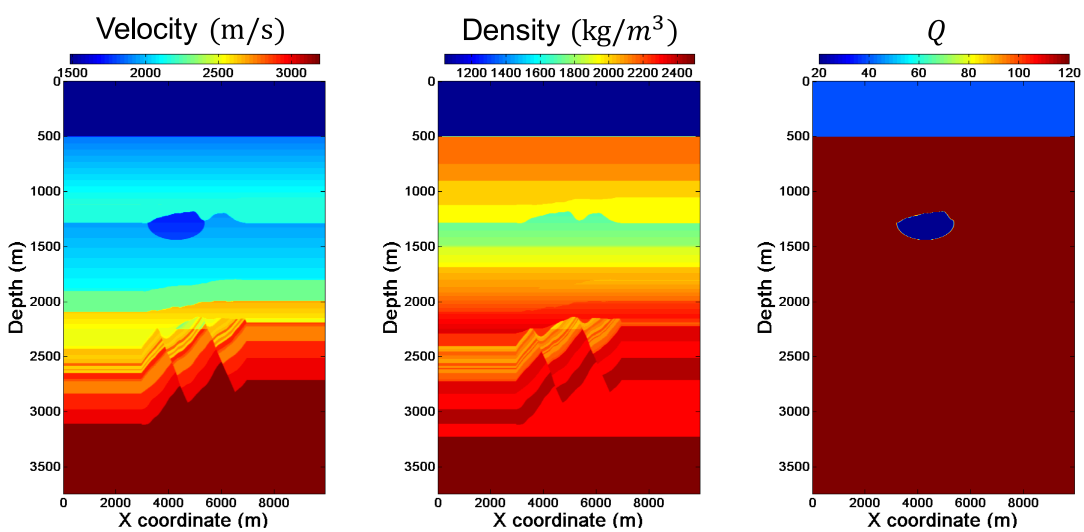

(a) (b) (c)

Fig. 8.6: A synthetic acoustic model: (a) velocity, (b) density, (c) modified Q (no unit). (Courtesy of Statoil)

As a starting point, we test a 1D normal-incidence plane-wave (reflectivity modeling strategy) at each single trace. Figure 8.7(a) is the input data with both primary and internal multiple, and Figure 8.7(b) is the isolated internal multiple of data. The multiple seriously interferes with the primary, and that interference could lead to a wrong interpretation. To better remove the multiple, the goal of multiple prediction is to predict the internal multiple with an amplitude as close to the actual one as possible. The plots in Figure 8.7(c) and 8.7 show that the result from the new method is brighter and closer to accuracy, while the prediction from the current one is much weaker.

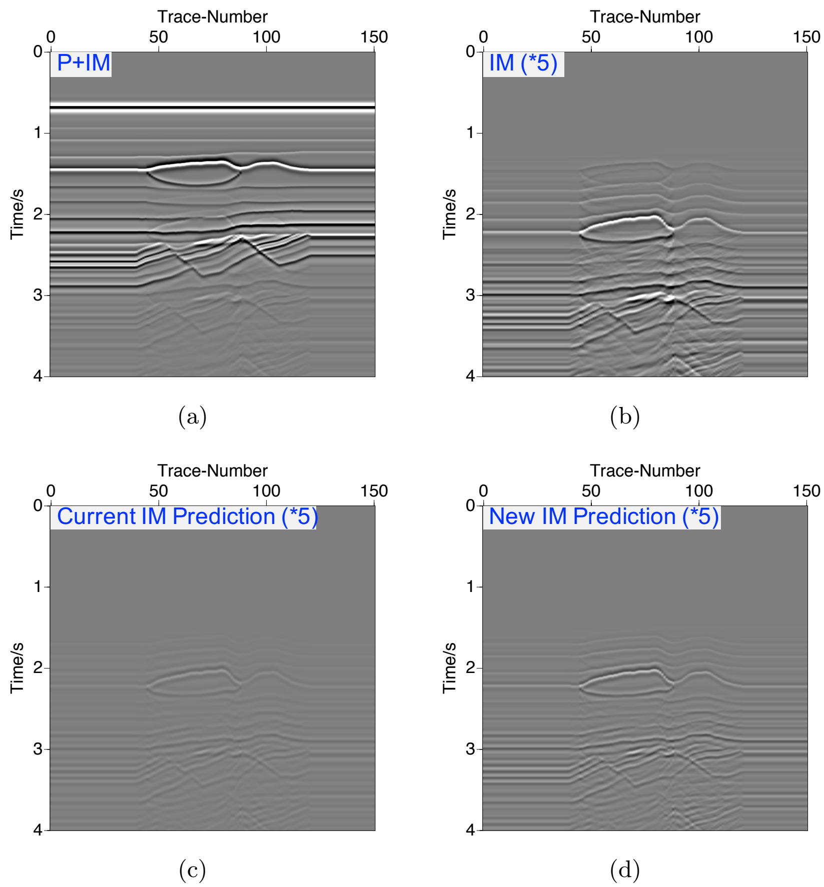

Fig. 8.7: 1D normal-incidence internal-multiple prediction with the model in Figure 6: (a) data with Q; (b) actual internal multiple; (c) current prediction; (d) new prediction. With respect to (a), the amplitudes of (b)-(d) are amplified by 5 times for clarity.

8.5 Conclusion

In the absorptive and dispersive exploration region, the current ISS attenuation algorithm can predict the internal multiple with accurate time; however, the absorption effect above the multiple generator can seriously reduce the prediction amplitude respecting to the actual multiple. We propose a new attenuation algorithm, that substitutes two datasets into the integrals with purpose. The outer terms are remaining not compensated, but the middle one is amplitude-compensated with half of estimated Q values. As a consequence, Qs influence on the relative amplitude difference can be removed and the prediction amplitude can be amplified. The improvement has been initially illustrated by normal-incident and pre-stack absorptive/dispersive data.

If the absorption is serious above the major internal multiple generators, the new solution can significantly improve the prediction, making the prediction amplitude closer to the actual multiple, reducing the burden of subsequent adaptive subtraction, and enhancing the potential of an effective internal multiple removal.

8.6 Acknowledgments

We thank Schlumberger for providing an internship opportunity to Jing Wu and for permission to publish.

We thank Kuwait Oil Company (KOC) for permission to use their log data in the study and to publish.

We thank Statoil for permission to use a synthetic acoustic model which they provided and to publish.

We are grateful for the helpful suggestions and software instructions from our Schlumberger colleagues Zhiming James Wu, Jae Young Park, Aanchal Jain, Glenn Miers, Scott Elliott and Maud Cavalca.

9. SUMMARY

This dissertation examines and addresses several challenging issues existing in seismic data processing. Among issues progressed within this thesis: (1) the removal of reference wave and ground roll in onshore plays, (2) ghost removal for marine, ocean bottom and onshore processing and (3), the attenuation of internal multiples in anelastic media.

I first progress and advance the capability of Green's theorem wave separation for more complicated offshore and onshore application. Three advances are made within this topic area.

Directly applying the current Green's theorem deghosting algorithm cannot deghost the recorded data themselves when the acquisition surface is not horizontal. This dissertation provides a two-step strategy to solve that problem. The new method retains the advantages of Green's theorem deghosting, i.e., it accommodates a non-horizontal measurement surface and doesn't assume or require any information about the source wavelet and its radiation pattern, the shape and the reflection coefficients at the air-water surface, and earth properties.

The application of Green's theorem deghosting is mature in marine towed streamer acquisition. I extend it to the ocean bottom acquisition. To deghost the acquired displacement data recorded at the seabed, an elastic reference medium is chosen and an elastic version of the Green's theorem deghosting algorithm is derived to accomplish the task.

One of the toughest problems in onshore exploration is ground roll removal. I develop the elastic Green's theorem wave separation algorithm which is able to separate the ground roll without injuring the reflection data. Noting the complete algorithm has a high demand for data acquisition (requiring both full multicomponent displacement and traction data to be recorded). That data requirement is rarely available from current acquisition capability. I further develop a simplified formula to achieve the goal of wave separation with a reduced data requirement (only requiring multicomponent displacement measurements and not traction). That reduced data requirement is comparable with current onshore acquisition capability.

Developing a more capable internal multiple prediction algorithm is of great importance for achieving a more successful internal multiple removal. The ISS method is uniquely advantageous for not needing any subsurface information. In the second part of this dissertation, I examine and improve the performance of the ISS internal multiple attenuation algorithm when the earth is anelastic. Absorption and dispersion can be significant in many exploration regions (e.g., in the pre-salt plays); however, analytical and numerical analyses show that the ISS attenuator retains its effectiveness to predict the accurate time and approximate amplitude of the internal multiples, and without requiring any elastic/inelastic subsurface information. The results further demonstrate that the ISS internal multiple attenuator is model-type independent. Notice that if the medium is anelastic, two factors will contribute to a smaller prediction amplitude in comparison with the actual multiples. One is related to the elastic transmission loss at the interfaces on and above the interface where the multiple has downward reflection, and the other one is related to the anelastic transmission loss in the layers above that interface where the downward reflection happens. To further improve the prediction amplitude and reduce the burden of the subsequent subtraction, we design a new algorithm to reduce the second factor by incorporating estimated Q information, when it is available and reliable.

REFERENCES

Aki, K., and P. G. Richards, 2002, Quantitative seismology, second ed.: University Science Books.

Amundsen, L., 1993, Wavenumber-based filtering of marine point-source data: Geophysics, **58**, 1335–1348.

Amundsen, L., A. Weglein, and A. Reitan, 2013a, On seismic deghosting using integral representation for the wave equation: Use of Green's functions with neumann or dirichlet boundary conditions: Geophysics, **78**, T89–T98.

Amundsen, L., and H. Zhou, 2013, Low-frequency seismic deghosting: Geophysics, **78**, WA15–WA20.

Amundsen, L., H. Zhou, A. Reitan, and A. Weglein, 2013b, On seismic deghosting by spatial deconvolution: Geophysics, **78**, V267–V271.

Araújo, F. V., 1994, Linear and non-linear methods derived from scattering theory: backscattered tomography and internal multiple attenuation: PhD thesis, Universidade Federal da Bahia.

Baeten, G., and A. Ziolkowski, 1990, The vibroseis source: Elsevier.

Bakulin, A., R. Burnstad, M. Jervis, and P. Kelamis, 2012, Evaluating permanent seismic monitoring with shallow buried sensors in a desert environment: SEG Expanded Abstracts, 1–5.

Baysal, E., D. Kosloff, and J. W. C. Sherwood, 1983, Reverse time migration: Geophysics, **48**, 1514–1524.

Carlson, D., A. Long, W. Söllner, H. Tabti, R. Tenghamn, and N. Lunde, 2007, Increased resolution and penetration from a towed dual-sensor streamer: First Break, **25**, 71–77.

Carvalho, P. M., 1992, Free-surface multiple reflection elimination method based on non-linear inversion of seismic data: PhD thesis, Universidade Federal da Bahia.

Claerbout, J. F., 1971, Toward a unified theory of reflector mapping: Geophysics, **36**, 467–481.

Coates, R., and A. B. Weglein, 1996, Internal multiple attenuation using inverse scattering: results from prestack 1D & 2D elastic synthetics: SEG Expanded Abstracts, 1522–1525.

Dave, M., 1993, Static corrections-a review, part i, part ii, part iii: The Leading Edge, **12**, 2.

Farouki, M., A. Long, and R. Tenghamn, 2010, Enhanced resolution, imaging and interpretability: Dual-sensor towed streamer data examples from around the world: Geohorizon, 19–23.

Innanen, K. A., and J. Lira, 2010, Direct nonlinear Q-compensation of seismic primaries reflecting from a stratified, two-parameter absorptive medium: Geophysics, **75**, V13–V23.

Innanen, K. A., and A. B. Weglein, 2003, Construction of absorptive/dispersive wave fields with the forward scattering series: Journal of Seismic Exploration, **12**, 259–282.

———, 2005, Towards non-linear construction of a q-compensation operator directly from reflection seismic data: SEG Expanded Abstracts, 1693–1696.

Keho, T. H., A. B. Weglein, and P. G. Rigsby, 1990, Marine source wavelet and radiation pattern estimation: SEG Expanded Abstracts, 1655–1657.

Kjartansson, E., 1979, Attenuation of seismic waves in rocks and applications in energy exploration: PhD thesis, Standford University.

Kolsky, H., 1956, The propagation of stress pulses in viscoelastic solids: Philos. Mag., **1**, 693–710.

Kostov, C., J. Wu, and D. Dishberger, 2017, Method for attenuating multiples. (US Patent App. 14/846,693).

Liang, H., and T. Keho, 2015, Deghosting 4d buried land sensor data using multi-component wavefield separation: SEG Expanded Abstracts, 2143–2147.

Lin, X., and A. B. Weglein, 2015, The significance of incorporating a 3-D point source in the inverse scattering series internal multiple attenuator for a 1-D subsurface: SEG Expanded Abstracts, 4391–4395.

Liu, F., and A. B. Weglein, 2014, The first wave equation migration RTM with data consisting of primaries and internal multiples: theory and 1D examples: Journal of Seismic Exploration, **23**, 357–366.

Ma, C., 2016, An inverse scattering series (ISS) data comprehensive internal multiple attenuation algorithm that accommodates primaries and internal multiples in the input data: PhD thesis, University of Houston.

Matson, K. H., 1997, An inverse-scattering series method for attenuating elastic multiples from multicomponent land and ocean bottom seismic data: PhD thesis, University of British Columbia.

Mayhan, J. D., P. Terenghi, A. B. Weglein, and N. Chemingui, 2011, Green's theorem derived methods for preprocessing seismic data when the pressure P and its normal derivative are measured: SEG Expanded Abstracts, 2722–2726.

Mayhan, J. D., and A. B. Weglein, 2013, First application of Green's theorem-derived source and receiver deghosting on deep-water Gulf of Mexico synthetic (SEAM) and field data: Geophysics, **78**, WA77–WA89.

McMechan, G. A., 1983, Migration by extrapolation of time-dependent boundary values: Geophysical Prospecting, **31**, 413–420.

McMechan, G. A., and M. J. Yedlin, 1981, Analysis of dispersive wave by wave field transformation: Geophysics, **46**, 869–874.

Moldoveanu, N., L. Combee, M. Egan, W. Abriel, and G. Hampson, 2006, Over/under towed streamer acquisition: A method to extend the seismic bandwidth to both, higher and lower frequencies: SEG Expanded Abstracts, 10–15.

Morse, P. M., and H. Feshbach, 1953, Methods of theoretical physics: McGraw-Hill Book

Co.

Neut, J., A. Bakulin, and D.Alexandrov, 2013, Acoustic wavefield separation using horizontal receiver arrays deployed at multiple depths on land: SEG Expanded Abstracts, 4601–4607.

Nolet, G., and G. F. Panza, 1976, Array analysis of seismic surface waves: Limits and possibilities: Pure and Applied Geophysics, **114**, 775–790.

Noorlandt, R., and G. Drijkoningen, 2016, On the mechanical vibrator-earth contact geometry and its dynamics: Geophysics, **81**, P23–P31.

O'Doherty, R. F., and N. A. Anstey, 1971, Reflections on amplitudes: Geophysical Prospecting, **19**, 430–458.

Osen, A., L. Amundsen, and A. Reitan, 1999, Removal of water-layer multiples from multicomponent sea-bottom data: Geophysics, **64**, 838–851.

Osen, A., B. G. Secrest, and L. Amundsen, 1998, Wavelet estimation from marine pressure measurements: Geophysics, **63**, 2108–2119.

Pao, Y. H., and V. Varatharajulu, 1976, Huygens principle, radiation conditions, and integral formulas for the scattering of elastic waves: J. Acoust. Soc. Am., **59**, 1361–1371.

Piété, H., L. Marié, B. Marsset, Y. Thomas, and M. A. Gutscher, 2013, Seismic reflection imaging of shallow oceanographic structures: Journal of Geophysical Research: Oceans, **118**, 2329–2344.

Shen, Y., and A. B. Weglein, 2017, Impact of the shape of the acquisition surface on the effectiveness of the ISS internal multiple attenuation and elimination algorithms: analyzing the problem and providing a response to the challenge: SEG Expanded Abstracts, accepted.

Socco, L., S. Foti, and D. Boiero, 2010, Surface-wave analysis for building near-surface velocity models-established approaches and new perspectives: Geophysics, **75**, A83–A102.

Sommerfeld, A., 1949, Partial differential equation in physics: New York: Academic Press.

Tan, T. H., 1999, Wavelet spectrum estimation: Geophysics, **64**, 1836–1846.

Thompson, M., B. Arntsen, and L. Amundsen, 2003, Acquisition geometry versus 4c image quality. A study from gullfaks south: SEG Expanded Abstracts, 793–796.

van Borselen, R., J. Fokkema, and P. van den Berg, 2013, Wavefield decomposition based on acoustic reciprocity: Theory and applications to marine acquisition: Geophysics, **78**, WA41–WA54.

Wang, P., and C. Peng, 2012, Premigration deghosting for marine towed streamer data using a bootstrap approach: SEG Expanded Abstracts, 1–5.

Weglein, A. B., 2015, Multiple removal: open issues, pressing challenges and recent progress towards providing the next and higher level of required capability: SEG Expanded Abstracts, 4555–4562.

———, 2016, Multiples: Signal or noise?: Geophysics, **81**, V283–V302.

Weglein, A. B., F. V. Araújo, P. M. Carvalho, R. H. Stolt, K. H. Matson, R. T. Coates, D. Corrigan, D. J. Foster, S. A. Shaw, and H. Zhang, 2003, Inverse scattering series and seismic exploration: Inverse Problems, **19**, R27–R83.

Weglein, A. B., and W. H. Dragoset, 2005, Multiple attenuation.: Soc. Expl. Geophys. Geophysics reprint series.

Weglein, A. B., F. A. Gasparotto, P. M. Carvalho, and R. H. Stolt, 1997, An inverse-scattering series method for attenuating multiples in seismic reflection data: Geophysics, **62**, 1975–1989.

Weglein, A. B., and K. H. Matson, 1998, Inverse scattering internal multiple attenuation: an analytic example and subevent interpretation: SPIE Conference on Mathematical Methods in Geophysical Imaging, 108–117.

Weglein, A. B., J. Mayhan, L. Amundsen, H. Liang, J. Wu, L. Tang, Y. Luo, and Q. Fu, 2013, Green's theorem deghosting algorithms in (k, ω) as a special case of (x, ω) algorithms.: Journal of Seismic Exploration, **22**, 389–412.

Weglein, A. B., and B. G. Secrest, 1990, Wavelet estimation for a multidimensional acoustic earth model: Geophysics, **55**, 902–913.

Weglein, A. B., S. A. Shaw, K. H. Matson, J. L. Sheiman, R. H. Solt, T. H. Tan, A. Osen, G. P. Correa, K. A. Innanen, Z. Guo, and J. Zhang, 2002, New approaches to deghosting towed-streamer and ocean-bottom pressure measurements: SEG Expanded Abstracts, 1016–1019.

Weglein, A. B., R. Stolt, and J. Mayhan, 2011a, Reverse-time migration and Green's theorem: Part I - the evolution of concepts, and setting the stage for the new RTM method: Journal of Seismic Exploration, **20**, 73–90.

———, 2011b, Reverse time migration and Green's theorem: Part II - a new and consistent theory that progresses and corrects current rtm concepts and methods: Journal of Seismic Exploration, **20**, 135–159.

Weglein, A. B., and R. H. Stolt, 1995, I. the wave physics of downward continuation, wavelet estimation and volume and surface scattering. II. approaches to linear and non-linear migration inversion: Mathematical Frontiers in Reflection Seismology: SEG/SIAM publication.

Whitmore, N. D., 1983, Iterative depth migration by backward time propagation: SEG Expanded Abstracts, 382–385.

Wu, J., and A. B. Weglein, 2014, The first test and evaluation of the inverse scattering series internal multiple attenuation algorithm for an attenuating medium: SEG Expanded Abstracts, 4130–4134.

———, 2015a, Preprocessing in displacement space for on-shore seismic processing: removing ground roll and ghosts without damaging the reflection data: SEG Expanded Abstracts, 4626–4630.

———, 2015b, Preprocessing in PS space for on-shore seismic processing: removing ground roll and ghosts without damaging the reflection data: SEG Expanded Abstracts, 4740–4744.

———, 2016a, Green's theorem-based onshore preprocessing: A reduced data requirement assuming a vacuum/earth model for the air/earth interface and the evaluation of the usefulness of that assumption: SEG Expanded Abstracts, 4685–4689.

———, 2016b, Predicting deghosted reflection data for both pressure and multicomponent displacements at the ocean bottom: SEG Expanded Abstracts, 4751–4755.

———, 2017, A new method for deghosting data collected on a depth-variable acquisition surface by combining Green's theorem wave separation followed by a Stolt extended Claerbout iii wave prediction for one-way propagating waves: SEG Expanded Abstracts, accepted.

Yilmaz, O., 2001, Seismic data analysis: Processing, inversion and interpretation of seismic data: Society of Exploration Geophysicists.

Zhang, H., 2006, Direct non-linear acoustic and elastic inversion: Towards fundamentally new comprehensive and realistic target identification: PhD thesis, University of Houston.

Zhang, J., 2007, Wave theory based data preparation for inverse scattering multiple removal, depth imaging and parameter estimation: analysis and numerical tests of Green's theorem deghosting theory: PhD thesis, University of Houston.

Zhang, J., and A. B. Weglein, 2006, Application of extinction theorem deghosting method on ocean bottom data: SEG Expanded Abstracts, 2674–2678a.

Zhang, Z., and A. B. Weglein, 2017, 3D source and receiver deghosting in the space-frequency domain using a depth-variable measurement surface: an initial off-shore synthetic data study with anticipated on-shore and ocean bottom application: SEG Expanded Abstracts, accepted.

Zou, Y., and A. B. Weglein, 2013, A new method to eliminate first order internal multiples for a normal incidence plane wave on a 1D earth: SEG Expanded Abstracts, 4136–4140.

———, 2015, An internal-multiple elimination algorithm for all first-order internal multiples for a 1D earth: SEG Expanded Abstracts, 4408–4412.

APPENDICES

A. COMPARISON BETWEEN GREEN'S THEOREM WAVEFIELD PREDICTION AND CONVENTIONAL ELEVATION STATIC CORRECTION

[1] Elevation static correction is the static correction made to each seismic trace for elevation effects by conceptually moving the shots and receivers to a common reference surface (which is usually horizontal). It involves a constant time shift to the data trace (Dave (1993)). The simplest way to calculate the constant time shift is the following

$$\Delta t = \frac{E_r - E_a}{c}, \tag{A.1}$$

where E_r is the elevation of the receiver on the reference measurement surface, E_a is the elevation of the receiver on the actual measurement surface, and c is the velocity of the medium. The elevation static correction shifts each trace of the data by their corresponding Δt and moves the actual measurement surface to the reference measurement surface. A detail tutorial on static correction can be found in Yilmaz (2001).

However, the elevation static correction is based on ray theory and is an approximation for a more complex problem (Dave (1993)). According to wave theory, moving the receiver from one elevation to another involves a surface integral of the data (Weglein et al., 2011a,b). Although the elevation static correction can serve as a good approximation for near-offset data, it will cause problems when the data comes from large offset.

Below shows an example. A one-reflector acoustic model demonstrated by A.1 is used to

[1] This appendix is cited from the dissertations of Yuchang Shen and Zhen Zhang.

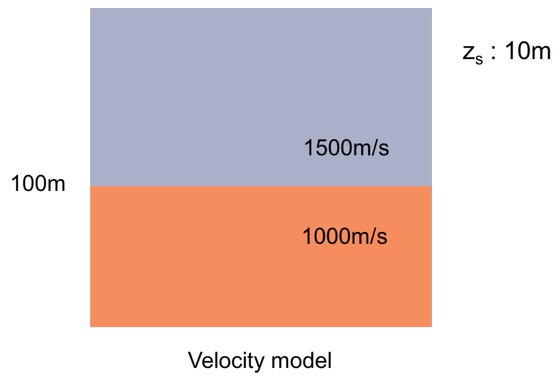

Fig. A.1: The acoustic model that generate the data for the second example.

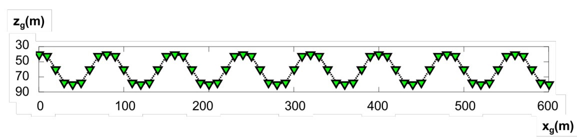

Fig. A.2: The acquisition surface in the second example.

generate the data. The data is collected by an acquisition surface that consist of several identical semi-circles shown in figure A.2. The average depth of the acquisition surface is 60m and the radii of the semi-circles are 25m. We only generated one primary event in this case. We will then use both the elevation static correction method and Green's theorem wavefield prediction method to predict the data from the current acquisition surface to a shallower horizontal acquisition surface located at depth 30m.

Figure A.3 shows the input data generated from the model. Figure A.4 shows the prediction shot gather by elevation static correction method at depth 30m and figure A.5 shows the prediction shot gather by Green's theorem wavefield prediction method at depth 30m. Comparing these two results we can find that at far offset the arrival time of the predicted events are not the same.

A more detail comparison can be illustrated by the trace comparison. Figure A.6 shows the trace comparison at different offsets between the perfect result generated analytically at depth 30m (blue solid line), the prediction by Green's theorem wavefield prediction method

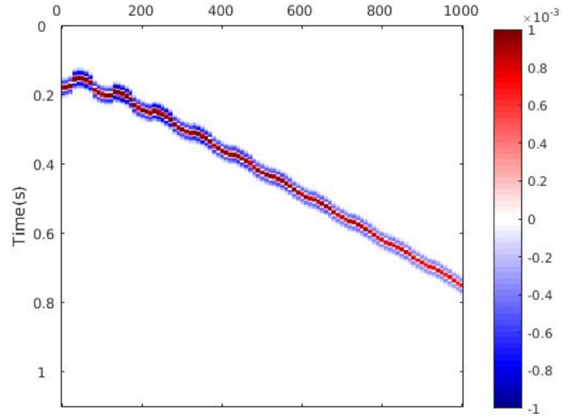

Fig. A.3: The input data. The color bars in this figure, Figure A.4 and Figure A.5 represent the amplitude (unit of N/m^2) of wavefield.

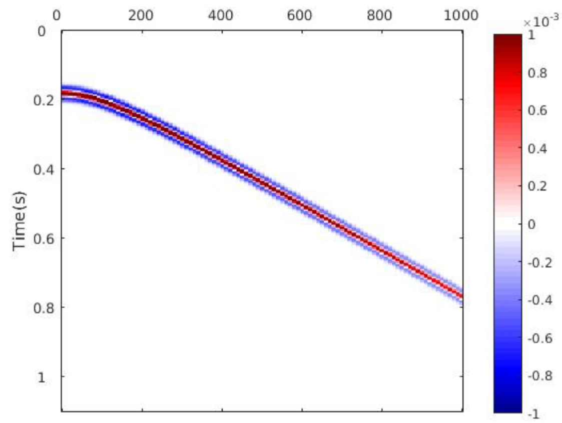

Fig. A.4: Prediction result by elevation static correction at depth 30m.

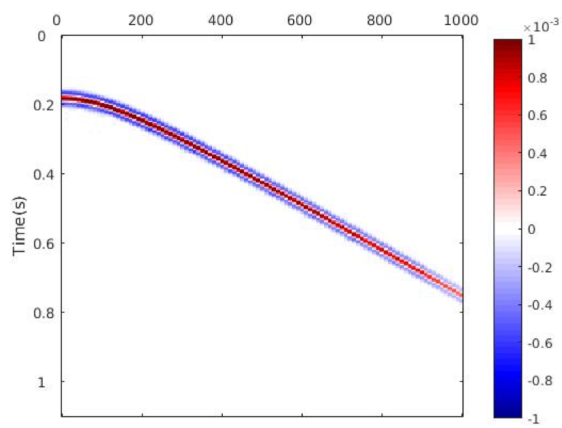

Fig. A.5: Prediction result by Green's theorem wavefield prediction at depth 30m.

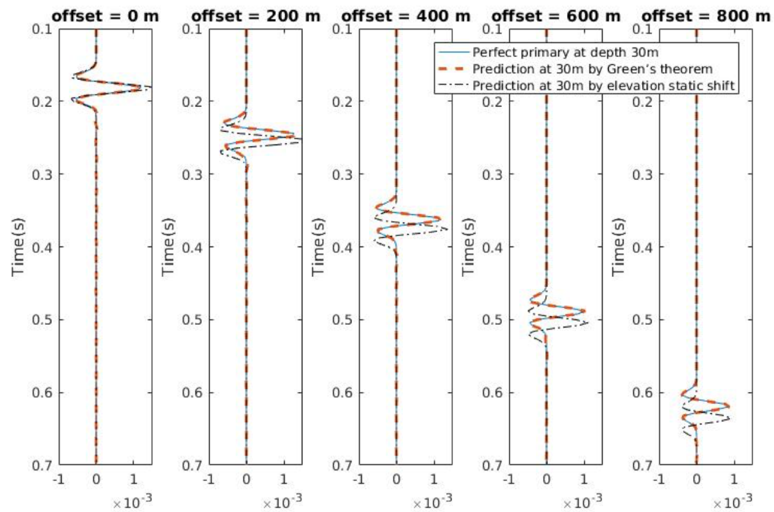

Fig. A.6: Trace comparison between the perfect result generated analytically at depth 30m (blue solid line), the prediction by Green's theorem wavefield prediction method (red dashed line), and the prediction by elevation static correction method (black dashed line) at different offsets. The horizontal axis represents the amplitude (unit of N/m^2) of wavefield.

(red dashed line), and the prediction by elevation static correction method (black dashed line). These trace comparisons show that, the elevation static correction method can only provide a prediction with exact time at 0m offset. As the offset gets bigger, the time of the static correction result deviates more from the perfect result. The amplitude of the static correction result deviates from the perfect result at every offset. On the other hand, the prediction result from the Green's theorem wavefield prediction matches the the perfect result very well at every offset.

The behavior of the elevation static correction method can be explained by a mathematical analysis provided by Weglein (personal communication, 2017). The elevation static correction method can be described by the following equation

$$D\left(x_g, z, t\right) = D\left(x_g, z_g, t - \Delta t\right) \tag{A.2}$$

Equation A.2 can be derived from the wave equation as the following. Starting from the wave equation

$$\left(\nabla^2 - \frac{1}{c^2}\frac{\partial^2}{\partial t^2}\right) D\left(x_g, z_g, t\right) = 0. \tag{A.3}$$

Fourier transform over x and t,

$$\left(\frac{d^2}{dz^2} + \frac{\omega^2}{c^2} - k_g^2\right) D\left(k_g, z_g, \omega\right) = 0 \tag{A.4}$$

In the Fourier domain, for a one-way wave prediction,

$$D\left(k_g, z, \omega\right) = e^{-ik_z(z-z_g)} D\left(k_g, z_g, \omega\right) \tag{A.5}$$

where

$$k_z = \sqrt{\frac{\omega^2}{c^2} - k_g^2}. \tag{A.6}$$

When k_g is small, $k_z \approx \omega/c$, so that

$$e^{-ik_z(z-z_g)} \approx e^{-i\frac{\omega}{c}(z-z_g)} = e^{i\omega\Delta t}. \tag{A.7}$$

Therefore

$$D\left(k_g, z, \omega\right) \approx e^{i\omega\Delta t} D\left(k_g, z_g, \omega\right). \tag{A.8}$$

With a stationary phase approximation (high frequency approximation),

$$\begin{aligned} D\left(x_g \approx 0, z, t\right) &\approx \int D\left(k_g \approx 0, z, t\right) e^{-i\omega t} d\omega \\ &= \int e^{i\omega\Delta t} D\left(k_g, z_g, \omega\right) e^{-i\omega t} d\omega \\ &= D\left(x_g \approx 0, z_g, t - \Delta t\right). \end{aligned} \tag{A.9}$$

So that, at near offset $x_g \approx 0$, we have

$$D\left(x_g, z, t\right) = D\left(x_g, z_g, t - \Delta t\right). \tag{A.10}$$

From the above analysis we know that elevation static correction has an assumption of a horizontal acquisition surface since it involves a fourier transform at the beginning. It also involves a stationary phase approximation, which requires $k_g \approx 0$ or $x_g \approx 0$. The stationary phase approximation implies a near offset or a high frequency approximation, or equivalently, a normal incident approximation in the elevation static correction method.

B. INITIAL STUDY OF THE SEPARATION OF THE WAVE GENERATED BY THE NEAR SURFACE WITHOUT NEAR SURFACE INFORMATION AND WITHOUT DAMAGING REFLECTION DATA

We show an initial study of separating a portion of wavefield due to the near surface without providing the near surface information.

Wave separation by using Green's theorem employs a model of the world that consists of a reference medium and sources. The choice of reference medium will determine what the sources have to be in order to arrange for the reference medium and the sources together to correspond to the actual medium and to the experiment. Figure B.1(a) shows a two-layer model with velocity c_1 over velocity c_2. The energy source is at depth z_s. The receiver is at depth z_g. The interface is the origin with z=0. For this example, we choose the reference medium to be a homogeneous whole space with velocity c_1 (Figure B.1(b)). Consider a 1D normal incidence wave, Then the wave equation for the field can be expressed as

$$(\partial_z^2 + k_1^2)P(z,\omega) = \rho, \tag{B.1}$$

where $k_1 = \omega/c_1$, P is the total wavefield, and ρ is the source term.

For this specific example and measurement location, there are three sources (Figure B.1(c)) acting on the reference medium: ρ_1 is the energy source (that is assumed to have a time dependence, $A(t)$ and be local in space), ρ_2 is the perturbation below the interface (at depth of 0) and above the measurement surface (at depth of z_g), and ρ_3 is the perturbation below the measurement surface. The three sources are

$$
\begin{aligned}
\rho_1 &= A(\omega)\delta(z - z_s), \\
\rho_2 &= k_1^2 \alpha_T P, \\
\rho_3 &= k_1^2 \alpha_B P,
\end{aligned}
\tag{B.2}
$$

where $A(\omega)$ is the source signature, and

$$
\begin{aligned}
\alpha_T &= (1 - \frac{c_1^2}{c_2^2})[H(z - z_g) - H(z)], \\
\alpha_B &= (1 - \frac{c_1^2}{c_2^2})H(z - z_g),
\end{aligned}
\tag{B.3}
$$

where H is Heaviside function, and $H(z) = \begin{cases} 1 & z > 0 \\ 0 & z < 0 \end{cases}$.

The total wavefield P can be expressed as

$$
P(z) = \int (\rho_1(z') + \rho_2(z') + \rho_3(z'))G_0(z, z')dz', \tag{B.4}
$$

where G_0 is the causal whole-space Green's function in the homogeneous reference medium. G_0 has an analytic expression:

$$
G_0(z, z') = \frac{1}{2ik_1} e^{ik_1|z - z'|}. \tag{B.5}
$$

For a point z (Figure B.1(c)) that is below the measurement surface, the total wave is

$$
P(z) = \frac{1}{2ik_1} A(\omega) T_1 e^{-ik_1 z_s} e^{ik_2 z}, \tag{B.6}
$$

where $T_1 = \frac{2c_2}{c_1 + c_2}$ is the transmission coefficient and $k_2 = \omega / c_2$. At z, the contribution from

ρ_1 and ρ_2 are both downgoing can be expressed analytically,

$$\begin{aligned}
P_{\rho_1}(z) &= \int \rho_1(z')G_0(z,z')dz' = \frac{1}{2ik_1}A(\omega)e^{ik_1(z-z_s)}, \\
P_{\rho_2}(z) &= \int \rho_2(z')G_0(z,z')dz' = \int_0^{z_g} k_1^2(1-\frac{c_1^2}{c_2^2})\frac{1}{2ik_1}A(\omega)T_1e^{-ik_1z_s}e^{ik_2z'}G_0(z,z')dz' \\
&= \frac{1}{2ik_1}A(\omega)e^{ik_1(-z_s)}e^{ik_2z_g}e^{ik_1(z-z_g)} - \frac{1}{2ik_1}A(\omega)e^{ik_1(z-z_s)},
\end{aligned} \tag{B.7}$$

where P_{ρ_1}, and P_{ρ_2} are the portion of wavefield due to source ρ_1 and ρ_2, respectively. The contribution from ρ_1 and ρ_2 are both downgoing and the sum is

$$P_{\rho_1+\rho_2}(z) = P_{\rho_1}(z) + P_{\rho_2}(z) = \frac{1}{2ik_1}A(\omega)e^{ik_1(-z_s)}e^{ik_2z_g}e^{ik_1(z-z_g)}. \tag{B.8}$$

Now let's perform the Green's theorem wave separation algorithm and evaluate the result inside the volume at z (as shown in Figure B.1(c)),

$$\begin{aligned}
P_d(z) &= -[P(z')\frac{dG_0(z,z')}{dz'} - G_0(z,z')\frac{dP(z')}{dz'}]|_{z'=z_g} \\
&= -[\frac{1}{2ik_1}A(\omega)T_1e^{-ik_1z_s}e^{ik_2z'}\frac{-1}{2}e^{ik_1(z-z')} - \frac{1}{2ik_1}e^{ik_1(z-z')}\frac{ik_2}{2ik_1}A(\omega)T_1e^{-ik_1z_s}e^{ik_2z'}]|_{z'=z_g} \\
&= \frac{1}{2}(1+\frac{k_2}{k_1})\frac{1}{2ik_1}A(\omega)T_1e^{-ik_1z_s}e^{ik_2z_g}e^{ik_1(z-z_g)} \\
&= \frac{1}{2ik_1}A(\omega)e^{-ik_1z_s}e^{ik_2z_g}e^{ik_1(z-z_g)} \\
&= P_{\rho_1+\rho_2}(z).
\end{aligned} \tag{B.9}$$

The result demonstrates that Green's theorem algorithm can separate the portion of the wavefield due to the source outside the volume.

On the other hand, we can analytically compute the portion of wavefield at z due to source inside the volume, which is ρ_3,

$$
\begin{aligned}
P_{\rho_3}(z) &= \int \rho_3(z')G_0(z,z')dz' \\
&= \int_{z_g}^{\infty} k_1^2(1-\frac{c_1^2}{c_2^2})\frac{1}{2ik_1}A(\omega)T_1e^{-ik_1z_s}e^{ik_2z'}\frac{1}{2ik_1}e^{ik_1|z-z'|}dz' \\
&= \int_{z_g}^{z} k_1^2(1-\frac{c_1^2}{c_2^2})\frac{1}{2ik_1}A(\omega)T_1e^{-ik_1z_s}e^{ik_2z'}\frac{1}{2ik_1}e^{ik_1(z-z')}dz' \\
&+ \int_{z}^{\infty} k_1^2(1-\frac{c_1^2}{c_2^2})\frac{1}{2ik_1}A(\omega)T_1e^{-ik_1z_s}e^{ik_2z'}\frac{1}{2ik_1}e^{ik_1(z'-z)}dz' \\
&= \frac{1}{2ik_1}(1-\frac{c_1^2}{c_2^2})\frac{k_1}{2i}A(\omega)T_1e^{-ik_1z_s}e^{ik_1z}\frac{1}{i(k_2-k_1)}[e^{i(k_2-k_1)z'}]|_{z'=z_g}^{z'=z} \\
&+ \frac{1}{2ik_1}(1-\frac{c_1^2}{c_2^2})\frac{k_1}{2i}A(\omega)T_1e^{-ik_1z_s}e^{ik_1z}\frac{1}{i(k_2+k_1)}[e^{i(k_2+k_1)z'}]|_{z'=z}^{z'=\infty} \\
&= \frac{1}{2ik_1}A(\omega)e^{-ik_1z_s}e^{ik_2z} - \frac{1}{2ik_1}A(\omega)e^{-ik_1z_s}e^{ik_2z_g}e^{ik_1(z-z_g)} \\
&+ \frac{1}{2ik_1}A(\omega)R_1e^{-ik_1z_s}e^{ik_2z} \\
&= \frac{1}{2ik_1}A(\omega)T_1e^{-ik_1z_s}e^{ik_2z} - \frac{1}{2ik_1}A(\omega)e^{-ik_1z_s}e^{ik_2z_g}e^{ik_1(z-z_g)} \\
&= P(z) - \frac{1}{2ik_1}A(\omega)e^{-ik_1z_s}e^{ik_2z_g}e^{ik_1(z-z_g)}
\end{aligned}
\tag{B.10}
$$

where P_{ρ_3} is the field caused by ρ_3; $R_1 = (\frac{c_2-c_1}{c_2+c_1})$.

Notice that there is one term $\frac{1}{2ik_1}(1-\frac{c_1^2}{c_2^2})\frac{k_1}{2i}A(\omega)T_1e^{-ik_1z_s}e^{ik_1z}\frac{1}{i(k_2+k_1)}[e^{i(k_2+k_1)z'}]|^{z'=\infty} = 0$, that can be achieved by adding a small friction on the k_1 and k_2 to be $k_{1'} = k_1 + i\epsilon$ and $k_{2'} = k_2 + i\epsilon$, and letting $\epsilon \to 0$ after the calculation,

$\lim_{\epsilon\to 0} \frac{1}{2ik_{1'}}(1-\frac{c_1^2}{c_2^2})\frac{k_{1'}}{2i}A(\omega)T_1e^{-ik_{1'}z_s}e^{ik_{1'}z}\frac{1}{i(k_{2'}+k_{1'})}[e^{i(k_2+k_1)z'}e^{-2\epsilon z'}]|^{z'=\infty} = 0.$

If we add the portion of wavefield at z due to ρ_3 to $P_d(z)$, we can get

$$
\begin{aligned}
P_d(z) + P_{\rho_3}(z) =& \frac{1}{2ik_1}A(\omega)e^{-ik_1z_s}e^{ik_2z_g}e^{ik_1(z-z_g)} + P(z) - \frac{1}{2ik_1}A(\omega)e^{-ik_1z_s}e^{ik_2z_g}e^{ik_1(z-z_g)} \\
=& P(z)
\end{aligned}
\tag{B.11}
$$

The sum of sources outside the volume and inside the volume gives the actual total wavefield at z. The theory communicates that if we describe the real world in terms of reference and sources, then the selected reference together with its corresponding sources should represent the real world and experiment. The calculation in Equation B.11 agrees with this theory and the separation result from Green's theorem is essentially accurate.

In a further step, if we move the output z upward to measurement depth z_g,

$$\begin{aligned} P_d(z_g) &= \frac{1}{2ik_1} A(\omega) e^{-ik_1 z_s} e^{ik_2 z_g}, \\ P_{\rho_3}(z_g) &= \frac{1}{2ik_1} A(\omega) T_1 e^{-ik_1 z_s} e^{ik_2 z_g} - \frac{1}{2ik_1} A(\omega) e^{-ik_1 z_s} e^{ik_2 z_g} \\ &= \frac{1}{2ik_1} A(\omega) R_1 e^{-ik_1 z_s} e^{ik_2 z_g} \\ P_d(z_g) + P_{\rho_3}(z_g) &= \frac{1}{2ik_1} A(\omega) T_1 e^{-ik_1 z_s} e^{ik_2 z_g} = P(z_g). \end{aligned} \tag{B.12}$$

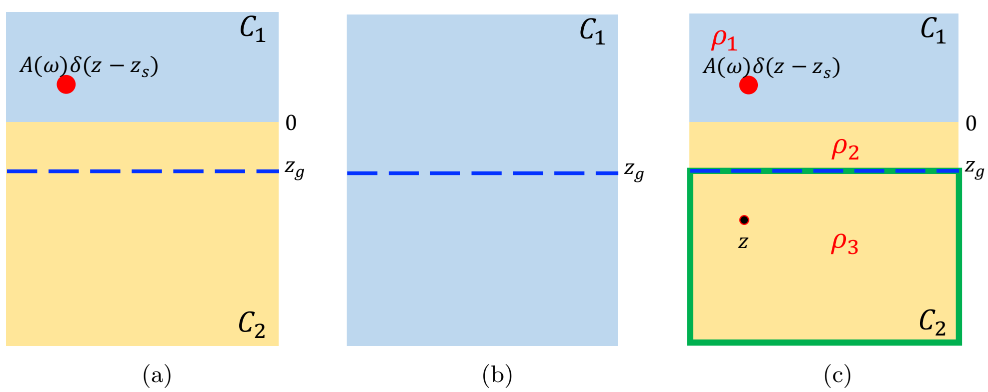

Fig. B.1: Illustration of wavefield separation. (a) the experiment; (b) the reference medium; (c) three sources (ρ_1, ρ_2 and ρ_3) act on the reference medium and the surface integral along S' (highlighted with green) can separate the contribution by ρ_1 and ρ_2 at point z inside the volume. Red star is the energy source and blue dashed line is measurement surface.

Comparing the separation result of Equation B.12 which is the downgoing wave produced by ρ_1 and ρ_2 at z_g and the total downgoing wave at z_g. We can understand the time is exact and the amplitude is not the same. That is because the contribution due to source inside the volume is extinguished after applying the Green's theorem algorithm.

Notice that while performing the algorithm, we input the measured data $P(z_g)$ and its normal derivative and the Green's function of the reference medium; however, we don't provide any information about the sources. Therefore, the portion of wavefield due to the near surface perturbation (If we treat that interface as an air/earth interface, then the near surface perturbation is characterized by source ρ_2.) can be separated without requiring any information about ρ_2.

This idea could be used to compute the downgoing wave at the measurement surface that depends on near surface properties without needing to know near surface properties.

C. DERIVATION OF 2D ELASTIC GREEN'S THEOREM WAVE SEPARATION IN THE DISPLACEMENT SPACE

Following Pao and Varatharajulu (1976), and with some modification, this section derives 2D elastic Green's theorem wave separation algorithm in $(\vec{r}, \omega)$ domain. $\vec{u}(\vec{r}', \omega)$ represents the displacement at $\vec{r}'$ in the actual medium (with $\rho(\vec{r}')$, $\lambda(\vec{r}')$, and $\mu(\vec{r}')$); $\boldsymbol{G}_0(\vec{r}', \vec{r}, \omega)$ represents the Green's displacement at $\vec{r}'$ by a source at $\vec{r}$ in the reference medium (with $\rho_0(\vec{r}')$, $\lambda_0(\vec{r}')$, and $\mu_0(\vec{r}')$).

$\boldsymbol{G}_0(\vec{r}', \vec{r}, \omega)$ satisfies

$$\nabla' \cdot \boldsymbol{\Sigma}_0(\vec{r}', \vec{r}, \omega) + \rho_0(\vec{r}')\omega^2 \boldsymbol{G}_0(\vec{r}', \vec{r}, \omega) = \delta(\vec{r}' - \vec{r})\, \boldsymbol{I}, \tag{C.1}$$

where,

$$\Sigma_{0ijk}(\vec{r}', \vec{r}, \omega) = \lambda_0(\vec{r}')\partial_{m'} G_{0mk}(\vec{r}', \vec{r}, \omega)\delta_{ij} + \mu_0(\vec{r}')(\partial_{i'} G_{0jk}(\vec{r}', \vec{r}, \omega) + \partial_{j'} G_{0ik}(\vec{r}', \vec{r}, \omega)) \; i, j, k = x, z \tag{C.2}$$

$\vec{u}(\vec{r}', \omega)$ satisfies

$$\nabla' \cdot \boldsymbol{\tau}(\vec{r}', \omega) + \rho(\vec{r}')\omega^2 \vec{u}(\vec{r}', \omega) = \vec{f}(\vec{r}', \omega), \tag{C.3}$$

where

$$\boldsymbol{\tau}(\vec{r}', \omega) = \lambda(\vec{r}')\nabla' \cdot \vec{u}(\vec{r}', \omega)\, \boldsymbol{I} + \mu(\vec{r}') \left(\nabla' \vec{u}(\vec{r}', \omega) + \vec{u}(\vec{r}', \omega)\nabla' \right). \tag{C.4}$$

To make the parameters of left side of Equation C.3 to be consistent with that of Equation

C.1, we rewrite Equation C.3 as

$$\begin{aligned}&\nabla' \cdot \boldsymbol{\tau_1}(\vec{r}',\omega) + \rho_0(\vec{r}')\omega^2\vec{u}(\vec{r}',\omega) = \vec{f}(\vec{r}',\omega) - (\rho(\vec{r}') - \rho_0(\vec{r}'))\omega^2\vec{u}(\vec{r}',\omega)\\ &- \nabla' \cdot [(\lambda(\vec{r}') - \lambda_0(\vec{r}'))\nabla' \cdot \vec{u}(\vec{r}',\omega)\,\boldsymbol{I} + (\mu(\vec{r}') - \mu_0(\vec{r}'))(\nabla'\vec{u}(\vec{r}',\omega) + \vec{u}(\vec{r}',\omega)\nabla')]\end{aligned}, \tag{C.5}$$

and

$$\boldsymbol{\tau_1}(\vec{r}',\omega) = \lambda_0(\vec{r}')\nabla' \cdot \vec{u}(\vec{r}',\omega)\,\boldsymbol{I} + \mu_0(\vec{r}')(\nabla'\vec{u}(\vec{r}',\omega) + \vec{u}(\vec{r}',\omega)\nabla'). \tag{C.6}$$

Now we rename $\boldsymbol{\tau_1}$ as $\boldsymbol{\tau}$, rename $\vec{f} - (\rho - \rho_0)\omega^2\vec{u} - \nabla' \cdot [(\lambda - \lambda_0)\nabla' \cdot \vec{u}\,\boldsymbol{I} + (\mu - \mu_0)(\nabla'\vec{u} + \vec{u}\nabla')]$ as $\vec{f}$; therefore, $\vec{f}$ becomes a generalized source, including both the active source and the passive sources due to ai or earth perturbation. Equation C.5 and Equation C.6 can be rewritten as

$$\nabla' \cdot \boldsymbol{\tau}(\vec{r}',\omega) + \rho_0(\vec{r}')\omega^2\vec{u}(\vec{r}',\omega) = \vec{f}(\vec{r}',\omega), \tag{C.7}$$

$$\boldsymbol{\tau}(\vec{r}',\omega) = \lambda_0(\vec{r}')\nabla' \cdot \vec{u}(\vec{r}',\omega)\,\boldsymbol{I} + \mu_0(\vec{r}')(\nabla'\vec{u}(\vec{r}',\omega) + \vec{u}(\vec{r}',\omega)\nabla'). \tag{C.8}$$

Multiplying Equation C.7 with $\boldsymbol{G}_0(\vec{r}',\vec{r},\omega)$, multiplying Equation C.1 with $\vec{u}(\vec{r}',\omega)$, followed by making a subtraction,

$$\nabla' \cdot \boldsymbol{\tau}(\vec{r}',\omega) \cdot \boldsymbol{G}_0(\vec{r}',\vec{r},\omega) - \vec{u}(\vec{r}',\omega) \cdot \nabla' \cdot \boldsymbol{\Sigma}_0(\vec{r}',\vec{r},\omega)\vec{f}(\vec{r}',\omega) \cdot \boldsymbol{G}_0(\vec{r}',\vec{r},\omega) - \vec{u}(\vec{r}',\omega)\delta(\vec{r}' - \vec{r}). \tag{C.9}$$

Using the relationships that

$$\begin{aligned}\nabla' \cdot (\boldsymbol{\tau} \cdot \boldsymbol{G}_0) &= (\nabla' \cdot \boldsymbol{\tau}) \cdot \boldsymbol{G}_0 + \boldsymbol{\tau} \colon \nabla'\boldsymbol{G}_0,\\ \nabla' \cdot (\vec{u} \cdot \boldsymbol{\Sigma}_0) &= \vec{u} \cdot (\nabla' \cdot \boldsymbol{\Sigma}_0) + \nabla'\vec{u} \colon \boldsymbol{\Sigma}_0,\end{aligned} \tag{C.10}$$

and

$$\boldsymbol{\tau} \colon \nabla'\boldsymbol{G}_0 - \nabla'\vec{u} \colon \boldsymbol{\Sigma}_0 = 0, \tag{C.11}$$

$$\nabla' \cdot (\boldsymbol{\tau}(\vec{r}', \omega) \cdot \boldsymbol{G}_0(\vec{r}', \vec{r}, \omega) - \vec{u}(\vec{r}', \omega) \cdot \boldsymbol{\Sigma}_0(\vec{r}', \vec{r}, \omega)) = \vec{f}(\vec{r}', \omega) \cdot \boldsymbol{G}_0(\vec{r}', \vec{r}, \omega) - \vec{u}(\vec{r}', \omega)\delta(\vec{r}' - \vec{r}). \tag{C.12}$$

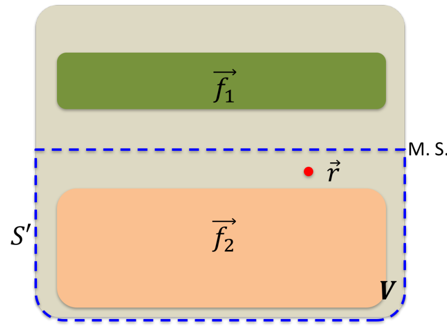

Fig. C.1: A schematic indicating that Green's theorem integral along S' can extract the contribution from $\vec{f}_1$ to the wavefield at $\vec{r}$.

For instance, assuming there are two sources acting on the reference medium, and $\vec{f} = (\vec{f}_1 + \vec{f}_2)$ (as shown in Figure C.1), putting a closed surface S' marked with dashed line, locating $\vec{r}$ inside the volume V, and integrating over V on both sides of Equation C.12, then the application of Green's Second Identity results in

$$\begin{aligned}
&\int_V \nabla' \cdot [\boldsymbol{\tau}(\vec{r}', \omega) \cdot \boldsymbol{G}_0(\vec{r}', \vec{r}, \omega) - \vec{u}(\vec{r}', \omega) \cdot \boldsymbol{\Sigma}_0(\vec{r}', \vec{r}, \omega)] d\vec{r}' \\
&= \oint_{S'} [(\hat{n} \cdot \boldsymbol{\tau}(\vec{r}', \omega)) \cdot \boldsymbol{G}_0(\vec{r}', \vec{r}, \omega) - \vec{u}(\vec{r}', \omega) \cdot (\hat{n} \cdot \boldsymbol{\Sigma}_0(\vec{r}', \vec{r}, \omega))] d\vec{r}' \\
&= \int_V \vec{f}_2(\vec{r}', \omega) \cdot \boldsymbol{G}_0(\vec{r}', \vec{r}, \omega) d\vec{r}' - \vec{u}(\vec{r}, \omega),
\end{aligned} \tag{C.13}$$

where, $\hat{n}$ is the outside normal vector along S' that bounds volume V.

On the other hand, the wavefield at $\vec{r}$ can be expressed by Lippmann–Schwinger equation,

$$\begin{aligned}
\vec{u}(\vec{r}, \omega) &= \int_\infty \vec{f}(\vec{r}', \omega) \cdot \boldsymbol{G}_0(\vec{r}', \vec{r}, \omega) d\vec{r}' \\
&= \int_{\infty - V} \vec{f}_1(\vec{r}', \omega) \cdot \boldsymbol{G}_0(\vec{r}', \vec{r}, \omega) d\vec{r}' + \int_V \vec{f}_2(\vec{r}', \omega) \cdot \boldsymbol{G}_0(\vec{r}', \vec{r}, \omega) d\vec{r}'
\end{aligned}, \tag{C.14}$$

where $\boldsymbol{G}_0$ is causal.

Therefore, choosing a causal $\boldsymbol{G}_0$ in Equation C.13 and comparing Equation C.13 with

Equation C.14, the surface integral corresponds to the contribution from the source $\vec{f}_1$ that is outside the volume; i.e.,

$$-\oint_{S'}[(\hat{n}\cdot\boldsymbol{\tau}(\vec{r}\,',\omega))\cdot\boldsymbol{G}_0(\vec{r}\,',\vec{r},\omega)-\vec{u}(\vec{r}\,',\omega)\cdot(\hat{n}\cdot\boldsymbol{\Sigma}_0(\vec{r}\,',\vec{r},\omega))]d\vec{r}\,'=\int_{\infty-V}\vec{f}_1(\vec{r}\,',\omega)\cdot\boldsymbol{G}_0(\vec{r}\,',\vec{r},\omega)d\vec{r}\,'. \tag{C.15}$$

By using the Sommerfeld radiation condition, the integral along closed surface can be reduced to the top boundary only when S' extends to infinity. The top boundary is actually the measurement surface (m.s.) where data is collected. Equation C.15 provides the basis of wave-separation method for data in the displacement space.

D. THE TRANSFORM OF 2D ELASTIC WAVE EQUATION FROM THE DISPLACEMENT SPACE TO THE PS SPACE

D.1 In the displacement space

In displacement space, the basic wave equations (Matson (1997), Zhang (2006)) are

$$
\begin{aligned}
&\boldsymbol{L}\vec{u} = \vec{f}, \\
&\boldsymbol{L}_0\vec{u}_0 = \vec{f}, \\
&\boldsymbol{L}\boldsymbol{G} = \delta, \\
&\boldsymbol{L}_0\boldsymbol{G}_0 = \delta,
\end{aligned}
\tag{D.1}
$$

where $\boldsymbol{L}$ and $\boldsymbol{L}_0$ are the differential operators that describe the wave propagation in the actual medium and the reference medium, respectively; $\vec{u}$ is the displacement; $\vec{f}$ is the source term; and $\boldsymbol{G}$ and $\boldsymbol{G}_0$ are the corresponding Green's operators for the actual medium and the reference medium, respectively.

In the actual medium, the 2D isotropic elastic wave equation is (Weglein and Stolt (1995))

$$
\boldsymbol{L}\vec{u} = \left(\rho\omega^2 \begin{pmatrix} 1 & 0 \\ 0 & 1 \end{pmatrix} + \begin{pmatrix} \partial_x\gamma\partial_x + \partial_z\mu\partial_z & \partial_x(\gamma-2\mu)\partial_z + \partial_z\mu\partial_x \\ \partial_z(\gamma-2\mu)\partial_x + \partial_x\mu\partial_z & \partial_z\gamma\partial_z + \partial_x\mu\partial_x \end{pmatrix}\right) = \vec{f}, \tag{D.2}
$$

where $\vec{u} = \begin{pmatrix} u_x \\ u_z \end{pmatrix}$; ρ is density; γ is the bulk modulus ($\gamma \equiv \rho\alpha^2$ and α is P-wave velocity);

μ is the shear modulus ($\mu \equiv \rho\beta^2$ and β is S-wave velocity); $\vec{f} = \begin{pmatrix} f_x \\ f_z \end{pmatrix}$.

For an isotropic homogeneous medium, $(\rho, \gamma, \mu) = (\rho_0, \gamma_0, \mu_0)$, $(\alpha, \beta) = (\alpha_0, \beta_0)$.

$$\boldsymbol{L}_0 = \left(\rho_0\omega^2 \begin{pmatrix} 1 & 0 \\ 0 & 1 \end{pmatrix} + \begin{pmatrix} \gamma_0\partial_x^2 + \mu_0\partial_z^2 & (\gamma_0 - \mu_0)\partial_x\partial_z \\ (\gamma_0 - \mu_0)\partial_x\partial_z & \mu_0\partial_x^2 + \gamma_0\partial_z^2 \end{pmatrix} \right). \tag{D.3}$$

D.2 In the PS space

For a homogeneous reference medium, $\boldsymbol{L}_0$ can be diagonalized in the PS basis (Weglein and Stolt (1995))

$$\hat{\boldsymbol{L}}_0 \equiv \boldsymbol{\Pi}\boldsymbol{L}_0\boldsymbol{\Pi}^{-1}\boldsymbol{\Gamma}_0^{-1} = \begin{pmatrix} \nabla^2 + \frac{\omega^2}{\alpha_0^2} & 0 \\ 0 & \nabla^2 + \frac{\omega^2}{\beta_0^2} \end{pmatrix} = \begin{pmatrix} \hat{L}_0^P & 0 \\ 0 & \hat{L}_0^S \end{pmatrix}, \tag{D.4}$$

where $\hat{\boldsymbol{L}}_0$ is the differential operator in the PS space, $\boldsymbol{\Pi} = \begin{pmatrix} \partial_x & \partial_z \\ -\partial_z & \partial_x \end{pmatrix}$, and $\boldsymbol{\Gamma}_0 = \begin{pmatrix} \gamma_0 & 0 \\ 0 & \mu_0 \end{pmatrix}$. The wave equation can then be written in the PS space as

$$\hat{\boldsymbol{L}}_0\boldsymbol{\Phi}_0 = \begin{pmatrix} \hat{L}_0^P & 0 \\ 0 & \hat{L}_0^S \end{pmatrix} \begin{pmatrix} \phi_0^P \\ \phi_0^S \end{pmatrix} = \boldsymbol{F}, \tag{D.5}$$

where

$$\begin{aligned} \boldsymbol{\Phi}_0 &= \begin{pmatrix} \phi_0^P \\ \phi_0^S \end{pmatrix} = \boldsymbol{\Gamma}_0\boldsymbol{\Pi}\vec{u}_0, \\ \boldsymbol{F} &= \begin{pmatrix} F^P \\ F^S \end{pmatrix} = \boldsymbol{\Pi}\vec{f}. \end{aligned} \tag{D.6}$$

The Green's function $\hat{\boldsymbol{G}}_0$ in the PS space can be obtained via

$$\hat{\boldsymbol{G}}_0 \equiv \boldsymbol{\Gamma}_0 \boldsymbol{\Pi} \boldsymbol{G}_0 \boldsymbol{\Pi}^{-1} = \begin{pmatrix} \hat{G}_0^P & 0 \\ 0 & \hat{G}_0^S \end{pmatrix}. \tag{D.7}$$

For the actual medium which is inhomogeneous, on the basis of scattering theory, the Lippmann-Schwinger equation shows

$$\boldsymbol{G} = \boldsymbol{G}_0 + \boldsymbol{G}_0 \boldsymbol{V} \boldsymbol{G}, \tag{D.8}$$

where $\boldsymbol{V}$ is the perturbation satisfying $\boldsymbol{V} = \boldsymbol{L}_0 - \boldsymbol{L}$.

$$\hat{\boldsymbol{G}} = \boldsymbol{\Gamma}_0 \boldsymbol{\Pi} \boldsymbol{G} \boldsymbol{\Pi}^{-1} = \boldsymbol{\Gamma}_0 \boldsymbol{\Pi} (\boldsymbol{G}_0 + \boldsymbol{G}_0 \boldsymbol{V} \boldsymbol{G}) \boldsymbol{\Pi}^{-1} = \hat{\boldsymbol{L}}_0 + \hat{\boldsymbol{G}}_0 \hat{\boldsymbol{V}} \hat{\boldsymbol{G}}. \tag{D.9}$$

In the PS space, $\hat{\boldsymbol{G}} = \begin{pmatrix} \hat{G}^{PP} & \hat{G}^{PS} \\ \hat{G}^{SP} & \hat{G}^{SS} \end{pmatrix}$ and $\hat{\boldsymbol{V}} = \boldsymbol{\Pi} \boldsymbol{V} \boldsymbol{\Gamma}_0^{-1} \boldsymbol{\Pi}^{-1} = \begin{pmatrix} \hat{V}^{PP} & \hat{V}^{PS} \\ \hat{V}^{SP} & \hat{V}^{SS} \end{pmatrix}$.

The elastic wave equations in the PS space for the actual medium are

$$\begin{aligned} \hat{\boldsymbol{L}} \boldsymbol{\Phi} &= \boldsymbol{F}, \\ \hat{\boldsymbol{L}} \hat{\boldsymbol{G}} &= \delta. \end{aligned} \tag{D.10}$$

E. 2D GREEN'S FUNCTION IN THE PS SPACE FOR AN AIR/EARTH MEDIUM

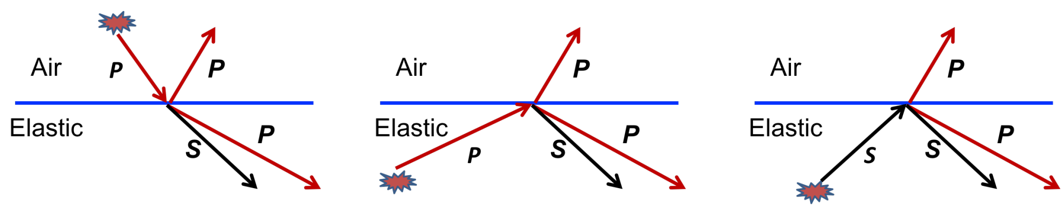

(a) (b) (c)

Fig. E.1: Three diagrams of wavefield for different types of sources in different media. (a) for a P source in the air; (b) for a P source in the earth; (c) for a S source in the earth.

In an air over elastic reference medium ($\hat{\boldsymbol{L}}_0'$), there are three possible experiments, as shown in Figure E.1. For a P source in the air, reflected wave $\grave{P}\acute{P}$ and transmitted waves $\grave{P}\grave{P}$ and $\grave{P}\grave{S}$ will be generated; for a P source in the elastic earth, $\acute{P}\acute{P}$, $\acute{P}\grave{P}$ and $\acute{P}\grave{S}$ will be generated; and for a S source in the elastic earth, $\acute{S}\acute{P}$, $\acute{S}\grave{P}$ and $\acute{S}\grave{S}$ will be generated. The reflection/transmission coefficients will be determined to compute the Green's function. Considering the boundary condition, the normal and shear stresses and vertical displacements are continuous along the air/elastic boundary; i.e., denoting the air is medium (1) and the elastic earth is medium (2),

$$
\begin{aligned}
&\tau_{zz}^{(1)} = \tau_{zz}^{(2)}, \\
&\tau_{zx}^{(1)} = \tau_{zx}^{(2)} = 0, \\
&u_z^{(1)} = u_z^{(2)},
\end{aligned}
\tag{E.1}
$$

where τ_{zz} is the normal stress, τ_{zx} is the shear stress, u_z is the vertical displacement.

With the constitutive relation,

$$\begin{aligned}\tau_{zz} &= \gamma\frac{\partial u_z}{\partial z} + (\gamma - 2\mu)\frac{\partial u_x}{\partial x},\\ \tau_{zx} &= \mu(\frac{\partial u_z}{\partial x} + \frac{\partial u_x}{\partial z}),\end{aligned} \tag{E.2}$$

and $\mathbf{\Phi} = \mathbf{\Gamma\Pi}\vec{u}$, we will have

$$\begin{aligned}\tau_{zz}^{(1)} &= \phi_1^P,\\ \tau_{zz}^{(2)} &= \frac{1}{\rho_2\omega^2}[(\gamma_2 - 2\mu_2)k_{\alpha_2}^2\phi_2^P - 2\mu_2(\frac{\partial^2\phi_2^P}{\partial z^2} + \frac{\partial^2\phi_2^S}{\partial x\partial z})],\\ \tau_{zx}^{(2)} &= -\frac{1}{\rho_2\omega^2}[2\frac{\partial^2\phi_2^P}{\partial x\partial z} + (\frac{\partial^2\phi_2^S}{\partial x^2} - \frac{\partial^2\phi_2^S}{\partial z^2})],\\ u_z^{(1)} &= -\frac{1}{\rho_1\omega^2}\frac{\partial\phi_1^P}{\partial z},\\ u_z^{(2)} &= -\frac{1}{\rho_2\omega^2}(\frac{\partial\phi_2^P}{\partial z} + \frac{\partial\phi_2^S}{\partial x}).\end{aligned} \tag{E.3}$$

Substituting Equation E.3 into E.1, the reflection and transmission coefficients can be confirmed. We assume that the boundary is located at depth 0 m and source and receiver points are at $\vec{r}_s(x_s, z_s)$ and $\vec{r}_(x, z)$, respectively.

For the first situation (Figure E.1(a)), the incident P-wave ($z < 0$) satisfies

$$\begin{aligned}(\nabla^2 + \frac{\omega^2}{\alpha_1^2})\hat{G}_0^P(\vec{r}, \vec{r}_s, \omega) &= \delta(\vec{r} - \vec{r}_s),\\ \hat{G}_0^P(\vec{r}, \vec{r}_s, \omega) &= \frac{1}{2\pi}\int\frac{e^{i\nu_1|z-z_s|}}{2i\nu_1}e^{ik_x(x-x_s)}dk_x,\end{aligned} \tag{E.4}$$

where the vertical wavenumber in the air is $\nu_1 = \begin{cases}\sqrt{k_{\alpha_1}^2 - k_x^2} & \text{if } k_x < k_{\alpha_1}\\ i\sqrt{k_x^2 - k_{\alpha_1}^2} & \text{if } k_x > k_{\alpha_1}\end{cases}$, $k_{\alpha_1} = \frac{\omega}{\alpha_1}$.

The reflected and transmitted waves can be expressed as

$$\begin{aligned}
\hat{G}_0^{PP(1)}(\vec{r},\vec{r}_s,\omega) &= \frac{1}{2\pi}\int \grave{P}\acute{P}\frac{e^{-i\nu_1 z_s}e^{-i\nu_1 z}}{2i\nu_1}e^{ik_x(x-x_s)}dk_x,\\
\hat{G}_0^{PP(2)}(\vec{r},\vec{r}_s,\omega) &= \frac{1}{2\pi}\int \grave{P}\grave{P}\frac{e^{-i\nu_1 z_s}e^{i\nu_2 z}}{2i\nu_1}e^{ik_x(x-x_s)}dk_x,\\
\hat{G}_0^{SP(2)}(\vec{r},\vec{r}_s,\omega) &= \frac{1}{2\pi}\int \grave{P}\grave{S}\frac{e^{-i\nu_1 z_s}e^{i\eta_2 z}}{2i\nu_1}e^{ik_x(x-x_s)}dk_x,
\end{aligned}\tag{E.5}$$

where the vertical wavenumbers in the elastic medium are $\nu_2 = \begin{cases} \sqrt{k_{\alpha_2}^2 - k_x^2} & \text{if } k_x < k_{\alpha_2} \\ i\sqrt{k_x^2 - k_{\alpha_2}^2} & \text{if } k_x > k_{\alpha_2} \end{cases}$,
and $\eta_2 = \begin{cases} \sqrt{k_{\beta_2}^2 - k_x^2} & \text{if } k_x < k_{\beta_2} \\ i\sqrt{k_x^2 - k_{\beta_2}^2} & \text{if } k_x > k_{\beta_2} \end{cases}$, $k_{\alpha_2} = \frac{\omega}{\alpha_2}$, $k_{\beta_2} = \frac{\omega}{\beta_2}$;

$\begin{cases} \grave{P}\acute{P} = \frac{\nu_1 D - \nu_2 n k_{\beta_2}^4}{D_1} \\ \grave{P}\grave{P} = \frac{-2\nu_1 k_{\beta_2}^2(2k_x^2 - k_{\beta_2}^2)}{D_1} \\ \grave{P}\grave{S} = \frac{4k_x\nu_1\nu_2 k_{\beta_2}^2}{D_1} \end{cases}$, where $\begin{cases} n = \rho_1/\rho_2, \\ D = (2k_x^2 - k_{\beta_2}^2)^2 + 4k_x^2\nu_2\eta_2, \\ D_1 = \nu_1 D + \nu_2 n k_{\beta_2}^4. \end{cases}$

For the second situation (Figure E.1(b)), the incident P-wave ($z > 0$) satisfies

$$\begin{aligned}
(\nabla^2 + \frac{\omega^2}{\alpha_2^2})\hat{G}_0^P(\vec{r},\vec{r}_s,\omega) &= \delta(\vec{r}-\vec{r}_s),\\
\hat{G}_0^P(\vec{r},\vec{r}_s,\omega) &= \frac{1}{2\pi}\int \frac{e^{i\nu_2|z-z_s|}}{2i\nu_2}e^{ik_x(x-x_s)}dk_x.
\end{aligned}\tag{E.6}$$

The reflected and transmitted waves can be represented as

$$\begin{aligned}
\hat{G}_0^{PP(1)}(\vec{r},\vec{r}_s,\omega) &= \frac{1}{2\pi}\int \acute{P}\acute{P}\frac{e^{i\nu_2 z_s}e^{-i\nu_1 z}}{2i\nu_2}e^{ik_x(x-x_s)}dk_x,\\
\hat{G}_0^{PP(2)}(\vec{r},\vec{r}_s,\omega) &= \frac{1}{2\pi}\int \acute{P}\grave{P}\frac{e^{i\nu_2 z_s}e^{i\nu_2 z}}{2i\nu_2}e^{ik_x(x-x_s)}dk_x,\\
\hat{G}_0^{SP(2)}(\vec{r},\vec{r}_s,\omega) &= \frac{1}{2\pi}\int \acute{P}\grave{S}\frac{e^{i\nu_2 z_s}e^{i\eta_2 z}}{2i\nu_2}e^{ik_x(x-x_s)}dk_x,
\end{aligned}\tag{E.7}$$

$$\text{where}\begin{cases}\acute{P}\acute{P}=\frac{-2n\nu_2k_{\beta_2}^2(2k_x^2-k_{\beta_2}^2)}{D_1},\\ \acute{P}\grave{P}=\frac{-\nu_1((2k_x^2-k_{\beta_2}^2)^2-4k_x^2\nu_2\eta_2)+\nu_2nk_{\beta_2}^4}{D_1},\\ \acute{P}\grave{S}=\frac{4k_x\nu_1\nu_2(2k_x^2-k_{\beta_2}^2)}{D_1}.\end{cases}$$

For the third situation (Figure E.1(c)), the incident S-wave ($z>0$) satisfies

$$\begin{aligned}&(\nabla^2+\frac{\omega^2}{\beta_2^2})\hat{G}_0^S(\vec{r},\vec{r}_s,\omega)=\delta(\vec{r}-\vec{r}_s),\\&\hat{G}_0^S(\vec{r},\vec{r}_s,\omega)=\frac{1}{2\pi}\int\frac{e^{i\eta_2|z-z_s|}}{2i\eta_2}e^{ik_x(x-x_s)}dk_x.\end{aligned}\tag{E.8}$$

The reflected and transmitted waves can be represented as

$$\begin{aligned}\hat{G}_0^{PS(1)}(\vec{r},\vec{r}_s,\omega)&=\frac{1}{2\pi}\int\acute{S}\acute{P}\frac{e^{i\eta_2z_s}e^{-i\nu_1z}}{2i\eta_2}e^{ik_x(x-x_s)}dk_x,\\\hat{G}_0^{PS(2)}(\vec{r},\vec{r}_s,\omega)&=\frac{1}{2\pi}\int\acute{S}\grave{P}\frac{e^{i\eta_2z_s}e^{i\nu_2z}}{2i\eta_2}e^{ik_x(x-x_s)}dk_x,\\\hat{G}_0^{SS(2)}(\vec{r},\vec{r}_s,\omega)&=\frac{1}{2\pi}\int\acute{S}\grave{S}\frac{e^{i\eta_2z_s}e^{i\eta_2z}}{2i\eta_2}e^{ik_x(x-x_s)}dk_x,\end{aligned}\tag{E.9}$$

$$\text{where}\begin{cases}\acute{S}\acute{P}=\frac{-4nk_{\beta_2}^2k_x\nu_2\eta_2}{D_1},\\ \acute{S}\grave{P}=-\frac{4k_x\nu_1\eta_2(2k_x^2-k_{\beta_2}^2)}{D_1},\\ \acute{S}\grave{S}=\frac{-\nu_1((2k_x^2-k_{\beta_2}^2)^2-4k_x^2\nu_2\eta_2)-\nu_2nk_{\beta_2}^4}{D_1}.\end{cases}$$

Therefore, when both the source and the receiver are in the earth, the Green's function is

$$\begin{aligned}\hat{\boldsymbol{G}}_0(\vec{r},\vec{r}_s,\omega)&=\begin{pmatrix}\hat{G}_0^P&0\\0&\hat{G}_0^S\end{pmatrix}+\begin{pmatrix}\hat{G}_0^{PP}&\hat{G}_0^{PS}\\\hat{G}_0^{SP}&\hat{G}_0^{SS}\end{pmatrix}\\&=\frac{1}{2\pi}\int e^{ik_x(x-x_s)}\left[\begin{pmatrix}\frac{e^{i\nu_2|z-z_s|}}{2i\nu_2}&0\\0&\frac{e^{i\eta_2|z-z_s|}}{2i\eta_2}\end{pmatrix}+\begin{pmatrix}\acute{P}\grave{P}\frac{e^{i\nu_2z_s}e^{i\nu_2z}}{2i\nu_2}&\acute{S}\grave{P}\frac{e^{i\eta_2z_s}e^{i\nu_2z}}{2i\eta_2}\\\acute{P}\grave{S}\frac{e^{i\nu_2z_s}e^{i\eta_2z}}{2i\nu_2}&\acute{S}\grave{S}\frac{e^{i\eta_2z_s}e^{i\eta_2z}}{2i\eta_2}\end{pmatrix}\right]dk_x.\end{aligned}$$

F. DERIVATION OF GREEN'S THEOREM REFERENCE WAVE PREDICTION ALGORITHM IN THE PS SPACE

We here take the reference wave prediction algorithm as an example to explain the derivation of the Green's theorem based wave separation method. The algorithms for the prediction of the scattered wave and the prediction of upgoing reflection data can be achieved in similar strategies.

Let us define $\hat{\boldsymbol{L}}_0, \hat{\boldsymbol{L}}_0^{'}, \hat{\boldsymbol{L}}$ as the differential operators in the PS space, in turn describing the whole-space homogeneous elastic medium, the reference medium composed by a half-space of air over a half-space of elastic earth, and the actual medium; and let $\hat{\boldsymbol{V}}_{air}, \hat{\boldsymbol{V}}_{earth}$ represent the perturbations of air and earth relative to the whole-space homogeneous elastic medium, respectively. Then we have

$$\begin{cases} \hat{\boldsymbol{L}}_0^{'} = \hat{\boldsymbol{L}}_0 - \hat{\boldsymbol{V}}_{air}, \\ \hat{\boldsymbol{L}}\boldsymbol{\Phi} = (\hat{\boldsymbol{L}}_0 - \hat{\boldsymbol{V}}_{air} - \hat{\boldsymbol{V}}_{earth})\boldsymbol{\Phi} = \boldsymbol{F}, \\ \hat{\boldsymbol{L}}_0^{'}\hat{\boldsymbol{G}}_0 = \delta. \end{cases} \tag{F.1}$$

$\hat{\boldsymbol{G}}_0$ represents the Green's function in the reference medium $\hat{\boldsymbol{L}}_0^{'}$.

Written Equation F.1 explicitly,

$$\begin{pmatrix} \nabla'^2 + \frac{\omega^2}{\alpha_2^2} & 0 \\ 0 & \nabla'^2 + \frac{\omega^2}{\beta_2^2} \end{pmatrix} \begin{pmatrix} \phi^P(\vec{r}\,', \vec{r}_s) \\ \phi^S(\vec{r}\,', \vec{r}_s) \end{pmatrix} = \boldsymbol{F}(\vec{r}\,') + (\hat{\boldsymbol{V}}_{air} + \hat{\boldsymbol{V}}_{earth}) \begin{pmatrix} \phi^P(\vec{r}\,', \vec{r}_s) \\ \phi^S(\vec{r}\,', \vec{r}_s) \end{pmatrix}, \tag{F.2}$$

$$
\begin{pmatrix} \nabla'^2 + \frac{\omega^2}{\alpha_2^2} & 0 \\ 0 & \nabla'^2 + \frac{\omega^2}{\beta_2^2} \end{pmatrix} \begin{pmatrix} \hat{G}_0^P(\vec{r}', \vec{r}) + \hat{G}_0^{PP}(\vec{r}', \vec{r}) & \hat{G}_0^{PS}(\vec{r}', \vec{r}) \\ \hat{G}_0^{SP}(\vec{r}', \vec{r}) & \hat{G}_0^S(\vec{r}', \vec{r}) + \hat{G}_0^{SS}(\vec{r}', \vec{r}) \end{pmatrix}
$$
$$
= \begin{pmatrix} \delta(\vec{r}' - \vec{r}) & 0 \\ 0 & \delta(\vec{r}' - \vec{r}) \end{pmatrix} + \hat{\boldsymbol{V}}_{air} \begin{pmatrix} \hat{G}_0^P(\vec{r}', \vec{r}) + \hat{G}_0^{PP}(\vec{r}', \vec{r}) & \hat{G}_0^{PS}(\vec{r}', \vec{r}) \\ \hat{G}_0^{SP}(\vec{r}', \vec{r}) & \hat{G}_0^S(\vec{r}', \vec{r}) + \hat{G}_0^{SS}(\vec{r}', \vec{r}) \end{pmatrix}. \tag{F.3}
$$

We choose a volume as is shown in Figure 4.2, and locate the evaluation point $\vec{r}$ inside the volume, then

$$
\begin{aligned}
&\int_V \Big(\boldsymbol{\Phi}(\vec{r}', \vec{r}_s) \cdot \nabla'^2 \hat{\boldsymbol{G}}_0(\vec{r}', \vec{r}) - \nabla'^2 \boldsymbol{\Phi}(\vec{r}', \vec{r}_s) \cdot \hat{\boldsymbol{G}}_0(\vec{r}', \vec{r}) \Big) d\vec{r}' \\
=& \int_V \left(\begin{array}{l} \boldsymbol{\Phi}(\vec{r}', \vec{r}_s) \cdot \begin{pmatrix} \delta(\vec{r}' - \vec{r}) & 0 \\ 0 & \delta(\vec{r}' - \vec{r}) \end{pmatrix} + \cancel{\boldsymbol{\Phi}(\vec{r}', \vec{r}_s) \cdot \hat{\boldsymbol{V}}_{air}(\vec{r}') \hat{\boldsymbol{G}}_0(\vec{r}', \vec{r})} \\ \cancel{+\boldsymbol{\Phi}(\vec{r}' - \vec{r}_s) \cdot \begin{pmatrix} \frac{\omega^2}{\alpha_2^2} & 0 \\ 0 & \frac{\omega^2}{\beta_2^2} \end{pmatrix}} \hat{\boldsymbol{G}}_0(\vec{r}', \vec{r}) \\ - \left(\begin{array}{l} \cancel{\boldsymbol{F}(\vec{r}') \cdot \hat{\boldsymbol{G}}_0(\vec{r}', \vec{r})} + \hat{\boldsymbol{V}}_{air}\cancel{(\vec{r}') \boldsymbol{\Phi}(\vec{r}', \vec{r}_s) \cdot \hat{\boldsymbol{G}}_0(\vec{r}', \vec{r})} \\ + \hat{\boldsymbol{V}}_{earth}(\vec{r}') \boldsymbol{\Phi}(\vec{r}', \vec{r}_s) \cdot \hat{\boldsymbol{G}}_0(\vec{r}', \vec{r}) + \cancel{\begin{pmatrix} \frac{\omega^2}{\alpha_2^2} & 0 \\ 0 & \frac{\omega^2}{\beta_2^2} \end{pmatrix} \boldsymbol{\Phi}(\vec{r}', \vec{r}_s) \cdot \hat{\boldsymbol{G}}_0(\vec{r}', \vec{r})} \end{array} \right) \end{array} \right) d\vec{r}' \\
=& \boldsymbol{\Phi}(\vec{r}, \vec{r}_s) - \int_V \hat{\boldsymbol{V}}_{earth}(\vec{r}') \boldsymbol{\Phi}(\vec{r}', \vec{r}_s) \cdot \hat{\boldsymbol{G}}_0(\vec{r}', \vec{r}) d\vec{r}' \\
=& \boldsymbol{\Phi}(\vec{r}, \vec{r}_s) - \boldsymbol{\Phi}_s(\vec{r}, \vec{r}_s) \\
=& \boldsymbol{\Phi}_0(\vec{r}, \vec{r}_s)
\end{aligned} \tag{F.4}
$$

where $\boldsymbol{\Phi}_s(\vec{r}, \vec{r}_s)$ represents the scattered wave that is contributed by the earth perturbation (or S_2 in Figure 4.3); and $\boldsymbol{\Phi}_0(\vec{r}, \vec{r}_s)$ is the reference wave, noticing the total wave $\boldsymbol{\Phi}(\vec{r}, \vec{r}_s)$ is the sum of the reference wave and the scattered wave.

Finally we can predict the reference wave by using Green's Second Identity,

$$\begin{aligned}
\boldsymbol{\Phi}_0(\vec{r},\vec{r}_s) &= \int_V \Big(\boldsymbol{\Phi}(\vec{r}\,',\vec{r}_s)\cdot\nabla'^2\hat{\boldsymbol{G}}_0(\vec{r}\,',\vec{r}) - \nabla'^2\boldsymbol{\Phi}(\vec{r}\,',\vec{r}_s)\cdot\hat{\boldsymbol{G}}_0(\vec{r}\,',\vec{r})\Big)\, d\vec{r}\,' \\
&= \oint_{S'} \Big(\boldsymbol{\Phi}(\vec{r}\,',\vec{r}_s)\cdot\nabla'\hat{\boldsymbol{G}}_0(\vec{r}\,',\vec{r}) - \nabla'\boldsymbol{\Phi}(\vec{r}\,',\vec{r}_s)\cdot\hat{\boldsymbol{G}}_0(\vec{r}\,',\vec{r})\Big)\cdot\hat{n}d\vec{r}\,' \\
&\quad \text{(by invoking the Sommerfeld Radiation Condition,)} \\
&= \int_{m.s.} \Big(\boldsymbol{\Phi}(\vec{r}\,',\vec{r}_s)\cdot\nabla'\hat{\boldsymbol{G}}_0(\vec{r}\,',\vec{r}) - \nabla'\boldsymbol{\Phi}(\vec{r}\,',\vec{r}_s)\cdot\hat{\boldsymbol{G}}_0(\vec{r}\,',\vec{r})\Big)\cdot\hat{n}d\vec{r}\,'.
\end{aligned} \tag{F.5}$$

G. DERIVATION OF GREEN'S DISPLACEMENT IN A HOMOGENEOUS ELASTIC MEDIUM

For a whole-space homogeneous elastic medium, the Green's function operators $\boldsymbol{G}_0$ (in the displacement space) and $\hat{\boldsymbol{G}}_0$ (in the PS space) have the relationship of

$$\boldsymbol{G}_0 = \boldsymbol{\Gamma}_0^{-1}\boldsymbol{\Pi}^{-1}\hat{\boldsymbol{G}}_0\boldsymbol{\Pi}, \tag{G.1}$$

$$\hat{\boldsymbol{G}}_0(\vec{r}\,',\vec{r},\omega) = \begin{pmatrix} \hat{G}_0^P(\vec{r}\,',\vec{r},\omega) & 0 \\ 0 & \hat{G}_0^S(\vec{r}\,',\vec{r},\omega) \end{pmatrix} = \frac{1}{2\pi}\int e^{ik_x(x'-x)}dk_x \begin{pmatrix} \frac{e^{i\nu_0|z'-z|}}{2i\nu_0} & 0 \\ 0 & \frac{e^{i\eta_0|z'-z|}}{2i\eta_0} \end{pmatrix}. \tag{G.2}$$

Therefore,

$$\begin{aligned}
&\boldsymbol{G}_0(\vec{r}\,',\vec{r},\omega) = -\frac{1}{\rho_0\omega^2}\boldsymbol{\Pi}^T\hat{\boldsymbol{G}}_0\boldsymbol{\Pi}\delta\boldsymbol{I} \\
&= -\frac{1}{\rho_0\omega^2}\int \begin{pmatrix} \partial_{x'} & -\partial_{z'} \\ \partial_{z'} & \partial_{x'} \end{pmatrix} \begin{pmatrix} \hat{G}_0^P(\vec{r}\,',\vec{r}\,'',\omega) & 0 \\ 0 & \hat{G}_0^S(\vec{r}\,',\vec{r}\,'',\omega) \end{pmatrix} \begin{pmatrix} \partial_{x''} & \partial_{z''} \\ -\partial_{z''} & \partial_{x''} \end{pmatrix} \begin{pmatrix} \delta(\vec{r}\,''-\vec{r}) & 0 \\ 0 & \delta(\vec{r}\,''-\vec{r}) \end{pmatrix} d\vec{r}\,'' \\
&= \frac{1}{\rho_0\omega^2} \begin{pmatrix} \partial_{x'} & -\partial_{z'} \\ \partial_{z'} & \partial_{x'} \end{pmatrix} \begin{pmatrix} \hat{G}_0^P(\vec{r}\,',\vec{r},\omega) & 0 \\ 0 & \hat{G}_0^S(\vec{r}\,',\vec{r},\omega) \end{pmatrix} \begin{pmatrix} \partial_x & \partial_z \\ -\partial_z & \partial_x \end{pmatrix} \\
&= \frac{1}{2\pi}\int \begin{pmatrix} \tilde{G}_{xx}(k_x,z',z,\omega) & \tilde{G}_{xz}(k_x,z',z,\omega) \\ \tilde{G}_{zx}(k_x,z',z,\omega) & \tilde{G}_{zz}(k_x,z',z,\omega) \end{pmatrix} e^{ik_x(x'-x)}dk_x,
\end{aligned} \tag{G.3}$$

where

$$\begin{aligned}
\tilde{G}_{xx}(k_x, z', z, \omega) &= \frac{1}{\rho_0\omega^2}\left(k_x^2\frac{e^{i\nu_0|z'-z|}}{2i\nu_0} + \eta_0^2\frac{e^{i\eta_0|z'-z|}}{2i\eta_0}\right),\\
\tilde{G}_{xz}(k_x, z', z, \omega) &= \frac{1}{\rho_0\omega^2}\left(k_x\nu_0 sgn(z'-z)\frac{e^{i\nu_0|z'-z|}}{2i\nu_0} - k_x\eta_0 sgn(z'-z)\frac{e^{i\eta_0|z'-z|}}{2i\eta_0}\right),\\
\tilde{G}_{zx}(k_x, z', z, \omega) &= \frac{1}{\rho_0\omega^2}\left(k_x\nu_0 sgn(z'-z)\frac{e^{i\nu_0|z'-z|}}{2i\nu_0} - k_x\eta_0 sgn(z'-z)\frac{e^{i\eta_0|z'-z|}}{2i\eta_0}\right),\\
\tilde{G}_{zz}(k_x, z', z, \omega) &= \frac{1}{\rho_0\omega^2}\left(\nu_0^2\frac{e^{i\nu_0|z'-z|}}{2i\nu_0} + k_x^2\frac{e^{i\eta_0|z'-z|}}{2i\eta_0}\right).
\end{aligned} \tag{G.4}$$

H. ANALYTIC EVALUATION OF EQUATION 8.4

Taking a two layered model (Figure 8.1) as an example, and assuming there is no overlap between two primary events in pseudo-depth domain, then the result of Equation 8.4 is

$$\hat{b}_3(k_z) = P^{(2)}(k_z) \cdot \left(P_c^{(1)}(k_z)\right) \cdot P^{(2)}(k_z), \tag{H.1}$$

where $P^{(2)}$ is the second primary of b_1; $P_c^{(1)}$ is the first primary of c_1, with Q/2 amplitude compensation applied; * denotes the conjugate; $k_z = \frac{2\omega}{c_0}$. For this specific model,

$$\begin{aligned} P^{(2)}(k_z) &= T_{01}T_{10}R_2 e^{i(\theta_1+\theta_2)} e^{-(\alpha_1+\alpha_2)}, \\ P_c^{(1)}(k_z) &= R_1 e^{i\theta_1} e^{+\alpha_1}. \end{aligned} \tag{H.2}$$

θ_1 and θ_2 relate to the phase of the events at the first and second layers, and the influence of velocity dispersion due to Q is included; α_1 and α_2 relate to Q amplitude absorption in the first and second layers, respectively; and

$$\begin{aligned} \alpha_1 &= \frac{|\omega|}{c_0 Q_0} z_1 = \frac{|k_z|}{2Q_0} z_1, \\ \alpha_2 &= \frac{|\omega|}{c_1 Q_1}(z_2 - z_1) = \frac{|k_z|}{2Q_1}\frac{c_0}{c_1}(z_2 - z_1). \end{aligned} \tag{H.3}$$

The recorded first-order internal multiple is

$$IM(k_z) = -T_{01}T_{10}R_1R_2^2 e^{i(\theta_1+2\theta_2)} e^{-(\alpha_1+2\alpha_2)}. \tag{H.4}$$

Substituting the expression in Equation H.2 to Equation H.1, and comparing that with Equation H.4,

$$\begin{aligned}\hat{b}_3(k_z) &= (T_{01}T_{10})^2 R_1^* R_2^2 e^{i(\theta_1+2\theta_2)} e^{-(\alpha_1+2\alpha_2)} \\ &- (T_{01}T_{10})\frac{R_1^*}{R_1} IM(k_z).\end{aligned} \tag{H.5}$$

With this specific two-reflector example, we have proven the relationship described in Equation 8.5 and confirmed the ability of this new algorithm to improve the accuracy of the predicted amplitudes of internal multiples.